Study of Neoclassical Internal Transport Barrier with YAG Thomson Scattering Measurement on Compact Helical System

Takashi Minami

DOCTOR OF SCIENCE

Department of Fusion Science

School of Mathematical and Physical Science

The Graduate University for Advanced Studies

2003

Abstract

A physical mechanism of neoclassical internal transport barrier (N-ITB) is studied using 24 spatial channels Nd:YAG Thomson scattering measurement system that has been developed and installed on Compact helical system (CHS).

An important feature of the CHS YAG Thomson Scattering System is to utilize back scattered light in order to resolve the accessibility problem to a diagnostic port due to existence of a helical winding coil that is located on an outside of a vacuum vessel of the CHS device. The scattering light is collected by a large concave mirror ($\phi = 50cm$) in order to increase solid angle for detection, and is introduced to 3 wavelength channels interference polychromators by 33 optical fibers of which core diameter is 2 mm. Avalanche photo diodes that have excellent quantum efficiency at YAG wavelength, 1064 nm, are utilized as detectors. The Thomson scattering system is able to measure a temporal evolution of electron temperature and density profiles simultaneously at 10 ms intervals using the high repetition rate Nd:YAG laser. Data acquisition is carried out using CAMAC modules, and real-time data analysis is performed using an error-weighted multiple lookup table method on VAX computer.

The internal transport barrier in helical plasma is discovered for the first time in CHS and plays an important role on enhanced plasma confinement as well as the ITB that has been observed on Tokamak plasmas. This barrier is formed due to the positive electric field and the electric field shear that is created by bifurcation of radial electric field with the electron cyclotron (EC) heating. The electric field is determined by the ambipolar diffusion of neoclassical particle fluxes, so that this internal transport barrier is named a neoclassical internal transport barrier.

The N-ITB has been formed by the 2nd harmonic EC heating ($P_{inj}^{ECH} \sim 200kW, 53.2GHz$) at the magnetic field strength of B = 0.88T at radial position $\rho = 0.2-0.3$ in low density EC heated plasma ($n_e \sim 4 \times 10^{12} cm^{-3}$). The central electron temperature increases up to $2.2 \pm 0.1keV$.

The steep electron temperature gradient ($dT_e/dr \sim -0.6keV/cm$) is produced at the barrier

location, and the electron temperature increase has been observed only around the plasma center inside the N-ITB. Density fluctuation around the N-ITB measured with HIBP show the clear reduction by ~ 40% at the location of the N-ITB.

The large radial electric field ($E_r \sim 5kV/m$) is observed inside $\rho \sim 0.3$ due to the transition to the electron root from the ion root. The radial electric field shear grows up at $\rho \sim 0.3$,of which value is $\sim -100kV/m^2$ at the barrier location.

The density threshold to form the N-ITB clearly exists at $4-5\times10^{12}cm^{-3}$ on $P_{inj} \sim 120kW$. The electron temperature increases up to $\sim 4keV$ by the density reduction to $2\times10^{12}cm^{-3}$. It is also confirmed that the N-ITB can be formed in the higher density plasma ($\sim 9\times10^{12}cm^{-3}$) at high magnetic field strength $B_T = 1.76T$.

The electron transport analysis is carried out for the ECH plasma. In spite of the high electron temperature, the electron thermal diffusivity of the plasma with N-ITB in the core region is significantly lower than that of the plasma without N-ITB. The reduction of the electron thermal diffusivity at the N-ITB is due to both the reduction of the anomalous transport and the improvement of the neoclassical transport.

The N-ITB also has been observed for EC heated NBI plasma, when 53.2GHz 2nd harmonic EC wave ($P_{inj} \sim 130kW$) was injected into the NBI plasma ($P_{inj} \sim 0.7MW$) with central density $n_e(0)$ of $\sim 3-4\times10^{12}cm^{-3}$. The central electron temperature $T_e(0)$ increases up to $\sim 2keV$ that is about 2 times higher than that of the high density plasma without N-ITB ($n_e(0) \sim 4-5x10^{12}cm^{-3}, T_e(0) \sim 900eV$), while the temperature remains at a few 100 eV in the peripheral region.

The electron N-ITB is formed at the outer location ($\rho \sim 0.4$) compared with the N-ITB in the ECH plasma, so that the improved confinement region is expanded. It is also confirmed with HIBP measurement that this barrier results from the large positive radial electric field ($E_r \sim 15kV/m$) and electric field shear ($dE_r/dr \sim 300kV/m^2$), which are induced by the transition

from the ion to the electron root. The ion temperature is increased ($T_i(0) \sim 400 - 500eV$), and the sharp ion temperature gradient (8-12 keV/m) measured with charge exchange spectroscopy is produced at $rhosim0.6$, of which location is outer than that of the large electron temperature gradient.

The N-ITB formation for the ions in the EC heated N-ITB plasma also depends on the plasma density as well as the electron N-ITB. The central ion temperature rapidly increases up to $\sim 500eV$ from $\sim 200eV$ by the application of ECH when the density is lower than $3 - 4 \times 10^{12}cm^{-3}$. The ion temperature gradient at $\rho \sim 0.6$ increases from 2-3 keV/m up to 8-12 keV/m in the case of N-ITB.

The shearing rate of the $E \times B$ drift velocity for the EC heated NBI plasma increases up to $\omega_{E\times B} \sim 4.0 \times 10^5 s^{-1}, dE_r/dr \sim 300kV/m^2$, of which value is approximately two times as large as that for the ECH plasma ($\omega_{E\times B} \sim 2.5 \times 10^5 s^{-1}$) . The peak of the shearing rate exists around $\rho \sim 0.5$, of which location is outer than that for the ECH plasma with the N-ITB ($\rho \sim 0.25$). The shearing rate value is comparable to that at the internal transport barrier observed in Tokamak experiment.

The transport analysis for the EC heated N-ITB plasma is performed for both electrons and ions. For the electron thermal diffusivity, the N-ITB plasma gives reduced electron thermal diffusivity at $\rho \sim 0.4$ compared to plasma without N-ITB. For the ion thermal diffusivity ,the transport analysis shows the sharp reduction of the ion thermal diffusivity ($\chi_i < 1m^2/s$) at $\rho \sim 0.6$ for N-ITB plasma which is the direct reflection of the steep ion temperature gradient at that position.

The impurity transport is decreased inside the barrier form observation of $TiK\alpha$ line using two-dimensional x-ray CCD camera. The peak energy (4.72-4.73 keV) of the intensity of TiK_α line at $\rho = 0.03$ is shifted to 4.68-4.69kV in the plasma without N-ITB. This results show that the core diffusion coefficient is reduced to $< 0.02m^2/s$ in the plasma with N-ITB, while it is

$0.1 - 0.18 m^2/s$ in the plasma without N-ITB.

It is confirmed that the N-ITB in the helical plasma improves not only the electron thermal transport but also the ion thermal transport and the particle transport improves as well as those have been observed for the ITB in the tokamak plasmas.

Contents

1. Introduction

In a reactor of the controlled thermonuclear fusion as an energy source, it is necessary to confine the energy with a sufficiently dense plasma for a time which allows an adequate fraction of the fuel to react. To achieve this condition in magnetic confinement fusion devices, high ion temperature($T_i \sim 10keV$), high ion density and long confinement time ($n_i T_i \tau \sim 1 \times 10^{21} m^{-3} skeV$) are simultaneously required. The low energy confinement mode (L-mode) is characterized by degradation of confinement time due to the increase in the injected heating power. The L-mode confinement is also observed in the helical plasmas as well as the tokamak plasmas. The typical L-mode scaling law in helical plasma is represented by International Stellarator scaling law (ISS95) as is shown in the following expression [1].

$$\tau_E^{ISS95} = 0.17 P^{-0.58} \bar{n}^{0.69} B^{0.84} a^2 R^{0.75}, \tag{1}$$

where P is absorbed power in MW, $\bar{n}$ plasma density in $10^{19} m^{-3}$, B strength of magnetic field in T, a and R are minor and major radius in m, respectively. The power - exponent of -0.54 dependence on the confinement time in the L-mode scaling is a large obstacle to achievement of break-even in nuclear fusion. Therefore, advanced high energy confinement mode (H-mode) is required.

An internal transport barrier (ITB) is a key issue for enhancement of core plasma confinement and is one of candidates to achieve the advanced H-mode as well as the edge H-mode. First, the internal transport barrier has been observed in tokamak devices. In neutral beam injection experiment, the density and ion temperature peaking with the sharp gradient at the barrier location have been observed. In this situation the reduction of ion thermal and particle diffusivities are also observed to almost same level of the neoclassical transport at the barrier location [2, 3, 4, 5]. In these primary experiments, the reduction of electron thermal transport was not clear. However, in JT-60U experiments [6, 7], simultaneous reduction of the ions and electrons

thermal diffusivities has been observed in the barrier region. The reversed field configuration is created in the current ramp up phase, when the current diffusion time is much longer than the rise time of the plasma current, so that the hollow current profile is formed. The simultaneous temperature increase of the electron ($\sim$ 8keV) and ion ($\sim$15 keV), and $T_i(0)/T_e(0)$ $\sim$1.45 has been realized in spite of dominant ion heating by the neutral beam injection. The n_e and T_e gradients on the ITB are about 20 times as large as those outside the ITB. The electron thermal diffusivity ($\sim 0.1m^2/s$) is sharply dropped by a factor of 20 at the ITB region. The ion thermal diffusivity is simultaneously reduced to the level of the neoclassical transport. The best fusion performance has been obtained in the JT-60U tokamak [8] by forming the ITB. The discovery of the ITB makes the break-through to achieve the Lawson criterion ("break-even" condition: produced thermonuclear power is greater than a sum of heating power and power loss).

In respect of physics, these phenomena are strongly related to the structure of the electric (radial electric field; E_r) and magnetic field of the plasma [9]. In VH mode experiments on DIII-D, a spatial and temporal correlation between the change in the $E \times B$ shear and the reduction in thermal diffusivity are confirmed. The region of the thermal diffusivity reduced has a good agreement with the maximum region of the $E \times B$ sharing rate. This also corresponds to the region where density fluctuation is reduced, which is measured with FIR scattering. Furthermore, the change in the $E \times B$ sharing rate begins prior to the first change in the thermal transport. The anomalous transport suppression is caused by both nonlinear turbulence decorrelation by the $E \times B$ velocity shear [9]. Accordingly, the $E \times B$ shearing stabilization model can explain the formation of transport barriers in magnetic confinement devices.

The helical (including stellarator, heliotron and torsatron) device is characterized by toroidal plasma magnetically confined only by external coils, while the tokamak plasma is confined by both an externally imposed toroidal field and a poloidal field produced by the toroidal current. Helical devices require no current drive, then well suited to steady state operation. The ITB

of helical plasma plays also an important role on plasma confinement enhancement as well as the tokamak plasmas. This ITB was discovered for the first time in Compact Helical System (CHS), then similar improved confinement regimes were found in W7-AS [10] ,TJ-II [12] , and LHD [13].

In CHS, the ITB is created by the EC heating at 53.2GHz and 106GHz for magnetic field strength of 0.88T, where injection power, P_{inj}^{ECH}, is 130-200 kW. The electron ITB was formed at $\rho = 0.2 - 0.3$ in low density EC heated plasma ($n_e \sim 4 \times 10^{12} cm^{-3}$). A significant increase of electron temperature (2-4 keV) and formation of steep electron temperature gradient in barrier region have been also observed. Formation of radial electric field and field shear was found around the barrier. Reduction of fluctuation and electron thermal transport at the barrier location was confirmed.

In W7-AS [10, 11, 12], the ITB was created by the electron cyclotron (EC) heating at 140 GHz ,where $P_{inj}^{ECH}$is 1.2MW. The achieved central electron temperature is $\sim 6keV$ at the electron density, n_e,$\sim 1.5 \times 10^{13} cm^{-3}$ when the magnetic field strength is 2.5 T with the rotational transform, $\iota/2\pi$, is 0.34. The temperature increase and the sharp gradient of the temperature was observed only for electrons.

In TJ-II Heliac [12], the electron ITB is created by the EC heating for the helium plasma. The ITB was observed at $\rho \sim 0.2$ in a low density plasma ($n_e \sim 7 \times 10^{12} cm^{-3}$) ,when injected power is 300 kW. The achieved central electron temperature is 1.5 keV.

In LHD, the electron ITB was created for EC heated counter neutral beam injection (NBI) plasma, where P_{inj}^{ECH} is 280 kW. The central electron temperature increases up to $6keV$ in the low density plasma ($n_e < 1.5 \times 10^{13} cm^{-3}$) , and the steep electron temperature gradient is formed at $\rho = 0.2$. The power threshold ($\sim 150kW$) for the formation of the electron ITB is clearly observed. In these experiments, the similar features as the CHS electron ITB were found, and the universality of the CHS experimental results was confirmed.

After the first observation, the new type of the ITB also has been observed for EC heated NBI plasma on CHS. A significant increase of ion temperature and formation of steep ion temperature gradient have also been observed. The ITB is formed at $\rho = 0.5 - 0.6$ that is outer than the previous ECH experiment, then the improved confinement region is expanded. The improvement of the impurity transport is also confirmed using X-ray CCD camera [14]. Thus, the considerable reduction of diffusivity has been observed not only for the electron thermal transport but also for the ion thermal transport and the impurity transport. The detailed characteristic for the CHS N-ITB that is the main theme of this paper will be discussed later.

The helical plasma has different character for the structure of magnetic and electric fields. The confinement properties of the helical plasma in the low collisional region are determined by the ∇B drift of the trapped particles in the local ripples and by the poloidal $E \times B$ drift. Thus, the neoclassical transport coefficients depend on the radial electric field [11]. The effect of the radial electric field on the neoclassical particle flux is larger for the ion than for the electron. From the ambipolar condition of the particle fluxes that depend on the radial electric field, reversely, the electric field can be derived. The equation has one, two, or three roots of the radial electric field on the same plasma parameters. The positive root is called ”electron root”, while the negative root is called ”ion root”. The existence of the plural roots suggests the capability of the transition phenomenon occurring between two of three states in helical devices. Then, the radial electric field in helical plasma is dynamically changed by neoclassical diffusion in contrast to the tokamak plasma. On the other hand, in these helical devices the magnetic field variation by plasma production is small, which is caused by a finite β effect or a current drive by plasma heating. The sign of the magnetic field shear is normally negative, which coincides with that in the reversed shear region in the tokamak plasmas.

The scenario of the formation of ITB is as following: the E_r transition to the electron from the ion root occurred first in the core region by the electron cyclotron heating (ECH). Con-

sequently, the large radial electric field is created in the core. Simultaneously, the large radial electric field shear is created at the interface between electron and ion roots. Finally, the neoclassical transport is improved by the radial electric field in the core, and the anomalous transport is reduced at the interface. Therefore, the ITB is established. The electric field is determined by the ambipolar diffusion of the neoclassical particle fluxes, so that this internal transport barrier is named neoclassical internal transport barrier (N-ITB).

It is more important to study the correlation between the radial electric field and the transport phenomena caused by N-ITB of the helical plasmas. To investigate detailed transport problem and confinement issues, profile measurement with increased space and time resolution is indispensable. In this respect, the previous Thomson scattering measurement has several problems : high power pulsed laser is limited in repetition rate, while sensitive detector arrays are expensive and difficult to make it spatially dense. Recently, high power Nd:YAG Thomson scattering system and high sensitive avalanche photo diode resolve these problems, so that the simultaneous measurement for the plasma profile at the multipoint and multitime becomes feasible.

In this paper, the investigation of N-ITB plasma on CHS about its dynamic behavior and effect on the transport in helical devices will be reported with the YAG Thomson scattering system.

The contents of this paper are as follows. In section 2, the principle of Thomson scattering measurement and detailed CHS YAG Thomson scattering system will be given. In section 3, the experimental results for EC heated plasma and EC heated NBI plasma will be provided. Finally, section 4 is devoted to discussions. The conclusion is summarized in section 5.

2. Theory of Thomson Scattering Measurement for High Temperature Plasma

2.1 Introduction

The Thomson scattering of a laser light is utilized as a popular method of measuring electron temperature and density of fusion plasma. The traditional Thomson scattering measurement can provide data for only one location at a specified single time during one discharge. In order to investigate plasma physics in fusion research device, it is necessary to determine plasma parameters at many space and time points. For the multipoint Thomson measurement, several kinds of methods have been developed: (1) Ruby Thomson Scattering utilizing an interference filter polychromator, (2) TV Thomson Scattering, (3) LIDAR Thomson Scattering, and (4) YAG Thomson Scattering utilizing an interference filter polychromator. The table 2.1 compares multipoint Thomson scattering systems in major fusion devices.

The ruby system consists of the high power ruby laser and the interference polychromator arrays. This system is a logical extension of a conventional Thomson scattering system to multipoint system. The disadvantage of the system is that only one profile can be measured during a discharge and the system is very complicated [23, 32].

The next TV Thomson system is very sophisticated system for the multipoint diagnostic. The TV Thomson utilizes a single TV camera or a single CCD as a detector. In this system, the collected scattered light is transferred to the spectrometer by fibers [21, 22]. The spectrometer consists of a grating and a relay lens. The image of the beam line along the plasma plane is projected on the CCD or the TV camera in the vertical direction (along the direction of the the spectrometer slit), and the wavelength information is dispersed in the horizontal direction. The advantage of the TV Thomson system is compactness of the system and the good spatial resolution. In RTP or TJ-II case [25, 26], the resolution is approximately 2 mm. On the other hand, the disadvantage of the TV Thomson system is that the high power laser is required because of the low sensitivity of the detector, thus it is very difficult to measure a temporal

evolution of the plasma profile. The TV Thomson system is adopted in major fusion device such as PLT, TFTR, RTP, TJ-II [21, 22, 24, 25, 26].

The LIDAR (light detection and ranging) Thomson scattering system is developed on JET [20]. In this system, the spectrum of the scattered light generated by the short laser pulse ($\sim 300ps$) is recorded as a function of the time. The position of the laser pulse within plasma is derived from the time information. Thus, the electron temperature and density are determined as a function of the spatial location. The advantage of the LIDAR Thomson system is that it is not necessary to calibrate the difference between the spatial positions, because the scattered light is detected by only one detector with specified wavelength for whole positions within plasma. The system can be constructed simple and compact. The disadvantage of the LIDAR system is that the spatial resolution is sparse because the resolution depends on the recording speed of a fast detection system. The typical spatial resolution of the LIDAR system is $\sim 10 - 20cm$.

Almost all these systems above mentioned adopt the ruby laser as the light source. The ruby laser has high power, on the other hand, the repetition rate of the laser fire is low, thus only single profile is measurable during a single discharge. Consequently, it is not suitable for measuring the temporal evolution of the plasma profile.

The purpose of the design of the CHS Thomson scattering system is the measurement of the temporal evolution of the plasma profile, then the ruby laser is not suitable. The high power Q-switched Nd:YAG laser is selected to get high repetition rate. The use of the Nd:YAG laser Thomson scattering diagnostic has been demonstrated on the ASDEX [15, 16], Alcator-C [18, 19] ,DIII-D [28], Tore-supra [31] and JT-60U [27]. The YAG Thomson Scattering System on CHS consists of Nd:YAG lasers, a light collection optics, polychromators, data acquisition systems by CAMAC [33, 34]. The important characteristic of the CHS YAG Thomson Scattering System is to utilize back scattered light. It is difficult to install the collective optics on the normal direction (90 degrees) to the laser beam, because of the existence of the helical wind-

Fusion Device	Thomson System	Spatial Points	Spatial Resolu-tion	Laser	Repiti-tion Rate	Collec-tion Optics	Light Trans-fer Optics	Detector	Spectro-meters
Alcator C Mod	YAG I.F.	11×10 2D	~ 2cm	1J YAG	50 Hz	Lens	Fiber	ICCD	9ch. Grating
JT-60U	YAG I.F.	20	-	2J YAG	10 Hz	Mirror	Fiber	APD	6ch. I.F.
JET	LIDAR	~45	~10-15cm	5J Ruby	1	Mirror, Back Scatter	Mirror	MCP Photo.	6ch. I.F.
PBX-M	TV	55	~1cm,	10J Ruby	1	Lens	FIber	ICCD	Grating
ASDEX upgrade	YAG I.F.	16	2-3cm	1J YAG	20Hz ×6	Lens	Direct	APD	4ch. I.F.
DIII-D	YAG I.F.	40	1.3cm	1J YAG	20Hz ×8	Lens	Fiber	APD	7ch. I.F.
PLT	TV	~80	-	10J Ruby	1	Lens	Fiber	MCP, SIT-vidicon	Grating
TFTR	TV	~80	-	15J Ruby	1	Mirror	Fiber	ICCD	Grating
RTP	TV	118	~2.6mm	25J Ruby	1	Lens	Mirror	ICCD	Grating
Toure Supra	YAG I.F.	12	-	0.7J YAG ×3	27Hz	Lens	Direct	APD	3ch. I.F.
ATF	Ruby I.F.	15x36 2D	-	20J Ruby	1	Lens	Mirror	Photo.	3ch. I.F.
W-VII AS	Ruby I.F.	20	-	10J Ruby	1	Lens	Fiber	Photo.	4ch. I.F.
TJ-II	TV	160	~2.4mm	8J Ruby	1	Lens	Mirror	ICCD	Grating
CHS	YAG I.F.	24	~1-2 cm	0.7J YAG	100(200) Hz	Mirror, Back Scatter	Fiber	APD	3ch. I.F.
LHD	YAG I.F.	120	~1-2 cm	0.6-3J YAG	≥250Hz	Mirror	Fiber	APD	5ch. I.F.

Table 1: Thomson Scattering Systems in major fusion devices. ”1” in repetition rate indicates only one profile can be measured during a discharge. ”photo.” means photomultiplier. ”I.F.” indicates an interference filter polychromator.

ing coil outside the vacuum vessel on the CHS device. The angle between the incident beam and the scattered light is 17 degrees. This backscattered configuration provides the benefit that the integration of the total system to the one port can be arranged in the compact space. The drawback of the back scattered configuration is that the larger stray light comes from a beam dump that is located in the backward of the scattering volume. However this disadvantage is compensated by the larger shift on wavelength of back scattered light compared to that of the normal direction.

The LIDAR system is not appropriate for CHS, because CHS is a medium-sized helical device, and the spatial resolution of the LIDAR system is insufficient. The TV Thomson is more sophisticated system for the profile measurement, however the CCD is not suitable for the YAG wavelength measurement, because the CCD is of low sensitivity at the YAG wavelength. The CHS YAG Thomson system utilizes the interference filter polychromator as the spectrometer. The traditional interference filter polychromator has complicated structure. However, the CHS one is compact and has a simple structure. The scattered light is transferred with the quartz optical fiber that has large core size (2mm). Thus, in spite of making use of many polychromators, the CHS YAG Thomson scattering system is very simple.

Consequently, the CHS YAG Thomson scattering system is superior to the LIDAR or TV system in the capability of the high spatial resolution and the high repetition rate measurement. These performances are indispensable for the study of the local transition phenomena such as the internal transport barrier.

The CHS YAG Thomson scattering system provides a very reliable and useful electron temperature and density information of the high temperature plasma. The system constantly measures inevitable parameters of the CHS plasmas during over 8 years. The design of the LHD Thomson scattering system is based on the CHS system.

2.2 Principle of incoherent Thomson scattering measurement

Thomson scattering measurement is well-known diagnostic for high temperature plasma. In this section, the relativistic thomson scattering cross section is briefly discussed [35].

An incident electric and magnetic wave collide with charged particles, then the particle is accelerated by the electric and magnetic field. The electromagnetic radiation is emitted in all directions. We might have described the process as the photons colliding with the particles, hence bouncing in the different directions. When electron thermal temperature exceeds a 1 keV, the relativistic corrections to the scattering spectrum become significant. The relativistic equation of the motion is

$$\frac{\partial}{\partial t}\left\{\frac{m_0\mathbf{v}}{(1-\beta^2)^{\frac{1}{2}}}\right\} = -e(\mathbf{E}+\mathbf{v}\wedge\mathbf{B}) \tag{2}$$

Here $\mathbf{v} = c\beta$, For the incident transverse wave $\mathbf{E}_i$ propagating in the direction $\hat{\mathbf{i}}$, the electric and magnetic fields are described as

$$\mathbf{B}_i = \frac{1}{c}\hat{\mathbf{i}}\wedge\mathbf{B}_i. \tag{3}$$

The formula for the radiated electric field from an accelerating charge is

$$\mathbf{E}_s = \frac{e}{4\pi\epsilon_0}\left[\frac{1}{\kappa^3 Rc}\{\hat{\mathbf{s}}\wedge(\dot{\beta}\wedge(\hat{\mathbf{s}}-\beta))\}\right] \tag{4}$$

We assume that the field is perpendicular to the scattering plane, such as $\mathbf{e}\cdot\mathbf{s} = 0$ (also $\hat{\mathbf{e}}\cdot\hat{\mathbf{i}} = 0$), where $\hat{\mathbf{e}} = \mathbf{E}_i/E_i$, $\hat{\mathbf{i}}$ and $\hat{\mathbf{s}}$ are incident and scattered directions, respectively. Consequently, the formula for the scattered electric field is

$$\hat{\mathbf{e}}\cdot\mathbf{E}_s = r_e\left[\frac{E_i(1-\beta^2)^{\frac{1}{2}}}{R(1-\beta_s)^3}\{(1-\hat{\mathbf{s}}\cdot\hat{\mathbf{i}})\beta_e^2-(1-\beta_i)(1-\beta_s)\}\right] \tag{5}$$

, where r_e is classical electron radius which is defined as

$$r_e \equiv \frac{e^2}{4\pi\epsilon_0 m_0 c^2}. \tag{6}$$

To obtain the total scattering, is necessary to sum up the electric field contribution from each of the electrons. In this calculation, it is required to take into account the relative phase and amplitude contribution of the each particle. For the Debye shielding of a plasma the charged particle is surrounded by the cloud of the shielding charges, which is characterized by the length λ_D. Because the electron moves much faster than the ion, the electron shield consists of the pure electron (absence of the ion). On the other hand, the ion is slow enough to allow the other ions to participate in the shielding. The ion is surrounded by the cloud that roughly consists of half of the total charge of electrons and ions. If $k\lambda_D << 1$, the scattering from the electron is comparable to the electron shielding cloud, so the scattering is greatly reduced. Thus, the scattering from the plasma mainly comes from the electrons shielding ions. This situation is called the collective scattering or coherent scattering. If $k\lambda_D >> 1$, the phase difference between the scattering from ions and electron is large. In this situation, it is sufficient to suppose that the scattering from electron and shielding cloud is incoherent, and the total scattered power is a sum of the each electron. Now, we consider only the measurement for the electrons with the ND:YAG laser ($\lambda \sim 1064nm, k\lambda_D << 1$), then the scattering is incoherent. First, we consider the Fourier transform of $\mathbf{E}_s(t)$, because we are interested in the frequency spectrum of the scattered field.

$$\mathbf{E}_s(\omega_s) = \frac{1}{2\pi}\int_T \mathbf{E}(t)e^{i\omega_s t}dt = \frac{1}{2\pi}\int_T \left[\frac{r_e}{R}\mathbf{\Pi}\cdot\mathbf{E}_i\right]e^{i\omega_s t}dt. \tag{7}$$

where Π is a tensor polarization that is defined by

$$\mathbf{E}_s(\mathbf{x}, t) = \left[\frac{r_e}{R}\mathbf{\Pi}\cdot\mathbf{E}_i\right] \tag{8}$$

Next, we transform the integral to the retarded quantities. The retarded time defined by the

$$t' = t - \frac{1}{c}(x - \hat{\mathbf{s}} \cdot \mathbf{r}'). \tag{9}$$

where primes denote the retarded quantities. We suppose that the difference between $\mathbf{R}/R$ and $\mathbf{x}/x$ is negligible and the incident wave is monochromatic,

$$\mathbf{E}_i(\mathbf{r}, t) = \mathbf{E}_i \exp i(\mathbf{k}_i \cdot \mathbf{r} - \omega_i t). \tag{10}$$

The transformed formula becomes

$$\mathbf{E}_s(\omega_s) = \frac{r_e \mathrm{e}^{i\mathbf{k}_s \cdot \mathbf{x}}}{2\pi x} \int_{T'} \kappa' \mathbf{\Pi}' \cdot \mathbf{E}_i \mathrm{e}^{i(\omega t' - \mathbf{k} \cdot \mathbf{r}')} dt'. \tag{11}$$

where $\omega = \omega_s - \omega_i$ and $\mathbf{k} = \mathbf{k}_s - \mathbf{k}_i$ which are the scattering frequency and $\mathbf{k}$ vector, and $\mathbf{k}'$ is$1 - \mathbf{s} \cdot \mathbf{i}$. Assuming that the incident wave amplitude $\mathbf{E}_i$ is constant, and also the particle velocity is effectively constant, the time integration in Eq. 11 can be written as

$$\mathbf{E}_s(\omega_s) = \frac{r_e \mathrm{e}^{i\mathbf{k}_s \cdot \mathbf{x}}}{2\pi x} 2\pi\kappa \mathbf{\Pi} \cdot \mathbf{E}_i \delta(\mathbf{k} \cdot \mathbf{v} - \omega) \mathrm{e}^{-i\mathbf{k} \cdot \mathbf{r}}. \tag{12}$$

The scattered power is described as

$$E_s(t) = \int_{-\infty}^{\infty} E_s(\omega_s) \mathrm{e}^{-i\omega t} d\omega_s = \frac{r_e e^{i(\mathbf{k}_s \cdot \mathbf{x} - \omega_d t)}}{x} \mathbf{\Pi} \cdot \mathbf{E}_i. \tag{13}$$

The magnitude of the Pointing vector is

$$\langle S_s \rangle = \langle c\epsilon_0 (\mathcal{R}](E_s(t))^2 \rangle = \frac{1}{2} c\epsilon_0 \left| \frac{r_e}{x} \mathbf{\Pi} \cdot \mathbf{E}_i \right|. \tag{14}$$

thus, the formula for mean power per unit solid angel per unit frequency is

$$\frac{d^2 P}{d\Omega_s d\omega_s} = r_e^2 |\mathbf{\Pi} \cdot \hat{\mathbf{e}}|^2 \langle S_i \rangle \delta(\omega_s - \omega_d). \tag{15}$$

where $\langle S_i \rangle$ is the mean power of the incident wave.

Because this formula gives energy per unit time at observer, when we calculate the total scattered power per unit time at particle, we must multiply κ^2. For the calculation of the total scattering power, it is necessary to multiply the factor $\int d^3\mathbf{v}d^3\mathbf{x}$, then the volume integration is performed. Therefore, the total incoherently scattered power spectrum from the electrons with distribution function f is written by

$$\frac{d^2P}{d\Omega_s d\omega_s} = r_e^2 \int_V \langle S_i \rangle \int |\mathbf{\Pi} \cdot \hat{\mathbf{e}}|^2 \kappa f \kappa \delta(\mathbf{k} \cdot \mathbf{v} - \omega) d^3\mathbf{v} d^3\mathbf{r} \tag{16}$$

The $\mathbf{\Pi} \cdot \hat{\mathbf{e}}$ is written as

$$\mathbf{\Pi} \cdot \hat{\mathbf{e}} = \frac{(1-\beta^2)^{\frac{1}{2}}}{\kappa^3} \times \hat{\mathbf{s}} \wedge \left\{ [\hat{\mathbf{s}} - \beta] \wedge [\hat{\mathbf{e}} - (\beta \cdot \hat{\mathbf{e}})\beta + (\beta \cdot \hat{\mathbf{e}})\hat{\mathbf{i}} - (\beta \cdot \hat{\mathbf{i}})\hat{\mathbf{e}}] \right\}. \tag{17}$$

The relativistic correlation for the Thomson scattering is that we observe the larger intensity from electrons that move to an observer than those that move away. The doppler shift of the scattering from the electron that moves toward the observer is upward in frequency; the blue shift. Thus, the Thomson scattering from the high temperature plasma is enhanced in the blue side of the spectrum.

When $\mathbf{E}_i$ is perpendicular to $\hat{\mathbf{s}}$ and $\hat{\mathbf{i}}$, and the (e.x. $\mathbf{E}_s$) components are selected, the scattered power is written as

$$\begin{aligned} \frac{d^2P}{d\Omega_s d\omega_s} &= r_e^2 \int_V \langle S_i \rangle d^3\mathbf{r} \int |\hat{\mathbf{e}} \cdot \Pi \cdot \hat{\mathbf{e}}|^2 \kappa^2 f \delta(\mathbf{k} \cdot \mathbf{v} - \omega) d^3\mathbf{v} \\ &= r_e^2 \int \langle S_i \rangle d^3\mathbf{r} \int \left| 1 - \frac{(1 - \hat{\mathbf{s}} \cdot \hat{\mathbf{i}})}{(1-\beta_i)(1-\beta_s)} \beta_e^2 \right|^2 \left| \frac{1-\beta_i}{1-\beta_s} \right|^2 \times (1-\beta^2) f \delta(\mathbf{k} \cdot \mathbf{v} - \omega) d^3\mathbf{v} \end{aligned} \tag{18}$$

The $\mathbf{v}$ integral along $\mathbf{k}$ can be performed, then the formula is

$$\frac{d^2P}{d\Omega_s d\omega_s} = r_e^2 \int_V \langle S_i \rangle d^3\mathbf{r} \left| \frac{1-\beta_i}{1-\beta_s} \right|^2 \int \left| 1 - \frac{(1 - \hat{\mathbf{s}} \cdot \hat{\mathbf{i}})}{(1-\beta_i)(1-\beta_s)} \beta_e^2 \right|^2 (1-\beta^2) \frac{1}{k} f(\mathbf{v}_\perp, v_k) d^2\mathbf{v}_\perp. \tag{19}$$

where ($v_k = \omega/k$ and $\beta = (\mathbf{v}_p + \mathbf{v}_k)/c$)

When the β^2 terms can be ignored, the relativistic Thomson scattering power spectrum is

$$\frac{d^2P}{d\Omega_s d\omega_s} = r_e^2 \int_V \langle S_i \rangle d^3\mathbf{r} \frac{1}{k_i[2(1-\hat{\mathbf{i}}\cdot\hat{\mathbf{s}})]^{\frac{1}{2}}} \left(1+\frac{3\omega}{2\omega_i}\right) f_k\left(\frac{\omega}{k}\right) \tag{20}$$

This result shows that in the mildly relativistic formula, the linearly weight factor $(1 - 3\omega/2\omega_i)$ is multiplied to the distribution factor of the non-relativistic formula. This formula provides reasonable accuracy to the electron temperature up to at least 10 keV. For higher temperature, the analytic formula is provided by Zhuravlev and Petrov [36]for an isotropic relativistic Maxwellian distribution . The differential cross section of the Thomson scattering is described as

$$\frac{\omega_s}{r_e^2}\frac{d^2\delta_p}{d\Omega_s d\omega_s} = q(T)\frac{\{2K_2(m_0c^2/T)\}^{-1}\omega_r^2}{\sqrt{\left\{1-2\omega_r\hat{\mathbf{i}}\cdot\hat{\mathbf{s}}+\omega_r^2\right\}}} \times \exp\left[-\frac{m_0c^2}{T}\sqrt{\left\{1+\frac{(\omega_r-1)^2}{2\omega_r(1-\hat{\mathbf{i}}\cdot\hat{\mathbf{s}})}\right\}}\right] \tag{21}$$

where $\omega_r = \omega_s/\omega_i$, $q(T)$ is the appropriate mean value of the depolarization factor $|1-\beta_e^2(1-\hat{\mathbf{i}}\cdot\hat{\mathbf{s}})/(1-\beta_i)(1-\beta_s)|^2$, which is approximated by $q \approx (1 - T/m_0c^2)^2$ .K_2 is the modified Bessel function.

The calculated thomson spectra are illustrated in figure 1 for the YAG laser (wavelength $\lambda = 1064nm$) in which the relativistic effect is taken into account. The angle between the incident laser beam and the scatted light is set to 163 deg. that is actual value of the CHS YAG Thomson scattering system explained later. The vertical axis shows the differential cross section described by Eq. 21 on log scale. The horizontal axis shows the wavelength in an area of blue shift to the YAG wave length because the detector of the CHS YAG Thomson system is sensitive in only blue range. The spectra are plotted for several electron temperatures that are selected for easily understanding variation of the cross section by the temperature in a range of 0.1-64 keV. As the temperature increases, the spectrum doppler broadening is accompanied by the peak position shift of the cross section to blue direction due to the relativistic effect. In the configuration of the CHS YAG Thomson system, the wavelength shift due to the relativistic effect is comparable to the doppler broadening.

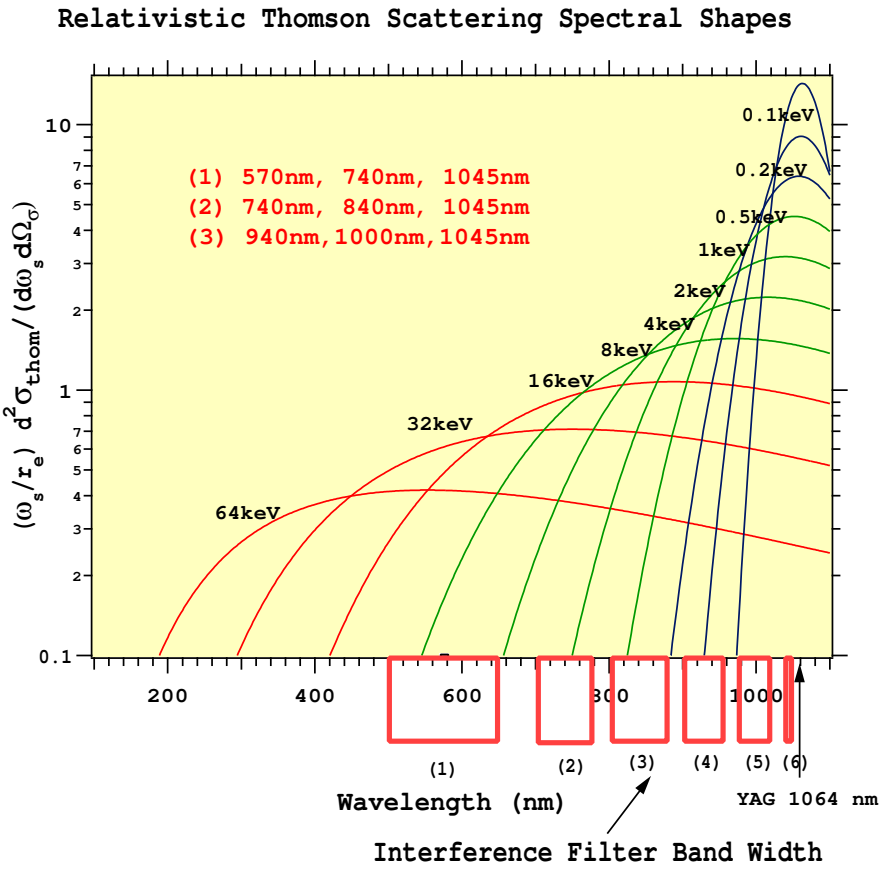

Figure 1: **Relativistic Thomson scattering spectrum shapes for YAG wavelength (1064 nm). The spectra are plotted for several electron temperatures in a range of 0.1-64 keV. Band width of the six polychromator channels are figures under the graph**

2.3 Laser System and Laser Beam Optics

Traditionary, single or double pulse ruby lasers were used for Thomson scattering measurement because that laser has capability of high power and suitable wavelength for usually used detectors such as photo multiplier [33, 34]. For advanced Thomson scattering diagnostic for electron temperature and density, high repetition laser is required to investigate time evolution of plasma discharge. Nd:YAG (yttrium aluminum garnet) laser is selected from many types of laser for the CHS Thomson scattering system because of rapidly pulsing, high power, and affordable cost. Low beam divergence is also required to minimize the beam waist at observation points for efficient collection of the scattering light. The CHS YAG laser can produce bursts of high power Q-switched 0.6J 20 ns pulses at wavelength of 1064 nm with divergence that is below 1.5 mrad. The repetition rate of this laser is 100 Hz, then the profile measurement is able to perform at 10 ms intervals. The laser consists of one oscillator and three optical amplifiers. The oscillator is equipped with a half-wave Pockels cell Q-switch. The output power of the oscillator ,1st,2nd,3rd amplifier are 70 mJ, 430 mJ, 470 mJ, 600 mJ, respectively. A laser beam input optics relay the laser pulse to the vacuum vessel of CHS. The laser system is installed on the floor where the CHS is located, and a distance between CHS and laser is $\sim 5m$ ($\sim 18m$ in Higashiyama site where CHS was formerly placed before movement to Toki site). The laser optics consists of four relay mirrors, one focusing lense, and one beam sampler. The 3 m focal length lens focuses the laser beam to $\sim 2mm$ at the plasma center. The beam sampler is used for introducing the fraction of the laser power to a power monitor. The power monitor consists of an integrating sphere and a silicon photodiode that is used for correcting the beam power fluctuation to the detected scattering light and the trigger of the gate timing to minimize jitter where allowable time lag is below 200 ns. A He-Ne laser is collinear with the YAG laser for beam alignment. The beam dump that is located at the CHS inner port is made with carbon plate that has superior absorption rate for the YAG wavelength (1064 nm) beam.

2.4 Light Collection Optics

The light collection optics is required for providing excellent efficiency of collection rate for the Thomson scattering light [33, 34]. The detailed light collection optics is shown in figure 2. The Thomson scattered light is collected by an f/2 spherical concave mirror coated with Au of which focal length is 100cm,and the diameter is 50cm that has affordable cost. The large solid angle (30 msr-60 msr) and the high reflection rate of the mirror provide the high collection efficiency for the scattering light, then it is possible to measure in lower density plasma ($< 5 \times 10^{12} cm^{-3}$) at only single shot. A collective window of 20 cm in diameter is installed to the same port as the laser injection to arrange all components compactly. The laser injection port is kept as far from the collective window ($\sim 1.5m$) as possible to avoid the reflection by the laser injection window to the optical fibers. The collected scattered light is focused on 33 optical fibers that are arranged in line to transfer the scattered light to the polychromators. The optical fiber is a single fiber to avoid a finite packing loss (> 70%). The core diameter is 2 mm that is less than the maximum spherical aberration < 2 mm. To get the enough coupling efficiency, the polymer clad (2.1mm) silica fiber that has the larger numerical aperture (=0.33) is selected. The nylon jacket diameter (3mm) determines the spatial resolution. The configuration of the components of the collection optics is determined to minimize the aberrations of the concave mirror. Because most of the collected light pass through near the center of the window, all the aberrations except the spherical one are kept at a minimum level.

2.5 Polychromators

The polychromators utilize an interference filter and an avalanche photo diode (APD) [33, 34]. The number of polychromators that correspond to the observation points in the plasma is 24. Each polychromator has three wavelength channels and is designed to maximize transmission. The schematic drawing of the polychromators is shown in figure 3. The scattering light is cas-

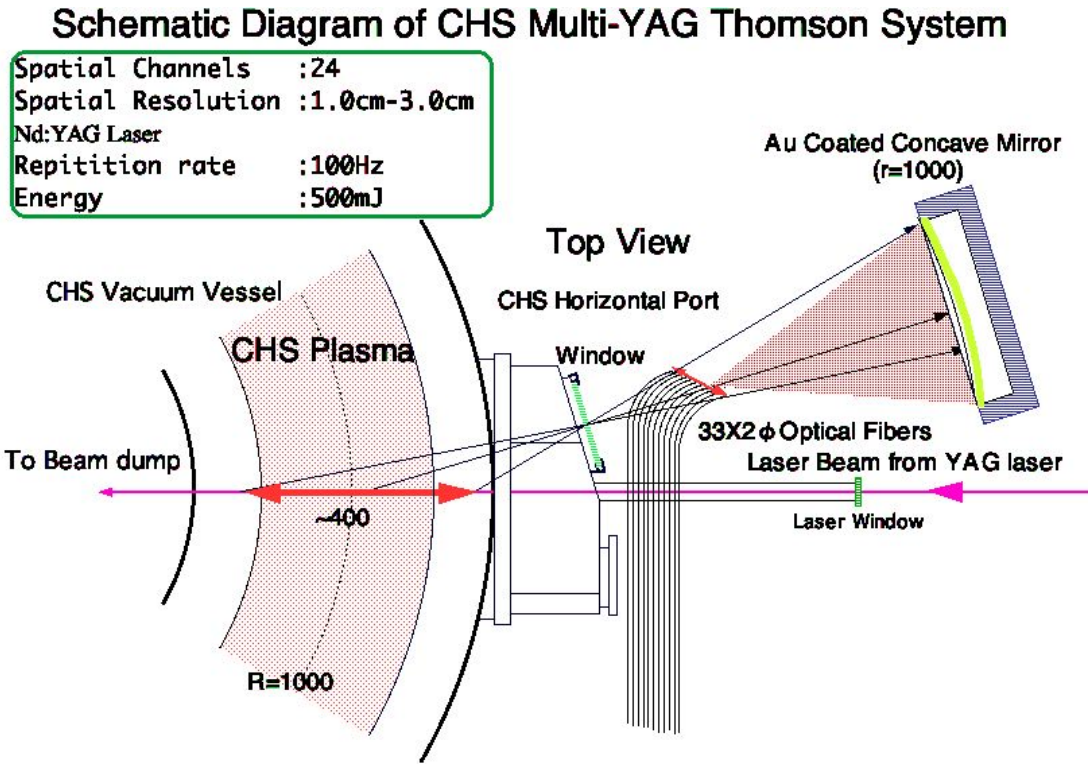

Figure 2: **Schematic diagram of CHS Multi-YAG Thomson Scattering system.**

caded between the interference filters using relay lens, and is introduced to the three detectors.

The transmission and reflection rates of the interference filters are > 70%, > 95%, respectively. The reflectance losses on other optical components are < 4%, thus the total throughput is larger than 60%. The rejection rate of the interference filters for the wavelength out of transmission range is $> 1 \times 10^{-5}$, which is enough to eliminate an intense stray light (wavelength is 1064 nm).

The output image of the filter polychromator is directly coupled to large photo sensitive surface (3mm diameter), silicon APDs (EG & G C30956E) whose quantum efficiency is above 80% at 900 nm, 40% even at 1060 nm. This large quantum efficiency is required to detect the subtle Thomson scattering light. Each channel has a pre-amplifier that utilizes commercial video amp. The output of the amplifier is coupled with a high-path filter whose cut off frequency is $\sim 3MHz$ that is enough to reduce the signal from the back scattered light.

For the selection of the filter sets, we take into account the range of the electron temperature

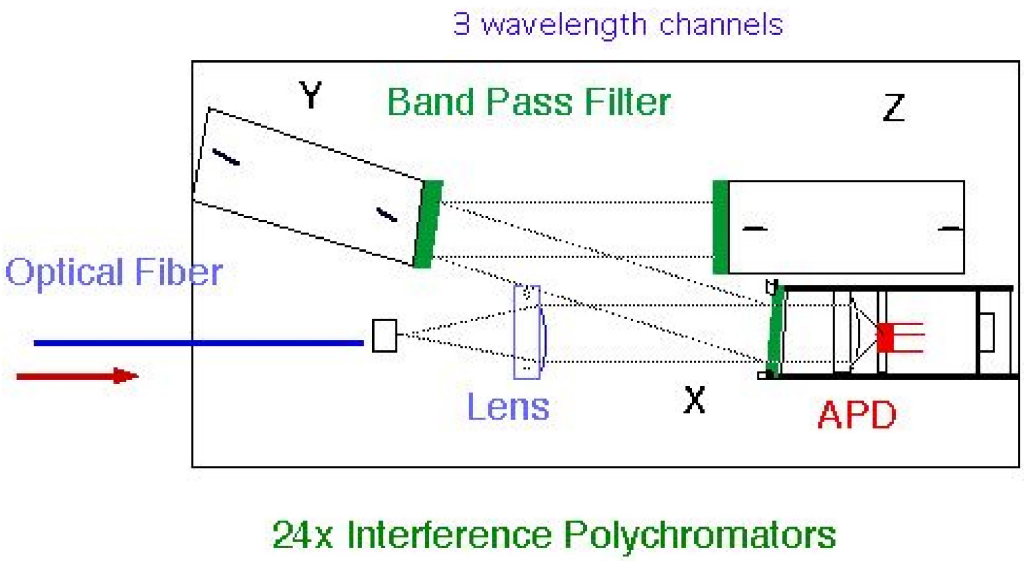

Figure 3: **Schematic drawing of three wavelength polychromator.**

that is realized on CHS, however it is not easy to measure wide range of temperature using only one filter set that consists of three filters. The high electron temperature measurement up to $\sim 10keV$ that is prospected as maximum temperature on the CHS in the core region requires the set of the wider band width filters. On the other hand, the precise low temperature measurement such as edge temperature that is expected as low as $\sim 50eV$ to understand the edge transport physics of several processes as well as L-H transitions requires the narrow band filter as close to the laser wavelength.

To solve this problem, we choose four kind of filter sets that correspond to following four temperature ranges:

1. for high temperature range (6 keV-0.1 keV), 9 polychromators, (a, b, d)
2. for middle high temperature range (2 keV-0.02 keV), 7 polychromators, (b, c, d)
3. for middle low temperature range (1 keV-0.01 keV), 5 polychromators, (c, d, e)
4. for low temperature range (0.5 keV-0.005 keV), 3 polychromators, (d, e, f)

Symbols a,b,c,.....denote following filters.

a CW:940 nm,BW:70

b CW:1000 nm,BW:45

c CW:1030 nm,BW:20

d CW:1045 nm,BW:12

e CW:1050 nm,BW:5

f CW:1055 nm,BW:4

CW:center wavelength,BW:band width

To optimize the performance of the polychromators, the filter sets selection is performed using a simulation code that modeled the polychromator behavior: 1). The statistical fluctuation of the photons is a main noise source. We calculated this level of the scattered photons plus the bremsstrahlung photons. In this code the filter transmission, the detector quantum efficiency is considered. The Seldem model 2) is used to calculate the Thomson scattering spectrum, which takes into account the relativistic blue shift. I developed this code using Mathematica [37]. The typical results of this code are as follows. Figure 4 (a) shows the estimated relative error of the electron temperature for the polychromator of the high temperature range (6 keV-0.1 keV). The calculation is carried out using the following parameters: the laser energy is 500mJ, $n_e = 1 \times 10^{19} m^{-3}$,the solid angle is 30 mstr, the scattering length is 1 cm, and the scattering angle is 17 deg. . The relative error increases with decrease in the electron temperature because of the bremsstrahlung light that mainly affects the range of the low temperature. The estimated error remains less than 5 % in the whole range of the prospective electron temperature value (6 keV-0.1 keV). Figure 4 shows the relative error of the electron density. The estimated error is, especially, lower than that of the electron temperature in the high electron temperature range.

All filter combinations are selected and optimized using this simulation code to lower the relative error to below 5%. Consequently, the prospected performance of the polychromator using the four types of filter sets is able to cover the whole required range of the electron temperature and density that is prospected on CHS.

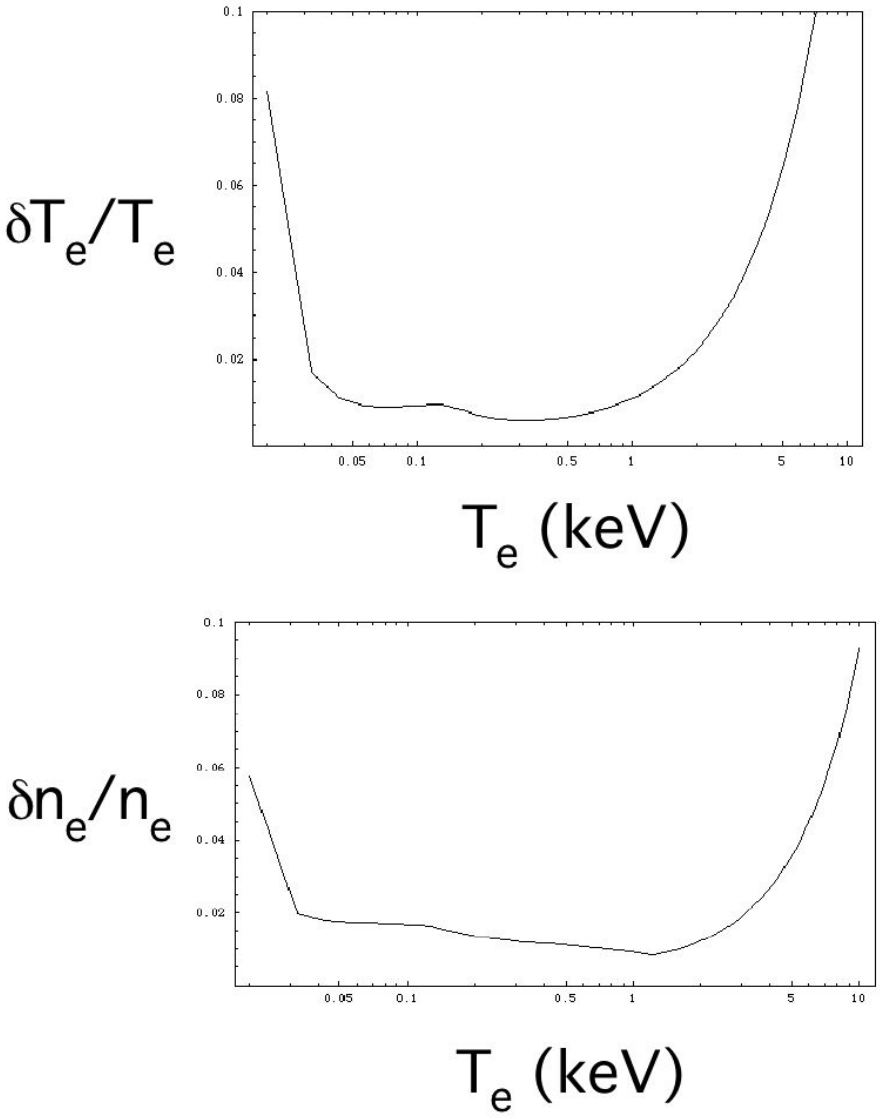

Figure 4: **Estimated relative error of electron temperature and density for an optimized filter set**

2.6 Calibration

In order to derive electron temperature, it is necessary to calibrate relative sensitivity of polychromators to the wavelength between channels. In the calibration, a reference monochromator

(CVI Degikrom 240) with a halogen lamp as a light source is utilized. The relative transmission rate of the monochromator is calibrated by the absolute calibrated commercial power meter (Yokogawa 3292). Figure 5 shows the typical example of the relative sensitivity spectrum of the polychromator in the filter combination for the high electron temperature that is described in the above section. It is noted that the transmitted wavelength is shifted due to the tilt of the interference filter on the incident light. The angle of incident light to the filter affects the transmitted wavelength. The frequency shift is expressed by

$$\lambda = \lambda_0(1 - sin^2\theta/N^2)^{1/2}, \tag{22}$$

where λ is the transmitted wavelength at incident angle θ, $\lambda_0 = \lambda$ at $\theta = 0degee$, N is the effective index of refraction that is equal to 1.9. The transmitted wavelength in figure 5 has good agreement with specifications of the filters by taking into account this shift, however, subtle disagreement remains because the actual incident angle is different from the designed one.

To calibrate total sensitivities in the polychromators and the optical systems for an absolute density measurement, Raman scattering light from nitrogen molecules is utilizedciteraman,ramanRohr,ramanPenney. The Rayleigh scattering method has been most frequently used for the absolute calibration of the Thomson measurement system on fusion devices. However, the stray light level is too high to separate the Rayleigh signal on the system in the configuration using the backward light, and another dedicated detector is required for the calibration of the interference polychromator because the Rayleigh wavelength is rejected by the filter. Accordingly, the Raman scattering method is suitable for the interference polychromator.

The hydrogen gas is most appropriate for the Raman scattering calibration, because of a large frequency shift of the rotational Raman lines and a large cross section that can be easily detected without the reduction of the S/N ration by the stray light. However, the hydrogen de-

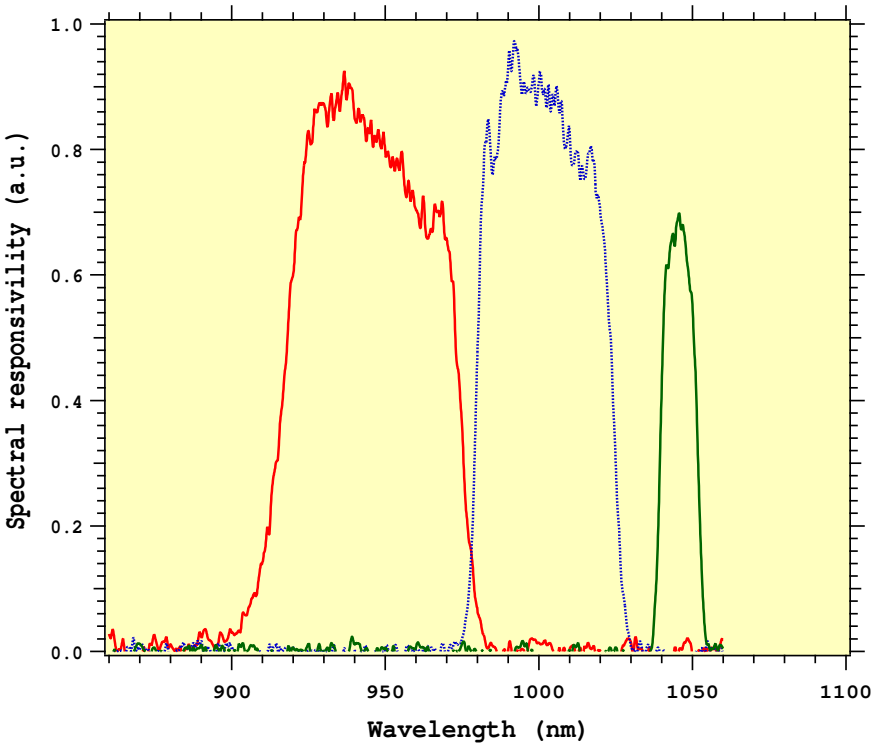

Figure 5: **The typical spectral responsivity of three wave length channels for a polychromator.**

grades the wall recycling and is hard to deal with the hydrogen gas because of explosive nature. Therefore, the nitrogen Raman scattering is utilized as the second candidate. The Raman signal of the nitrogen gas has a small shift of the scattered lines and small cross section. However, because of the wide band width of the interference filters that can include many Raman lines, we can detect enough signal to noise ratio for the accurate calibration.

The rotational N_2 Raman scattering differential cross section spectrum normalized by the Thomson scattering cross section for the YAG wavelength (=1064 nm) [40] is shown in figure 6 with the transmittance of the interference filter(CW=1045 nm,BW=12 nm). The intensity of the Raman scattering light is reduced by the transmittance of the filter. The cross section is exponentially decreased as the wavelength is shifted from 1064 nm, so that the accurate measurement of the transmittance was carried out, because the edge of the transmitted wavelength of the filter is steeply dropped.

The typical result of the N_2 Raman scattering calibration is sown in figure 7, where the

detected signal that includes the stray light as offset is plotted at four pressures 0, 200, 400, 600 torr at room temperature. In the experiment, about 1000 shots are accumulated for achieving good S/N ratio.The scattering light is proportional to the gas pressure. The figure shows the good linearity between the signal and the pressure for all the polychromators. That proves the N_2 Raman scattering calibration to be effective for the absolute density calibration.

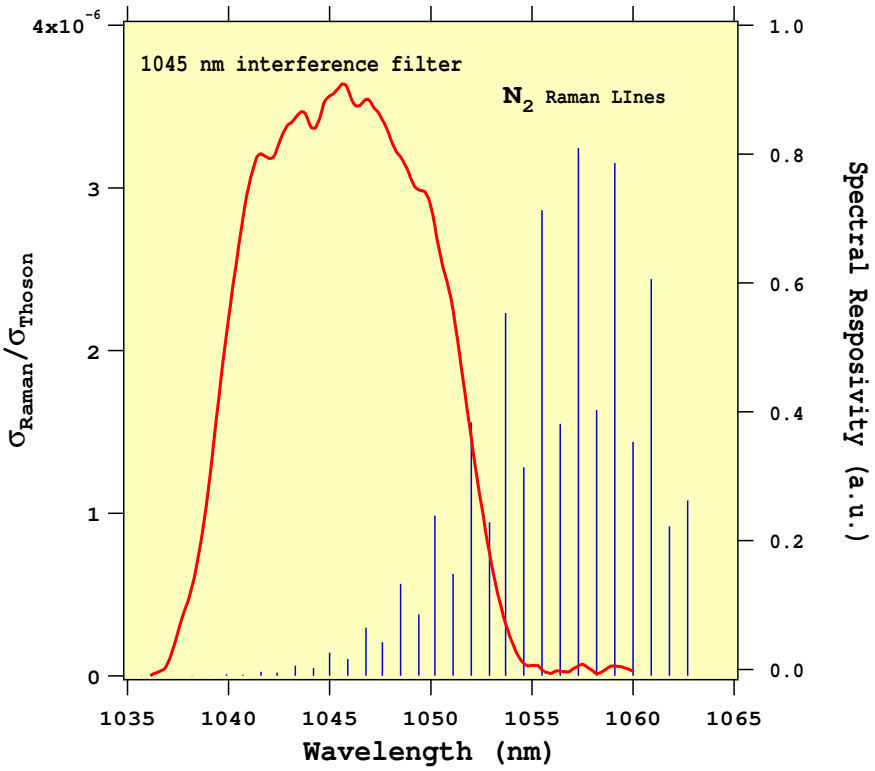

Figure 6: **Rotational N_2 Raman scattering differential cross section spectrum normalized by the Thomson scattering cross section for the YAG wavelength (=1064 nm). Spectral responsivity of 1045 nm interference filter is over plotted.**

2.7 Data Acquisition System and Analysis Method

Data acquisition is carried out using the standard CAMAC crate that is located near the polychromators. The signals from polychromators are digitized with LeCroy 4300B; fast charge integrated A/D converter. The gate timing is triggered by the sampled signal of the YAG laser to which several timings are added to acquire back ground signals. The timing is adjusted to the arrival time of the scattering signal by adjusting length of the coaxial cables between the poly-

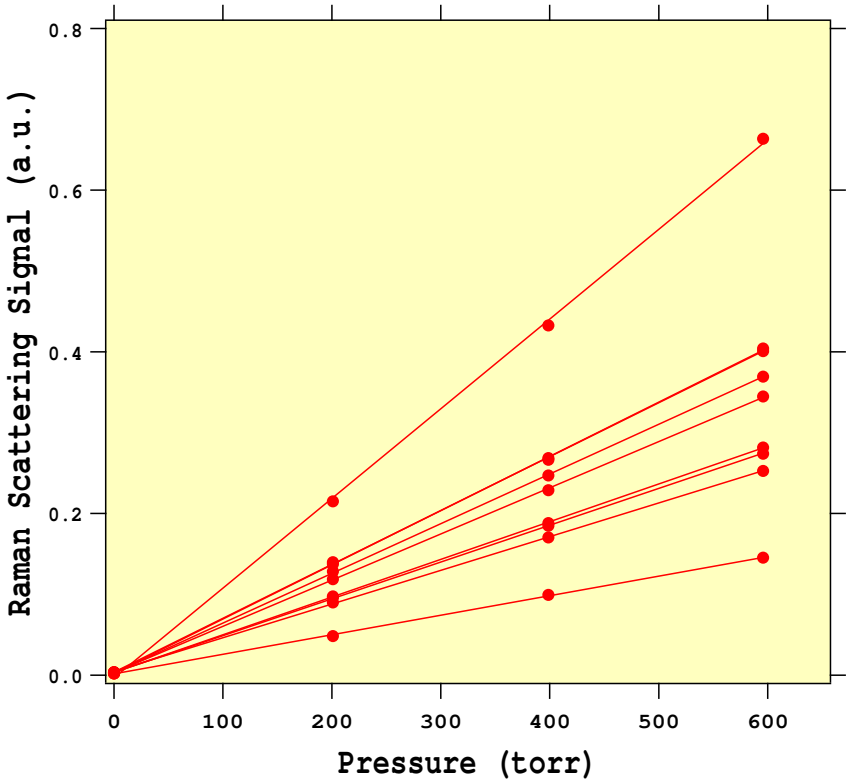

Figure 7: **The result of the N_2 Raman scattering calibration. The typical 9 polychromators are selected and plotted as a function of N_2 pressure on room temperature.**

chromator and the digitizer. The converted data are transfered to the memory module by the FERA (fast encoding and readout ADC) controller through high speed ECL data bus. The VAX directly reads the memory using standard CAMAC calls. In calibration, the data are acquired by PC with simple operation. The FERA data transfer speed is 10 MWords/Sec, which is fast enough for all data form polychromators to be transfered in less than 10μsec..

Real-time data analysis is performed using following procedure. The data are preprocessed before the analysis: the level of the stray light that is sampled after the plasma discharge and the level of the back ground light that is sampled after laser firing during 100μsec. are subtracted from the raw data of the scattering light. To calculate electron temperature and density from the scattering signal, we performed an error-weighted multiple lookup table method [30] used by DIII-D [28]. The set of signals ratios between polychromator channels are calculated

$$R^{ij} = \frac{S_i}{S_j} \tag{23}$$

where S_i is the signal from the i th wavelength channel of the polychromator.

The ratio is calculated as the function of the electron temperature using the above relativistic Thomson scattering cross section formula from the calibration factor. We can derive the electron temperature and its error $(T_e^{ij}, (\sigma_T^2)^{ij})$ as a function of the ratios and its errors of signals.

$$T_e^{ij} \equiv T_e(R^{ij}) \tag{24}$$

$$(\sigma_T^2)^{ij} = \left(\frac{dT_e^{ij}}{dR^{ij}}\right)^2 (\sigma_R^2)^{ij} \tag{25}$$

The correspondence between R^{ij} and T_e^{ij} is calculated by the spline interpolation from calibration factors. We can define the functions C_1^{ij}, C_2^{ij} and build tables.

$$C_1^{ij} \equiv \frac{T_e^{ij}}{\left(\frac{dT_e^{ij}}{dR_{ij}}\right)^2} \tag{26}$$

$$C_2^{ij} \equiv \frac{1}{\left(\frac{dT_e^{ij}}{dR^{ij}}\right)^2} \tag{27}$$

The averaged electron temperature is calculated using the next equation.

$$T_e = \sum_{i,j} \frac{C_1^{ij}}{(\sigma_R^2)^{ij}} \Big/ \sum_{i,j} \frac{C_2^{ij}}{(\sigma_R^2)^{ij}} \tag{28}$$

In this equation, the contribution from the electron temperature which has a large error becomes minimum. The error of the electron temperature is also calculated as follows

$$\sigma_T^2 = \frac{1}{\sum_{i,j} \frac{C_2^{ij}}{(\sigma_R^2)^{ij}}}. \tag{29}$$

The electron density is derived from the total number of the scattered photon that is integrated over the entire spectrum. We can build a set of tables of C_3^i for the electron density

calculation. The factor is calculated using the N_2 Raman scattering calibration, where the difference in the angular dependence between the Raman and Thomson scattering cross sections is corrected.

$$n_e^i = C_3^i(T_e)N_i \tag{30}$$

,where N_i is the signal which corresponds to the i th wavelength channel of the interference polychromator normalized by the laser energy. N_i is proportional to the number of the photons.

The averaged n_e is also calculated from the following equation.

$$n_e = \sum_i \frac{N_i}{(\sigma_N^2)^i} \Big/ \sum_i \frac{1}{(\sigma_N^2)^i} \tag{31}$$

The error of the electron density is calculated from the following equation.

$$\sigma_{n_e} = 1 \Big/ \sum_i \frac{1}{(\sigma_N^2)^i}. \tag{32}$$

Using this table reference method, it is possible to perform a full analysis very quickly ,and provide results of the electron temperature and the density as soon as the data are acquired. All the calculated results are displayed in real-time on the monitor in the operation room. The delay between the acquisition and the display is no more than 2-3 sec., and this method can be as accurate as the least squares fit.

3. Experimental Results

3.1 Introduction

In this section, the experimental results of N-ITB experiments are described. The content consists of the N-ITB for the plasma heated with electron cyclotron only (ECH plasma) and the plasma heated simultaneously with ECH and neutral beam injection (NBI). In the ECH plasma, the formation of the N-ITB for the electrons was clearly observed for the first time. The clear reduction of the density fluctuation and the electron thermal transport were discovered. After obtaining these results, the N-ITB for ions was discovered for the EC heated NBI plasma.

3.2 N-ITB Experiments for ECH plasma

3.2.1 Compact Helical System

Compact Helical System (CHS) belongs to Heliotron/Torsatron type devices, whose magnetic field structure has a polarity of l=2 and the period number m=8 respectively, and the major and averaged minor radii of 1.0 and 0.2m respectively. The schematic drawing of the CHS is shown in figure 8. The machine is designed to investigate the energy and particle transports, MHD characteristic, and plasma wall interaction with the aspect ratio as low as 5 [41]. The magnetic field configurations can be modified by independently controlled three PF coils, so it is possible to investigate the MHD characteristic and the transport problem under a variety of magnetic configuration on well and shear, rotational transform profile, magnetic axis location relative to the equi-B surface. The CHS is equipped with two NBI systems (maximum power of each NBI is $\sim 1MW$) and two gyrotrons (53GHz, 106GHz).

It is possible to investigate a wide variety of plasmas that has a wide range of plasma parameters by combining ECH and NBI for plasma heating.

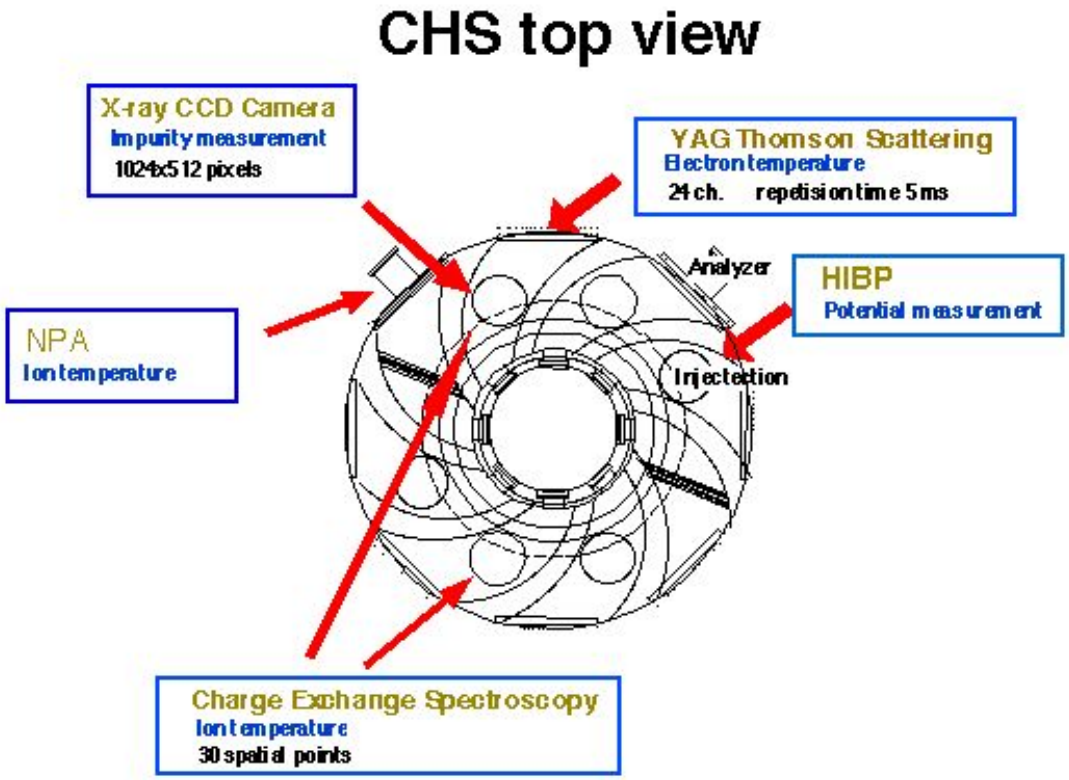

Figure 8: **Schematic drawing of Compact Helical System**

3.2.2 N-ITB Experiment for ECH Plasma

The N-ITB experiment presented here was performed for the plasma that was produced by a gyrotron with the frequency of 53.2 GHz for the 2nd harmonic resonance at the magnetic field strength of 0.88T, In this experiment, the resonance zone is precisely located at the plasma center. The experiment is performed for the low density plasma. The electron temperature profiles measured with the multipoint YAG Thomson scattering system along the horizontal plane are shown in figure 9 resulting from 10-20 accumulated shots to get enough S/N ratio. There is a clear difference between the profiles of electron temperature for the plasma with and without the N-ITB. The data are plotted as a function of the flux coordinate denoted by ρ. This expression is convenient for comparison to the results of the other profile measurement such as a charge exchange spectroscopy.

The electron temperature is 1.3 keV for the low density plasma ($n_e(0) = 6 \times 10^{12} cm^{-3}$) in

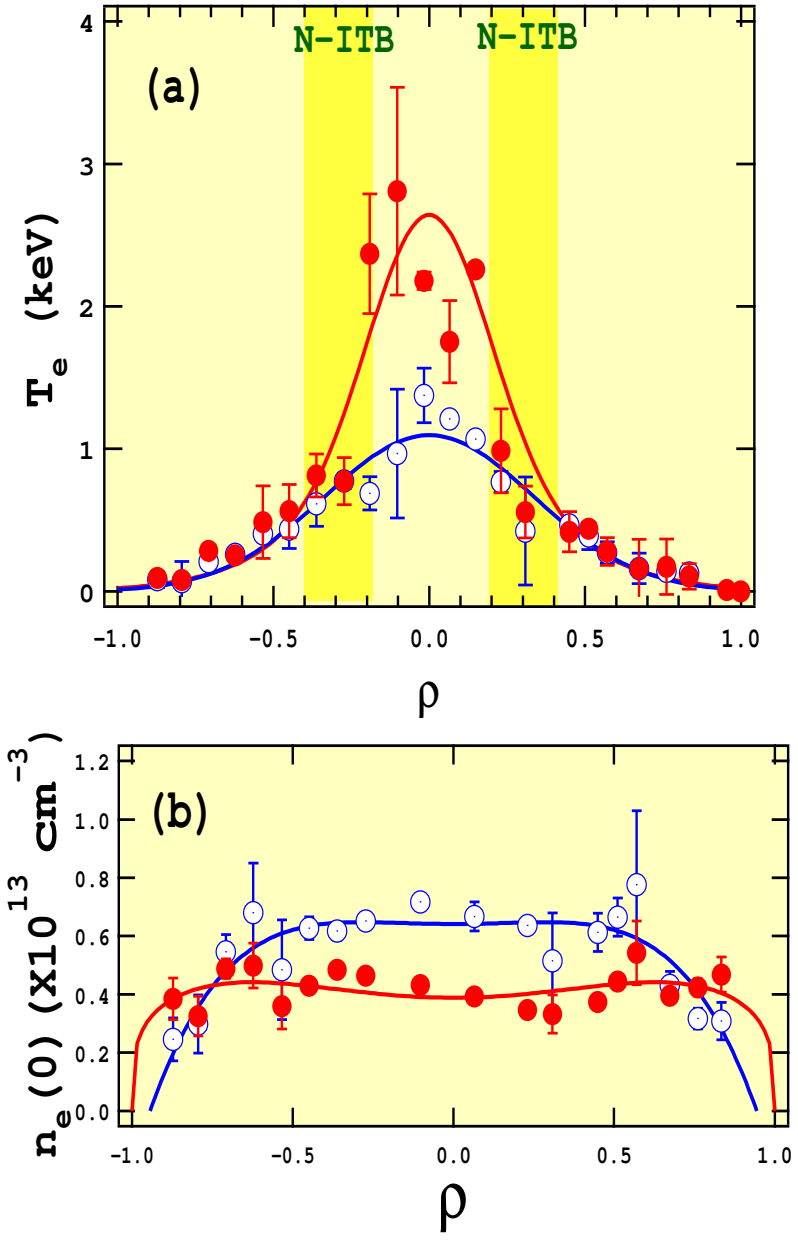

Figure 9: **Electron temperature (a) and density (b) profile. The close (red) circles show the ECH plasma with N-ITB ($P_{inj} \sim 200kW$). The open (blue) circles show the ECH plasma without N-ITB ($P_{inj} \sim 150kW$).**

the case of the injected ECH power of 150kW. The plasma profile is parabolic that is typical in usual CHS experiment. When the ECH power increases up to 200 kW and the density slightly decreases to $n_e(0) = 4 \times 10^{12} cm^{-3}$, the temperature profile shows a prominent change: dome structure in the core region appears as is shown in figure 9(a). The central electron temperature derived from 15 accumulated shots increases up to $2.2 \pm 0.1 keV$, while the electron temperature outside the dome remains $\sim 0.8 keV$, which is almost same as the temperature outside for the plasma without N-ITB. The increase of the electron temperature occurs in the plasma core region. The steep electron temperature gradient ($dT_e/dr \sim -0.6 keV/m$) is produced at the bending location of the electron temperature profile ($\rho \sim 0.3$), while that is $dT_e/dr \sim -0.1 keV/m$ for the plasma without N-ITB.

In contrast, the electron density profile is slightly hollow or almost flat (figure 9 (b)), which is the typical shape of the ECH plasma on CHS that is caused by the pump out of the particle due to the ECH. There is no prominent difference for the density gradient at the location of the N-ITB, as shown in figure 9 (b). The plasma pressure is a production of the temperature and the density, then the pressure profile shape is almost determined by the electron temperature due to the flat density profile. Accordingly, the steep pressure gradient exists at $\rho(r/a) \sim 0.3$ that corresponds to the location where the steep gradient of the electron temperature exists.

The injected ECH power of more than 90% is absorbed at the resonance zone that is located inside of $\rho = 0.1$, and the power is not absorbed in the outer area outside of $\rho = 0.1$. Consequently, the steep pressure gradient suggests the improvement of the electron transport: an energy transport barrier for electrons is formed at the point with the large gradient. The occurrence of these phenomena depends on the plasma density, which is discussed later.

We succeeded in achieving the maximum electron temperature in CHS discharges was achieved using the N-ITB formation. Figure 10 shows the electron temperature and density profiles of this shot. The electron temperature profile reveals the clear characteristic of

the N-ITB plasma: the existence of the large temperature gradient, hence, the steep pressure gradient at the barrier location and the clear dome shape structure formed in the plasma core. The electron temperature increases up to $\sim 4keV$ by the density reduction to $2 \times 10^{12} cm^{-3}$ in $P_{inj} \sim 200kW$. The electron temperature of the outside of the improved region remains low temperature ($T_e \sim 0.5keV$), then the difference between the inside and outside is outstanding.

3.2.3 Thomson Spectrum Shape for N-ITB Plasma

There is a problem whether the high value of the electron temperature ($T_e \sim 2 - 4keV$) reflects a bulk component or a tail component (high energy super thermal electron) that is a minority of the electrons. If the measured temperature is affected by the high energy electron, the real temperature of the bulk electron is lower than the measured electron temperature with YAG Thomson scattering. A few additional channels are required to separate more precisely the bulk temperature from the effect of superthermal electron, because the Thomson scattering system has normally three wave length channels. However, it is not easy to modify the optical configuration of the polychromator that has no room in the polychromator to install the other components. To solve this problem, three sets of interference filter polychromators that have following combinations of center wavelength are used. (1) 570 nm, 740 nm, 1045 nm, (2) 740 nm, 840 nm, 1045 nm, (3) 940 nm, 1000 nm, 1045 nm. These wavelength ranges are denoted by the red squares below the graph of figure 1. The 1045 nm filters are used for the relative calibration of sensitivity among the three polychromators. Using all wavelength channels of the three polychromators, it is possible to measure the Thomson scattering light at six types of wavelength. For six-channel measurement, the measurable range of temperature expands from $50eV - 3keV$ to $50eV - 20keV$, while spatial resolution is reduced to $\sim 5cm$ from $\sim 1.5cm$, which is about half radius of the inside N-ITB region.

Figure 11 shows Thomson scattering spectrum shape measured with the virtual six-channel polychromator [44]. The horizontal axes indicate a square of wavelength shift normalized by

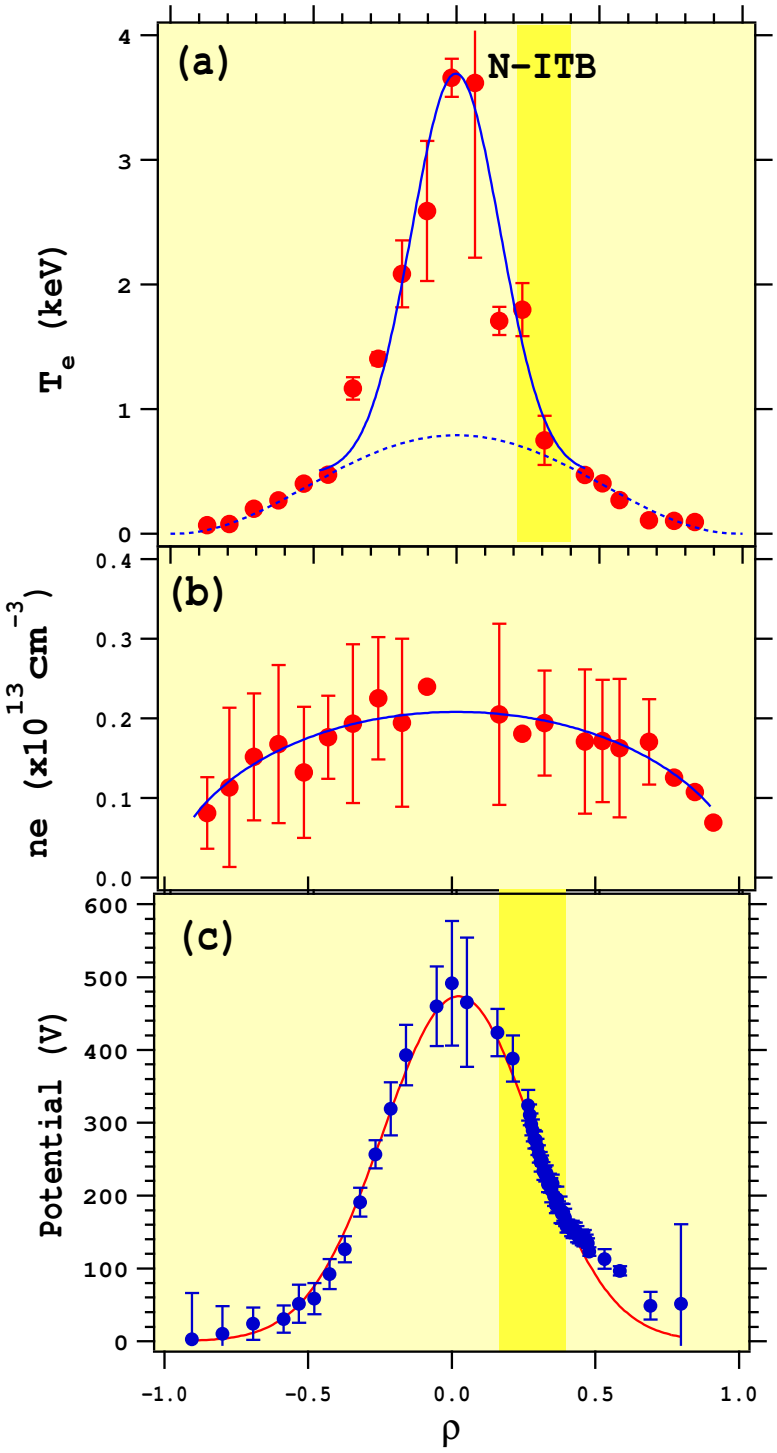

Figure 10: **Electron temperature (a) ,density (b) and potential (c) profile for the plasma with maximum electron temperature in CHS discharges.**

the YAG wavelength, and the vertical axis indicates a logarithm for the intensity of the scattering light. The axes are selected so that a gaussian profile is expressed by a linear function. If the measurement is affected by the high energy electrons, then the plot should show a nonlinear relation, and the Thomson scattering spectrum is not gaussian.

However, the Thomson spectrums for the ECH plasma with N-ITB show linear dependence. For the plasma without N-ITB, the spectrum, of course, shows the linear relation. Consequently, from the six-channel measurement, it is confirmed that the effect of tail electron on the derived temperature from three channels of the polychromators is negligible, and the high electron temperature of the Thomson scattering measurement is the temperature of the bulk electrons.

The gradient of the spectrum measured with the six-channel measurement also shows that there is an obvious difference of the electron temperatures between inside and outside N-ITB as shown in figure 11 (a), while the difference is slight in the plasma without N-ITB, as shown in figure 11 (b). The derived temperature ($2.16 \pm 0.14 keV$) within the N-IITB is three times as large as that of the outside region ($0.77 \pm 0.09 keV$) near the N-ITB, and is almost two times as large as that at the plasma center ($1.31 \pm 0.07 keV$) in the plasma without N-ITB . Therefore, these results clearly show the high electron temperature region exists in the plasma core.

3.2.4 Potential Measurement for N-ITB

The radial potential is measured with Heavy Ion Beam Probe (HIBP). The principle of potential measurements with the HIBP is as follows. Singly charged ions are injected into the plasma, then doubly charged ions emerge from the plasma with the energy change which corresponds to the space potential at the birth point. The required capability of the HIBP analyzer is to distinguish an energy change due to the potential ($\sim 10V$) form the kinetic energy of beam ($\sim 100kV$). A secondary beam sweeper is introduced in addition to the primary sweeper in the CHS HIBP. The purpose of the second sweeper installed is (1) the reduction of the error caused by the uncertainly of the beam injection angle; (2) the expansion of the observable area;

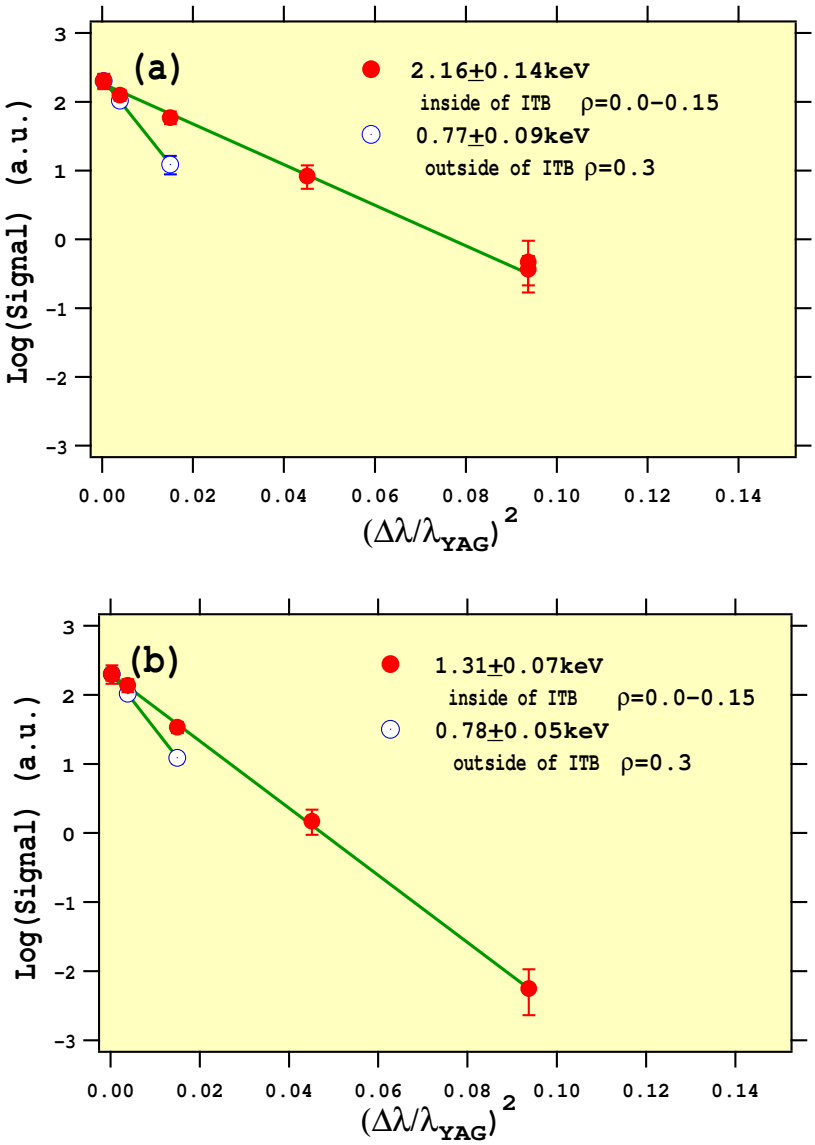

Figure 11: **The Thomson scattering spectrum shape. (a) the injected power is** $\sim 200kW$**. Profile has ITB. (b) the injected power is** $\sim 150kW$**. Profile has no ITB. The horizontal axis indicates a square of wave length shift normalized by the YAG wave length, and the vertical axis indicates logarithm of the intensity of the scattering light.**

(3) keeping away the analyzer from the magnetic field fluctuation which disturbs the beam energy. Under the operational condition of N-ITB experiments the cesium beam is used. The beam energy is 72 keV. The radial length of the sample volume is a few cm according to the calculated trajectory. The detected beam current is $\sim 100nA$ at maximum, while the amplifier noise level is approximately $\sim \pm 0.2nA$. The time resolution is up to 250 kHz.

The potential profiles for the plasma with and without N-ITB obtained with the HIBP measurement are shown in figure 12. The measurement is carried out for the above mentioned ECH plasma with N-ITB. The profile for the EC heated plasma with N-ITB has the prominent dome structure in the core region as well as the electron temperature profile with the YAG Thomson scattering measurement. The central plasma potential with N-ITB increases up to $\sim 400V$ from $\sim 200V$ that is for no N-ITB case. There is no change in the potential outside the improved region, of which characteristic is similar to that in the electron temperature above mentioned. Accordingly, the large radial electric field and the large radial electric field shear are created. The plasma rotation due to the $E \times B$ velocity is different between inside and outside N-ITB ($v_{EXB}^{out} \sim 9km/s$,and $v_{EXB}^{in} \sim 2km/s$). This result suggests the difference of the confinement character, and it is discussed below in detail.

The structure of the radial electric field is investigated around the location of N-ITB. Figure 13 (a) shows the radial electric field that is derived from the derivative of the potential for the plasmas with and without the N-ITB. The plasma with the large radial electric field ($E_r \sim 5kV/m$) is observed inside $\rho = 0.3$ where the E_r shows the transition to the electron root from the ion root; the electron thermal transport is reduced inside $\rho = 0.3$ due to the suppression of fluctuations by the radial electric field shear, which is discussed in the next section. On the other hand, the plasma without the N-ITB has smaller E_r ($E_r < 2kV/m$).

The radial electric field shear that is derived form the derivative of the radial electric field is plotted in figure 13(b). The shear grows up at $\rho = 0.3$, and the value reaches $\sim -100kV/m^2$

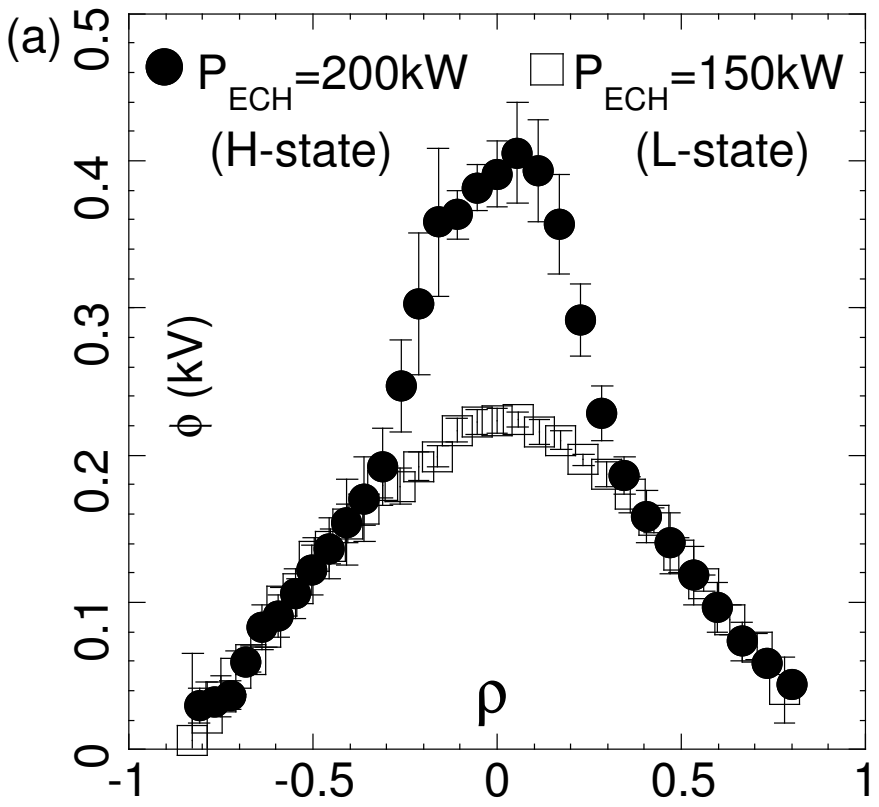

Figure 12: **Potential profile measured with HIBP for with and without N-ITB. The potential increases in the core region due to transition to electron root from ion root.**

for the plasma with the N-ITB where the steep electron temperature gradient is located . In contrast, the shear for the plasma without the N-ITB is almost constant in the whole plasma region. The observation that the radial electric field and shear outside the N-ITB are at almost same level shows the transition occurs on only in the plasma core and there is no change in the peripheral region of the plasma.

It is noted that the larger radial electric field is created, the more electron temperature increases. In accordance with this, when the maximum electron temperature , mentioned above, is achieved the plasma potential has the prominent steepest potential gradient at the location of the large electron temperature gradient is formed, as is shown in figure 10(c). The bifurcation of the plasma potential is controlled by the ECH injection power. The power threshold of the transition that is observed in the plasma potential was found to be in the range of $\sim 150 - 170kW$ at the density regime of $\bar{n_e} \simeq (4-6) \times 10^{12} cm^{-3}$. The N-ITB is formed by raising the ECH power. It is noted that two bifurcated states also depend on the plasma density, which is discussed later.

3.2.5 Reduction of Density Fluctuation on N-ITB

Density fluctuations around the location N-ITB are measured with HIBP shot by shot in sequential discharges under the same condition. The results are shown in figure 14. The fluctuation spectra are detected from the beam current at the several spatial points: $\triangle r$=-3,-1,0,1, and 3 cm, where $\triangle r$ represents the distance from the location of the N-ITB and the location $\triangle r = 0$ corresponds to $r_0 = 4.3 \pm 0.9$ cm ($\rho_0 = 0.23 \pm 0.05$). The spectrum at $\triangle r = 0$ indicates a reduction in power whose frequency ranges from 5 to 70 kHz, while the spectra apart from $\triangle r = 0$ have a large power.

Figure 15(b) shows the integral of power spectrum from 5 to 70kHz as a function of the observation position:

$$Q(\triangle r) = \int P df \tag{33}$$

. The figure clearly shows power reduction on the N-ITB by 39%, which is estimated from

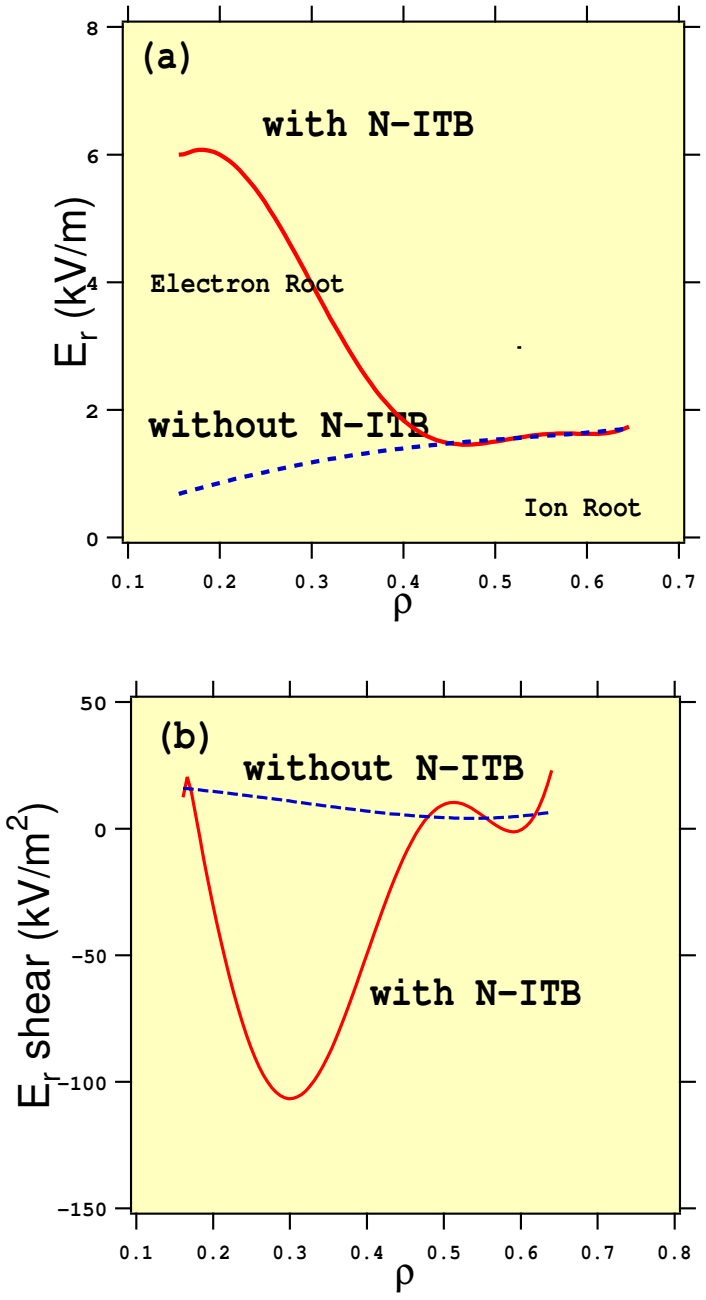

Figure 13: **Profiles of (a) the radial electric field and (b) the radial electric field shear. The solid (red) line indicates ECH plasma with N-ITB, and dotted (blue) line indicates without N-ITB. The large radial electric field is formed inside N-ITB for the transition from ion to electron root.**

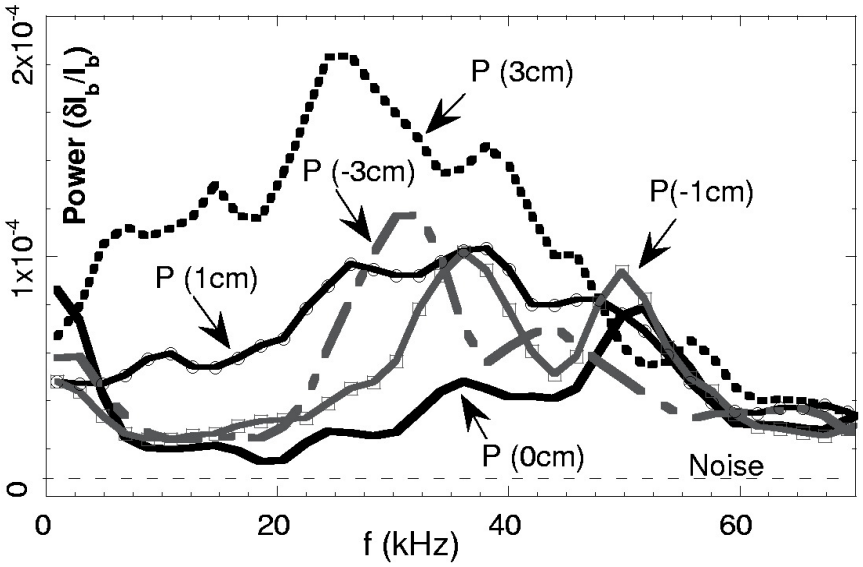

Figure 14: **Power spectra of density fluctuation at several points around the shear-maximum point for N-ITB plasma.**

$[\bar{Q}(1cm) - Q(0)/\bar{Q}(1cm)$ with $\bar{Q}(1cm) = 0.5[Q(1cm) + Q(-1cm)]$. Figure 16 exhibits a peak frequency and width of spectrum normalized by the peak frequency. Those values are obtained by fitting the following function

$$P(f) = P_0 exp[\frac{-(f - f_0)^2}{\triangle f^2}] + P_{base}. \tag{34}$$

The peak frequency becomes maximum, and the normalized band width is narrower at the barrier location.

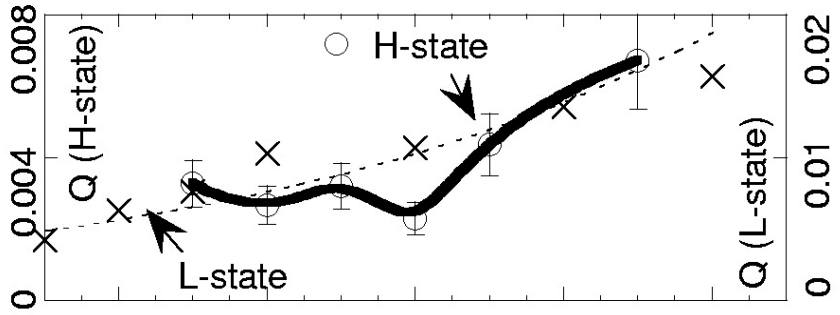

Figure 15: **Integrated powers of density fluctuations.**

The reason why the integral is performed from 5 to 70kHz is because the low frequency should contain other effects such as plasma movements, and the power spectrum above 70kHz

just shows a nature of white noise that corresponds to the parameter $P_{base} \sim 1 \times 10^{-5}$. This fluctuation level could be attributed to the path integral effects [42]. The noise level of an integrated fluctuation is estimated as $Q_{noise} \sim 10^{-5}$. Consequently, the reduction of the fluctuation power at the N-ITB is 48% when the noise is subtracted form the fluctuation integral. The integral of power spectrum for the plasma without N-ITB is also shown in figure 15, and the integral shows the fluctuation increases toward the outside of the N-ITB. The power level is almost two times as large as that for the plasma with the N-ITB, which shows that the fluctuation is $\sim \sqrt{2}$ times larger.

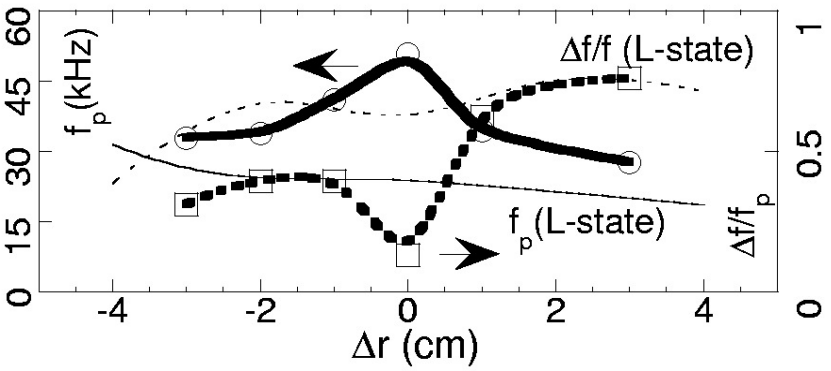

Figure 16: **Peak f_p and width Δf of frequency spectrum.**

The peak frequency and the normalized band width by the peak frequency for the plasma without N-ITB are also shown in figure 16. The peak frequency has maximum and the band width is narrower at the barrier location.

3.2.6 Dependence of N-ITB Formation on Density

Operation condition for N-ITB formation depends on the plasma density. Figure 17 shows electron temperature at the plasma center and at the outer location ($\rho = 0.5$) as a function of central electron density. In this experiment, the injected power is $\sim 120kW$, the frequency is 53.2GHz, and B_T is 0.88 T, which are almost same as the above described ECH experiment described above [44].

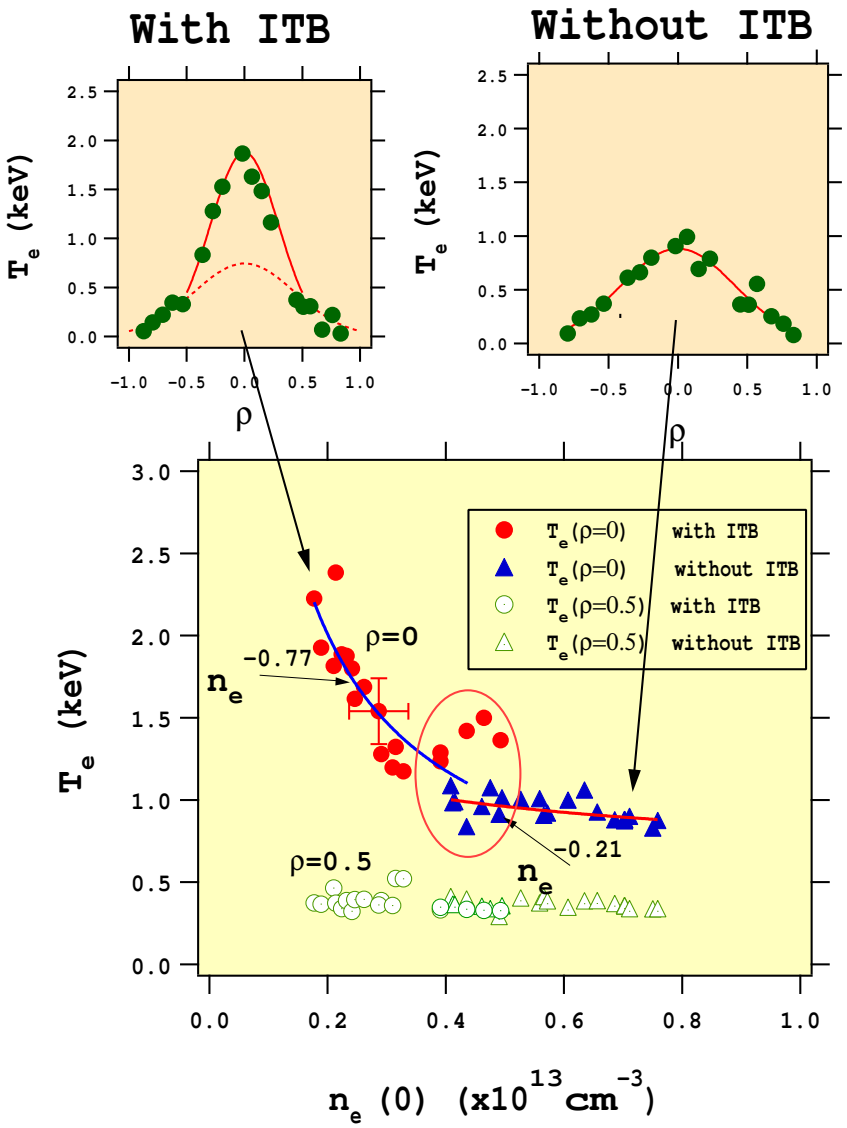

Figure 17: **Electron temperature of 53.2 GHz ECH plasma as a function of central electron density.** $P_{inj} =\sim 120kW$**,** $B_T = 0.88T$**.**

As the density decreases below the specific value ($4-5\times10^{12}cm^{-3}$), the central electron temperature increases significantly, and the electron temperature shape is transformed to the dome shape (denoted by closed red circles) that indicates N-ITB formation. The electron temperature goes up to $2.5keV$ at the low electron density ($2\times10^{12}cm^{-3}$). On the other hand, when the density increases above the threshold value (denoted by the blue triangles), the electron temperature monotonically decreases with the gradual gradient (1.0-0.8 keV), and the temperature shape has no dome structure and no specific point of the steep electron temperature is created that indicates the N-ITB. Then, the electron temperature dependence on the density is changed from $T_e \propto n_e^{-0.77}$ to $T_e \propto n_e^{-0.21}$ at the threshold density. This remarkable change of the density dependence indicates the improvement of the electron energy transport caused by the N-ITB formation. The electron temperature outside the N-ITB (denoted by open green triangles (without N-ITB) and open yellow circles(with N-ITB) gradually decrease ($T_e \sim 0.3kev$) as density increasing. Accordingly, the N-ITB does not change the electron transport outside the N-ITB. It is noted that around the threshold density ($4-5\times10^{12}cm^{-3}$), both-type plasmas with and without N-ITB exist, then the data points are separated into two groups that have different electron temperature. This separation suggests that the phenomena have bifurcation nature.

These observations show good agreement with the radial electric field measurement. Figure 18 shows the radial electric field measured with the HIBP as a function of averaged electron density [45, 47, 49]. The radial electric field inside the N-ITB increases significantly ($E_r \sim 16kV/m$) below the same threshold density, and the shape of the potential profile is transformed to the dome structure, then the large radial electric field and shear are created at the barrier location. In contrast, the radial electric field above the threshold density stays at $\sim 100kV/m$, there is no dome structure, hence, no bifurcated state is observed. These observations clearly exhibit that the increase in the temperature is closely correlated to the creation of the radial electric field of the N-ITB formation.

The radial electric field has two bifurcated states below the threshold density even if in the low density ($n_e < 3 \times 10^{12} cm^{-3}$), of which result is contrasted to the density dependence of the electron temperature. This is because the plotted radial electric fields include the wider variety of the N-ITB plasma than that is plotted in figure 17. The electron temperature profile corresponds to another state of the radial electric field in the low density might be found by further investigation.

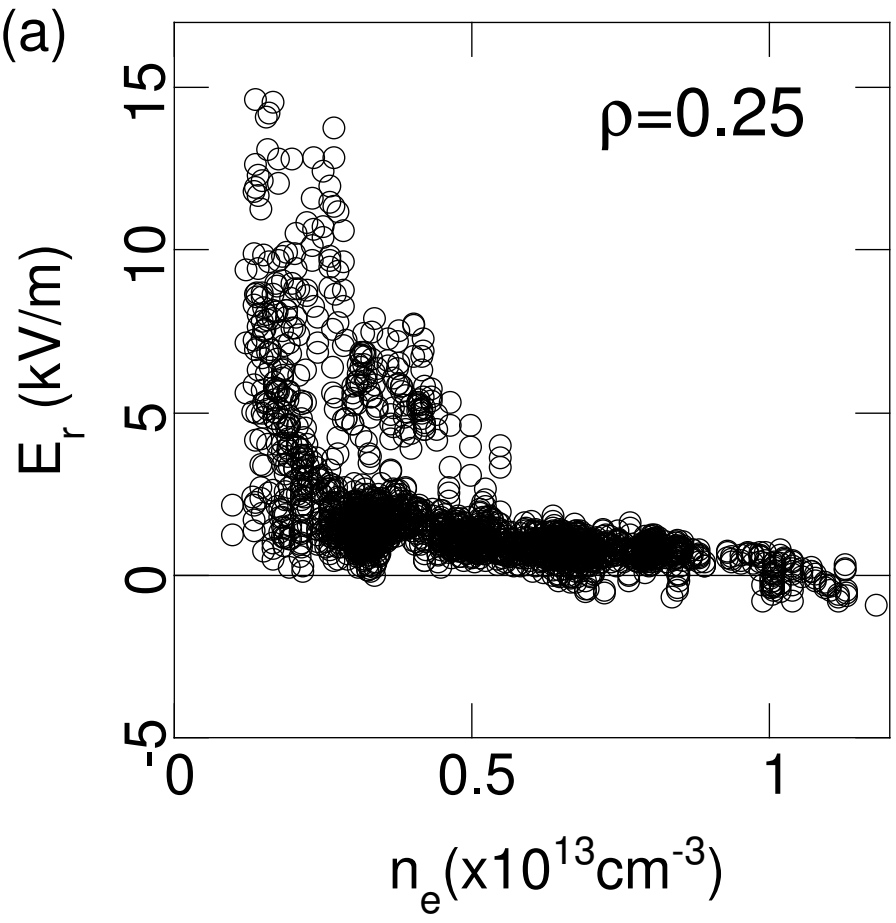

Figure 18: **Dependence of the radial electric field at** $\rho = 0.25$ **on averaged electron density.**

3.2.7 Expansion of Operational Regime to High Density Plasma

As is described in the above section, since the condition for N-ITB formation depends on the plasma density, it is required to lower the density to improve plasma confinement. To achieve the necessary plasma performance for the fusion reactor, raising up the stored energy that is

the product of plasma density and temperature, is important, so that the N-ITB formation for high density is indispensable. The formation of the N-ITB also depends on the magnetic field strength. We can demonstrate higher density ECH plasma with N-ITB in higher magnetic field.

The experiments are carried out at $B_T = 1.76T$ that is two times as high as the above reported experiments, and the plasma is heated using the following two EC heating techniques: (1) second harmonic heating (106GHz) (2) fundamental heating (53GHz).

For the first case, the profile of the electron temperature and density are shown in figure 19. Here, the injected power is $\sim 250kW$, the central electron temperature increases up to 1.9 keV, and clearly the large electron temperature gradient ($15keV/cm$) is mildly formed at $\rho = 0.3$ which exhibits the formation of N-ITB. An achieved central density is $\sim 9 \times 10^{12} cm^{-3}$, which is two times higher than the above mentioned low field experiment. This result is unable to prove the threshold density shift in the higher magnetic field, however shows a possibility of the expansion of the operational regime of the N-ITB to the higher density region.

In the second experiment, P_{inj} is $\sim 180kW$, and the central temperature increases up to $1.8keV$. The large electron temperature gradient ($0.25keV/cm$) is also produced at $\rho \sim 0.3$ that is almost the same location as in the experiment with the low magnetic field. Here, the achieved central density is $\sim 8 \times 10^{12} cm^{-3}$, which is almost same level as the second harmonic experiment. The threshold density is also increased due to the higher magnetic field strength.

For realization of the reactor, it is preferable to sustain a good performance plasma as long as possible, so that it is important to provide answer to whether it is able to maintain N-ITB formation for a long period or not. The following result demonstrates the possibility of the long pulse operation of the N-ITB plasma. Through long pulse operation of the gyrotron, it can be successful to sustain the ECH plasma with N-ITB during $\sim 100ms$ that is only limited by the capability of the gyrotron, as shown in figure 20. In this plasma, the maximum central electron temperature and the density are $\sim 2keV$ and $\sim 3 \times 10^{12} cm^{-3}$ at $P_{inj} \sim 120kW$, respectively. In

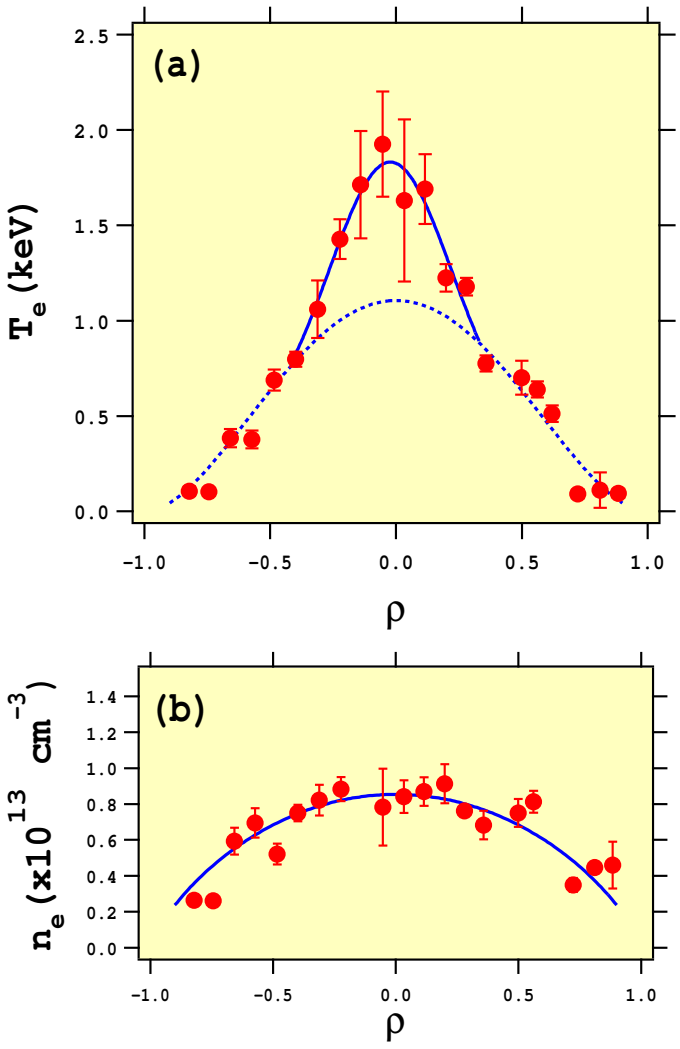

Figure 19: **Electron temperature (a) and density (b) for high field N-ITB experiment (**$P_{inj} = 250kW$**,** $B_T = 1.76T$**). The achieved central density is** $\sim 9 \times 10^{12} cm^{-3}$

this discharge, the modulation of the central electron temperature from 1.5 keV to 2 keV with the period of ~ 20ms is observed. This phenomenon suggests the possibility that the electron confinement is pulsated in accordance with the potential pulsation that is observed with HIBP measurement on CHS [46]. The potential pulsation is caused by the transition between two or three bifurcated states. The period of the potential pulsation (2-3 ms) is shorter than that observed for the electron temperature. However, this might be explained by the repetition rate of the YAG laser fired (10s): an alias effect that usually causes the problem to digitizer occurs in the temperature measurement.

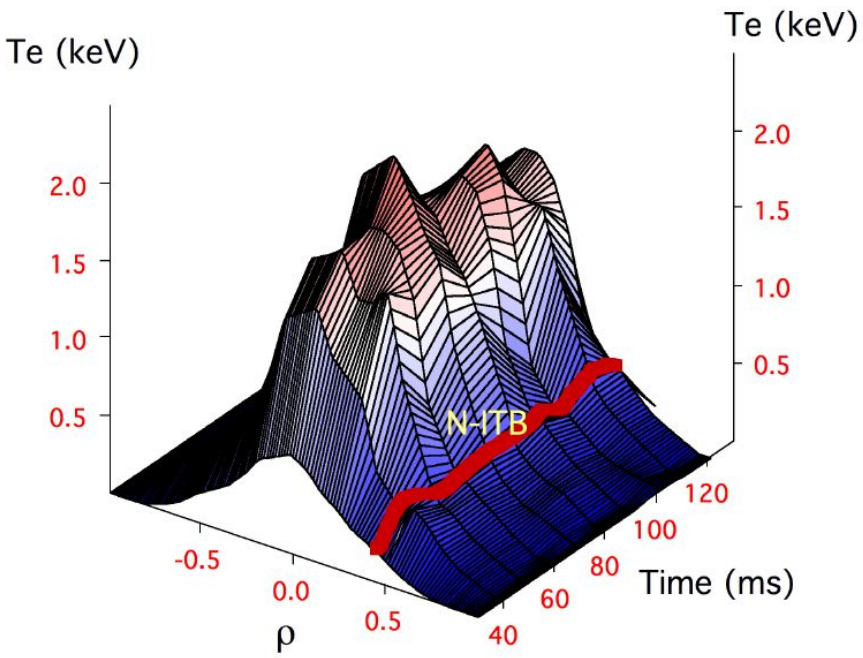

Figure 20: **Long pulse operation of N-ITB plasma.** P_{inj} = 120kW **at 53 GHz,** B_T = 1.76T

3.3 N-ITB Experiments for EC heated NBI Plasma

3.3.1 Introduction

In tokamak experiments, the ITB improves not only electron thermal transport but also ion thermal and particle transports.

In the above described N-ITB experiment on CHS, when the plasma is produced with the electron cyclotron heating only ,though the electron temperature increases up to $\sim 4keV$, the change in the ion temperature profile structure and transport is not clear as shown in figure 21. The ion temperature is measured with the charge exchange spectroscopy by a diagnostic neutral beam injection. In addition, the density profile shape is flat or hollow, and it is not clearly observed that the density gradient that suggests the improvement of the particle transport is produced in the N-ITB plasma.

However, in the next experiments for N-ITB, when the plasma is heated by the NBI and ECH is superposed as an additional heating, the new type of the N-ITB formation has been observed, where the ion temperature increases as well as the electron temperature.

It is a critical problem for understanding the N-ITB of the helical plasma to investigate characteristics of the ion thermal and particle transports. In this section, the experimental observations of the new N-ITB plasma for the EC heated NBI plasma are reported.

3.3.2 Charge Exchange Spectroscopy Measurement for Ion Temperature in N-ITB Plasma

It is important to measure precisely ion temperature profile for investigating the ion transport and confinement characteristics. Charge exchange spectroscopy (CXS) method is utilized for the ion temperature and toroidal rotation velocity profile measurements on CHS [51]. In the CXS measurement, the radiation from charge exchange reactions of the neutral beam is contaminated by background radiation from the cold plasma edge, which is so-called a cold component. In this respect, the CXS measurement on CHS has an advantage to have sophisticated method by using two sets of optical-fiber arrays that are installed on and off the neutral beam

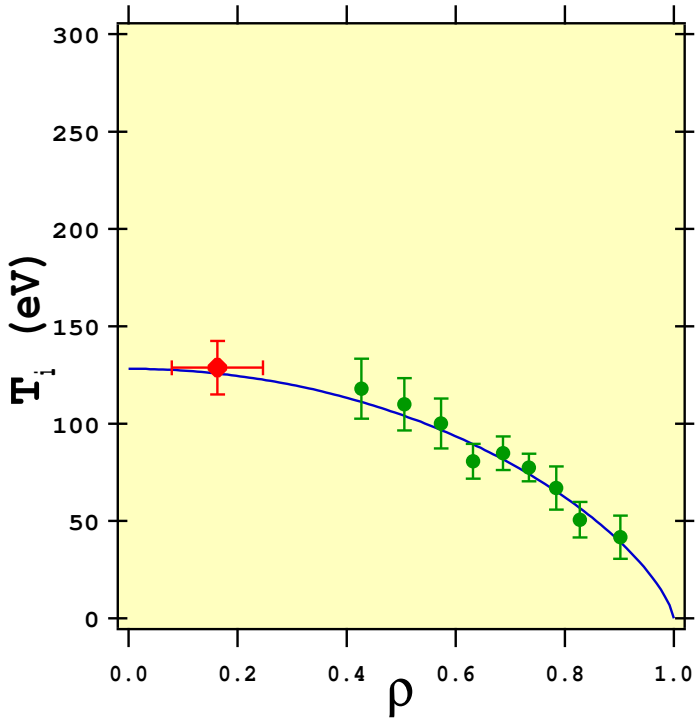

Figure 21: **Ion temperature profile measured with the charge exchange spectroscopy by a diagnostic neutral beam injection for ECH plasma with N-ITB**

line and a charge-coupled device (CCD) as a two-dimensional detector to measure multichordal charge-exchange profiles [CVI 529.2 nm] and background simultaneously. Consequently, a lot of spatial channels (30 ch.) are obtained using the CCD, while the time resolution is $\sim 20ms$ due to the integration time of CCD.

3.3.3 Simultaneous Increase of Electron and Ion Temperature in N-ITB Discharge in EC heated NBI plasma

In this section, the characteristics of the new type N-ITB in the EC heated plasma are described, where both electron and ion temperatures simultaneously increase. Figure 22 shows the typical time evolution of the central electron and ion temperatures and the line averaged electron density for the N-ITB discharge. The electron and ion temperatures are measured at 10 and 20 msec. intervals, respectively. NBI discharge without the second pulse of ECH is plotted in the same figure as a reference.

In plasma discussed here, the target is produced by the first pulse of 53.2GHz 2nd harmonic

ECH($P_{inj} \sim 130 - 150kW, 20 - 40ms$), then heated and sustained by the NBI ($P_{inj} \sim 0.7MW$). The NBI is tangentially injected into the plasma. The magnetic field is 0.88T and the magnetic axis of the plasma is 92.1 cm. When the second pulse of ECH is superposed to the NBI plasma (60-120 ms), the electron temperature increases up to $\sim 3keV$ with a sharp temperature gradient ($dT_e/dr \sim 20keV/m$) ,as is shown in figure 23 (a), which suggests the improvement of the electron transport by forming the ITB.

The difference between the plasmas with and without the N-ITB is ascribed to whether the density is below the critical value or not. As shown in figure 23 (c), the electron density for the plasma with the N-ITB ($n_e \sim 3 - 4 \times 10^{12} cm^{-3}$) is slightly lower than that for the plasma without the N-ITB ($n_e \sim 5 - 6 \times 10^{12} cm^{-3}$). The condition of the critical density ($n_e \sim 4 \times 10^{12} cm^{-3}$) under which the N-ITB is created is discussed later. As the electron density gradually increases (figure 22 (c), red curve), the central electron temperature decreases to $\sim 1keV$, which is one-third of that with N-ITB ,and the sharp temperature gradient disappears. In contrast, the electron temperature remains almost constant ($\sim 150eV$) during the plasma discharge for the plasma without the ECH.

Figure 23 (a) shows the electron temperature profile of N-ITB plasma. It also shows profiles of EC heated NBI plasma without N-ITB. When the N-ITB is produced, the steep electron temperature gradient is produced at $\rho \sim 0.4 - 0.5$.

These characteristics are generally similar to the results of the previous N-ITB ECH experiment without NBI. However, the significant difference is in the electron temperature profile: the improved confinement region is expanded in the present experiment and the temperature profile has ”bell” shape rather than ”dome” shape which was observed in the above described ECH experiment. For N-ITB plasma, the foot point of the enhanced region of the electron temperature is located at the outer location ($\rho_{e-footpoint} = 0.4 - 0.5$) compared to the previous ECH N-ITB experiment ($\rho_{e-footpoint} = 0.3 - 0.4$). The stored energy of the new N-ITB is two times larger

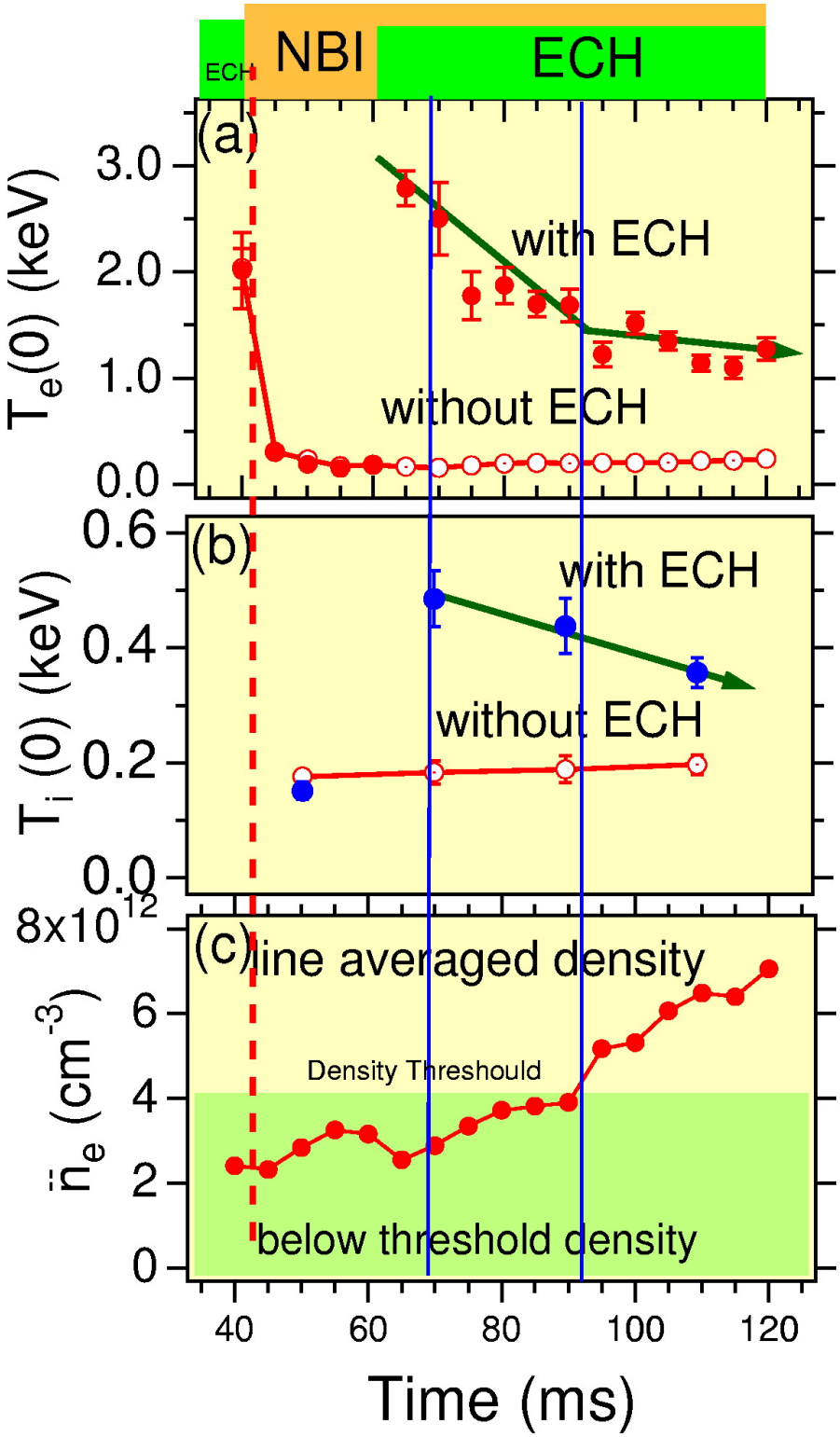

Figure 22: **Time evolution of the typical EC heated NBI discharge with N-ITB and without N-ITB (a) electron temperature (b) ion temperature (c) line averaged density**

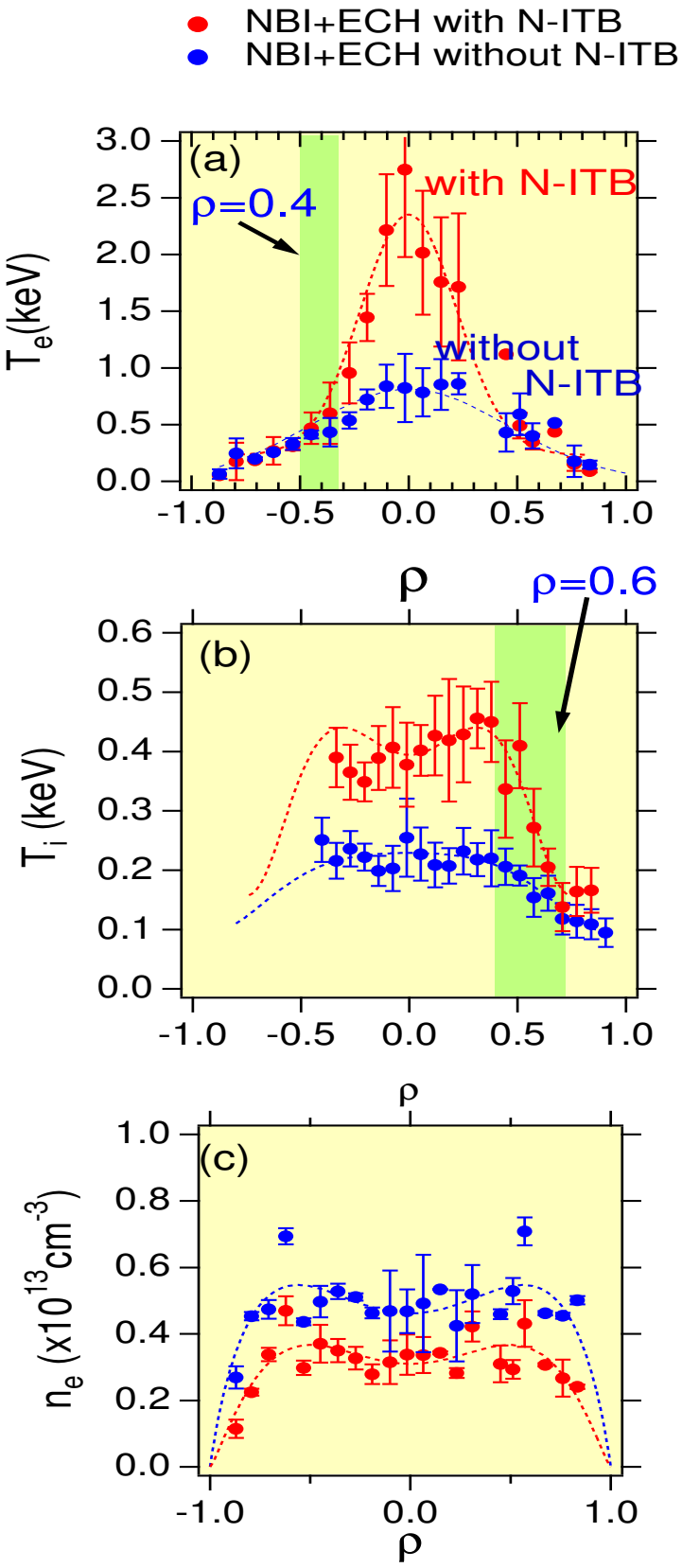

Figure 23: **Radial profiles of EC heated NBI plasma with N-ITB. (a)electron temperature (T_e) (b) ion temperature (T_i) (c) electron density (n_e). The red circles refer to N-ITB. The blue circles denote refer to no N-ITB.**

than that of the ECH plasma with the N-ITB by the expansion of the improved region.

The ion temperature that is measured with the CXS simultaneously increases ($T_i(0) \sim 400 - 500eV$) by two to three times compared to the plasma without N-ITB. It is clearly different from the ion temperature (150-200 eV) of the NBI plasma without the N-ITB, of which temperature is in the same level as the temperature in the ECH plasma. The sharp ion temperature gradient is also produced (8-12 keV/m) at the location of $\rho \sim 0.4 - 0.7$. The foot point for ion temperature appears at outer position ($\rho_{i-footpoint} \sim 0.7$) than that for electrons. In contrast, for the NBI plasma without ECH the ion temperature remains almost constant ($T_i \sim 150eV$) during the discharge that is same temperature as the electron.

It is noted that the signal from the impurity lines that is included in the CXS is negligible. It is confirmed from the direction of the plasma rotation that is derived from the CXS: the intense light from the impurity lines result in being opposite as a mistake for inside and outside of the plasma cross section. However, the direction of the plasma rotation is correct for this experiment.

In addition, the neutral particle analyzer (NPA) is also used for ion temperature measurement. Figure 24 shows the spectrum of the NPA for the EC heated NBI plasma with N-ITB. The spectrum clearly shows that the ion temperature is about 400 eV. These results are in good agreement with the result of CXS measurement.

When the N-ITB is formed, the density profile is almost flat as shown in figure 23 (c), thus the mechanism for the high ion temperature is not the same as the high Ti mode [52, 53], because the High T_i mode is caused by the density peaking due to gas-puff switched off.

Figure 22 (a) shows that the ion temperature slowly goes down as the density increases. Figure 25 shows the temporal evolution of the ion temperature profile. With second pulse of ECH, the ion temperature gradient grows up and the sharp shoulder of the temperature profile is produced. When the averaged density exceeds the threshold for N-ITB at 80 ms, the ion

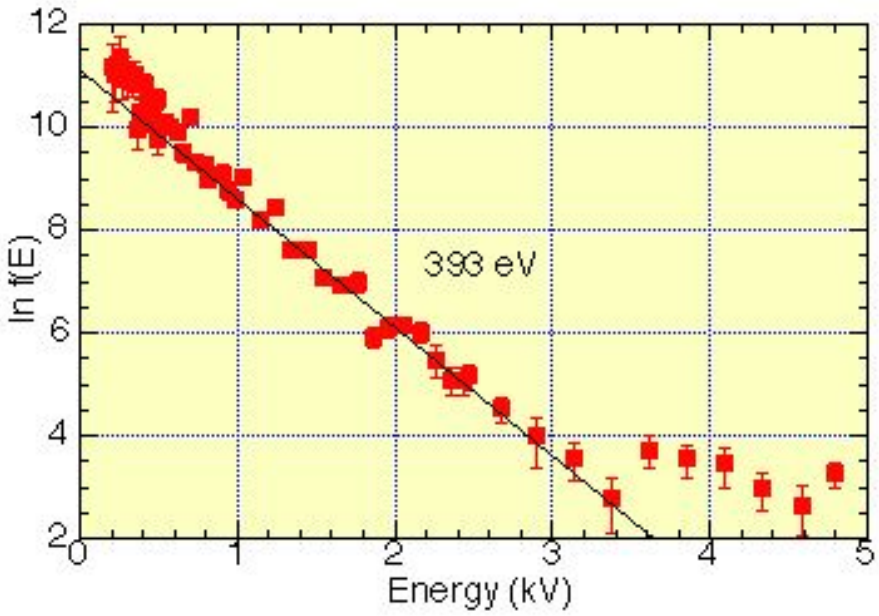

Figure 24: **NPA spectrum in EC heated NBI plasma with N-ITB. The fitting shows that the ion temperature is** $\sim 400eV$**.**

temperature gradient quickly decreases and the shoulder disappears. However the decrease in the central ion temperature is relatively slow. After ECH is turned off, the ion temperature still remains around 400eV in spite of the density increase to $4 - 5 \times 10^{12} cm^{-3}$, which is above the threshold. To demonstrate the characteristics of the temperature reduction, the time evolution of the electron and ion temperatures is plotted as as function of the density as shown in figure 26, because the formation of the N-ITB depends on the plasma density. In spite of the disappearance of the N-ITB above the threshold density $n_e \sim 4 \times 10^{12} cm^{-3}$, the ion temperature is gradually reduced as the electron density increases, while the electron temperature rapidly decreases until the threshold density, then gradually decrease.

One possible reason for this sustainment of the good ion thermal confinement is due to the fraction of the ion heating increase by the NBI relative to the electron heating. However, the electron temperature quickly dropps than the ion temperature decrease, as shown in figure 26, thus the further investigation is required for resolving the problem .

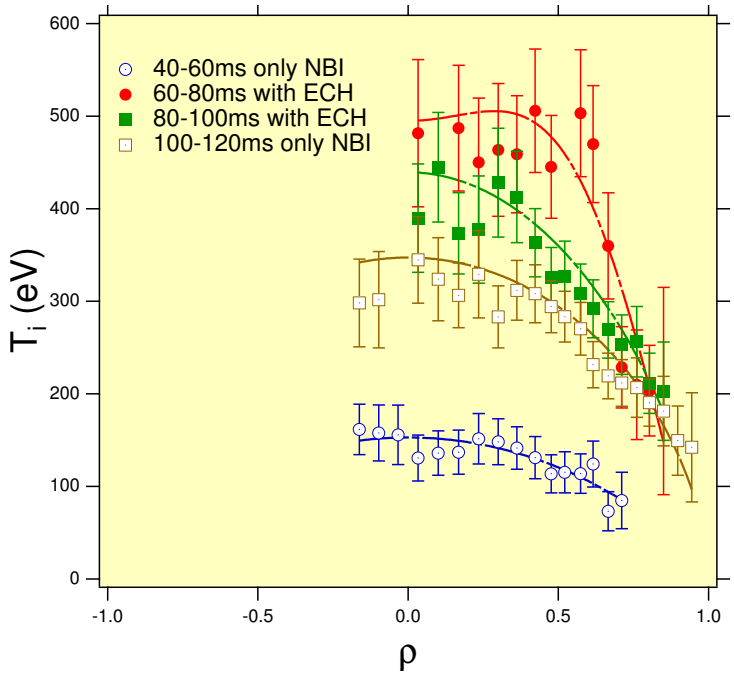

Figure 25: **Time evolution of the ion temperature profile in EC heated NBI plasma with N-ITB. The open circles and squares denote NBI phase in 40-60 ms, and 100-120 ms. The closed circles and squares denote ECH+NBI phases 60-80, and 80-100 ms, respectively.**

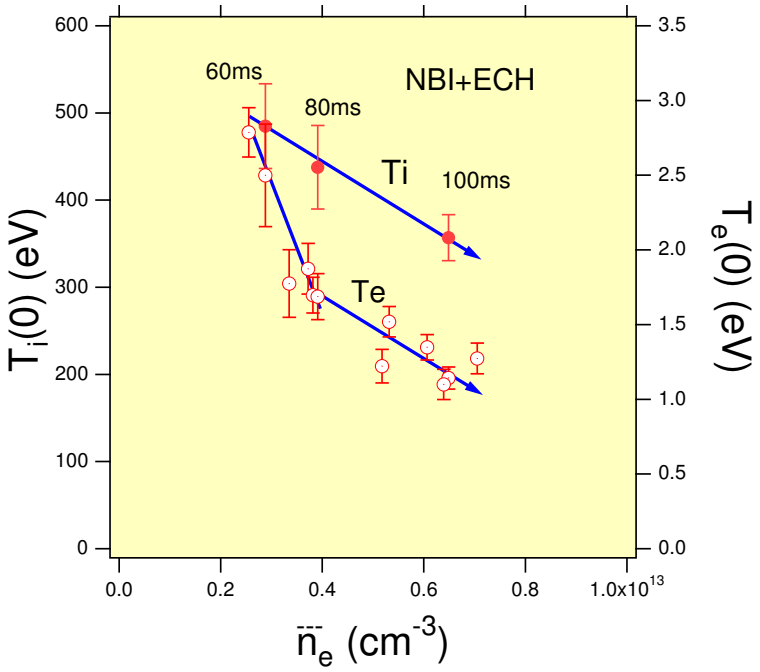

Figure 26: **Electron and ion temperatures are plotted as a function of an averaged density for the density increasing phase.**

3.3.4 Effect of EC Resonance Zone and Critical Density on N-ITB Formation of EC Heated NBI Plasma

Operation regime is investigated for the EC heated NBI plasma. Dependence of the N-ITB formation on the location of the EC heating resonance zone has been investigated.

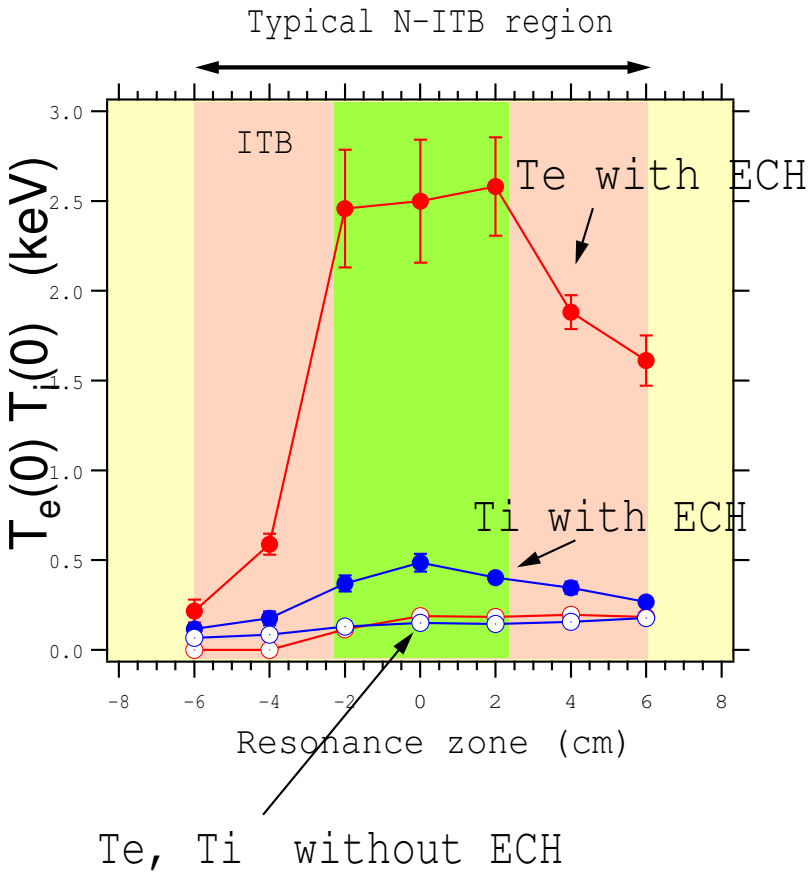

Figure 27: **Achieved central electron and ion temperatures as a function of location of the resonance zone for ECH on and off cases. Closed red and blue circles denote the electron and ion temperatures with ECH, respectively. Open red and blue circles denote the electron and ion temperatures without ECH, respectively. When the resonance zone is located in the plasma center (**$-2cm < R_{resonance} < 2cm$**), the N-ITB is formed.**

The target plasma produced by 53 GHz gyrotron ($P_{inj} \sim 135kW$) is sustained by NBI heating ($P_{inj} \sim 620kW$). When second pulse of the 53 GHz gyrtoron is injected into the NBI plasma, the steep electron and ion temperature gradients are created, which indicate the formation of the N-ITB. The shift of the resonance zone is slightly caused by variation of the magnetic field strength and the focus point of EC heating.

Figure 27 shows the achieved central electron and ion temperatures for the various resonance location, and both cases of ECH on and off cases are plotted. The increases of the electron and ion temperatures have been observed only when the plasma is heated around the magnetic axis ($-2cm < R_{resonance} < 2cm$), then the steep temperature gradient is also created. The area is narrower than the region of the N-ITB ($-10cm < R_{N-ITB} < 10cm$). When the plasma is heated in the outer region than the above region ($2cm < |R_{resonance}|$), the increase of the temperature is small and the structure of the N-ITB is not clear. This is because the electron temperature profile is broad compared to that in the central heating. These results suggest that the transition from the ion root to the electron root does not occur due to the low electron temperature. The temperatures are very low when the resonance zone located in the inboard region ($R_{resonance} < -2cm$), because the plasma is heavily contaminated by sputtering from the inner wall due to the plasma attachment to the wall.

The N-ITB formation in EC heated N-ITB plasma also strongly depends on the plasma density similar to the ECH experiments above described.

Figure 28 (a) and (b) show the dependence of the central electron temperature and the temperature gradient at the N-ITB on the averaged density. When the averaged electron density is below the threshold density ($n_e \sim 4 \times 10^{12} cm^{-3}$), the central electron temperature considerably increases for the plasma with ECH. As shown in figure 28 (b), the gradient of the electron temperature at $\rho = 0.4$ is also raised up to $\sim 30 keV/m$ from $\sim 15 keV/m$ and the profile shape is transformed to the dome structure that exhibits the formation of the N-ITB. Then, the electron temperature dependence on the density increases to $T_e \propto n_e^{-1.6}$ below the threshold density. In contrast, as the density decreases the central electron temperature is gradually reduced, and the electron temperature gradient remains constant level for the plasma without the ECH. The threshold density and other characteristics are very close to the ECH N-ITB experiments except the electron temperature increase in EC heated NBI plasma is larger.

The dependence of the ion temperature on the density is the same as the electron temperature.

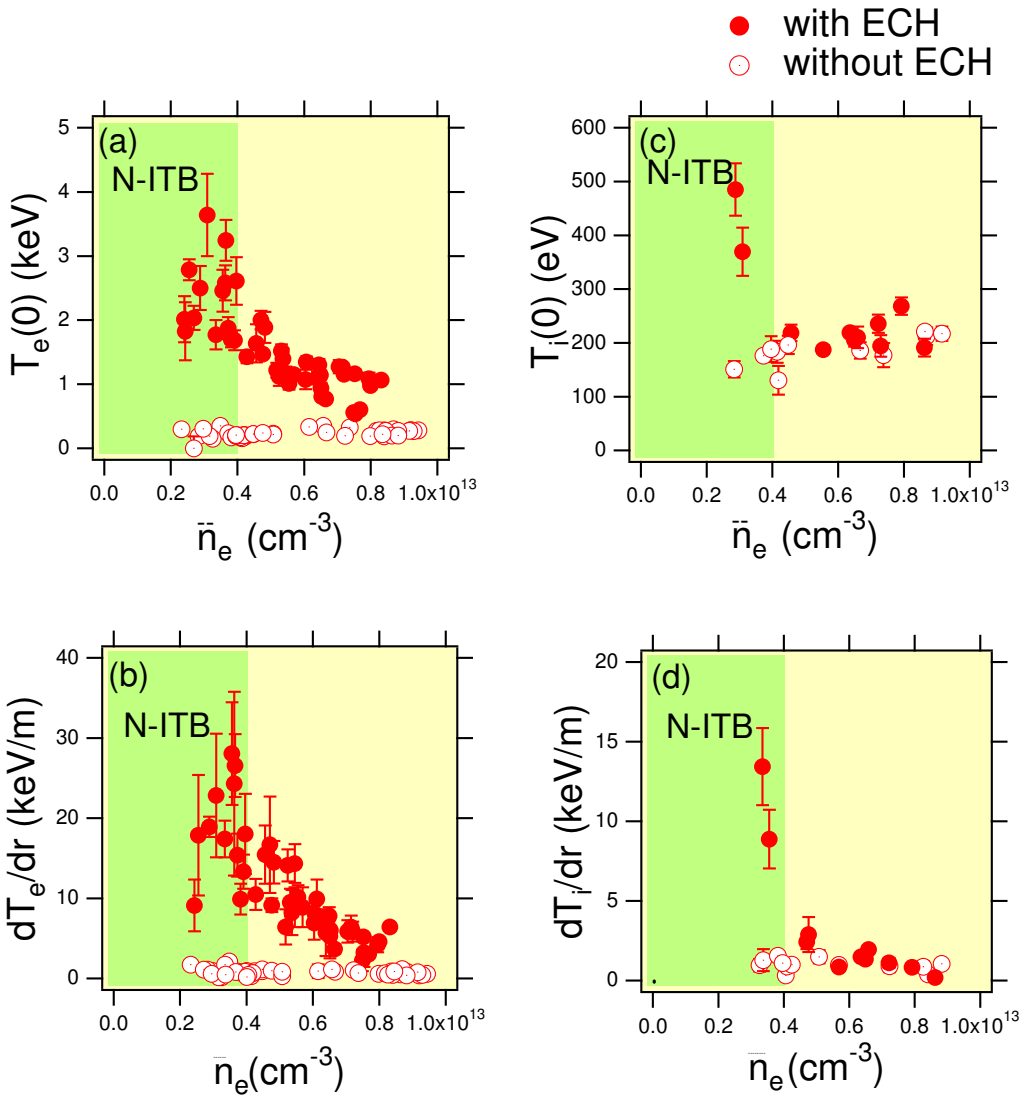

Figure 28: **Central electron (a) and ion (c) temperature and electron temperature gradient (b) and ion temperature gradient (d) as a function of line averaged density. The close circles denote the plasma with ECH. The open circles denote the plasma without ECH.**

As shown in figure 28 (c), the central ion temperature rapidly increases up to $\sim 500eV$ from $\sim 200eV$ by the application of ECH when the density is lower than $3-4\times10^{12}cm^{-3}$. On the other hand, when the averaged density is above the threshold, the ion temperature of the EC heated NBI plasma is gradually reduced and is almost the same as the NBI plasma without ECH. The ion temperature gradient at $\rho = 0.6$ increases from 2-3 keV/m up to 8-12 keV/m

for N-ITB, while the gradient is comparable to that of the NBI plasma without ECH when the density is above the threshold. In contrast, there is no change in the density dependence on the electron temperature and the gradient below the threshold density for the plasma without ECH.

3.3.5 Radial Electric Field structure of N-ITB Plasma

Potential measurement with the HIBP is also performed for the EC heated NBI plasma. Figure 29 shows the potential profile of the EC heated NBI plasma with and without the N-ITB. The considerably large positive potential is produced for the N-ITB plasma around the plasma core, while the smaller potential exist for the plasma without the N-ITB. This plasma potential ($\phi \sim 900eV$) is two times as large as that ($\phi \sim 400eV$) in ECH experiments above described as shown in figure 12, and the are of the increasing potential by the transition is also significantly expanded to $-0.7 < \rho < 0.7$ from $-0.4 < \rho < 0.4$, while the potential profile without the N-ITB case is same for both plasmas with and without NBI.

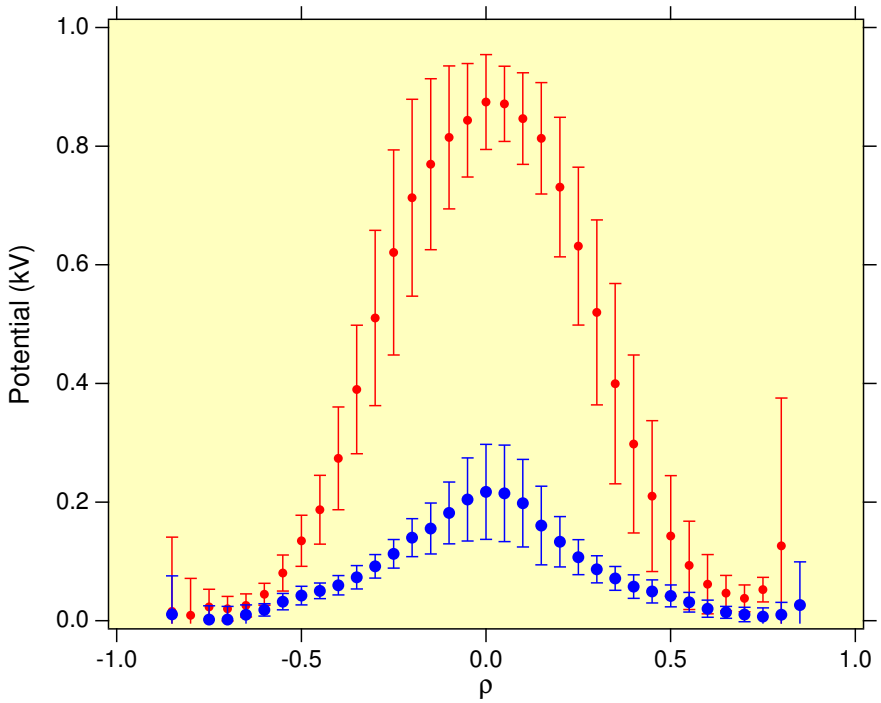

Figure 29: **Potentials of EC heated NBI plasma with and without N-ITB.**

The radial electric field is derived form the potential profile. In the EC heated NBI plasma

experiment, the transport barrier is also accompanied with the large positive radial electric field ($E_r \sim 15kV/m$), which is larger than that ($E_r \sim 6kV/m$) in ECH plasma as shown in figure 30(a). The region of the increased radial electric field is expanded in accordance with the expansion of the increased potential. The plasma without N-ITB also has the smaller radial electric field ($E_r < 5kV/m$). The NBI plasma without ECH has negative and very small radial electric field relative to EC heated plasma.

The radial electric field based on the neoclassical particle flow is estimated analytically from the neoclassical particle fluxes calculated using the analytical formula derived by Kovrizhnykh [57]. Due to the nonlinear dependence of the neoclassical particle fluxes on the radial electric field in the helical plasma , the electric field is reversely determined by the ambipolar condition as follows:

$$\Gamma_e(E_r) = \Gamma_i(E_r), \tag{35}$$

where Γ denotes the particle flux of plasma species with ”e” for electrons and ”i” for ions, respectively [56], which are calculated from T_e,T_i and n_e.

Figure 30 also shows profiles of the radial electric field. In this calculation, the magnetic field strength that is described by the Boozer coordinates is calculated by VMEC code [58]. The poloidal inhomogeneity of B, which is defined by the geometrical inverse aspect ratio in the Kovrizhnykh formula, is replaced by the component derived from the VMEC code [56].

The estimate using the parameters of the plasma with the N-ITB shows that the large radial electric field exists in the plasma core that is created by the transition to the electron from the ion root, while the plasma remains in the ion root in an outer region. On the other hand, when there is no N-ITB, in the core region the radial electric field is smaller in spite of the transition to the electron from the ion root. At the interface between electron and ion root, the three solutions of the radial electric field exist that correspond to the three bifurcated states. For the NBI only

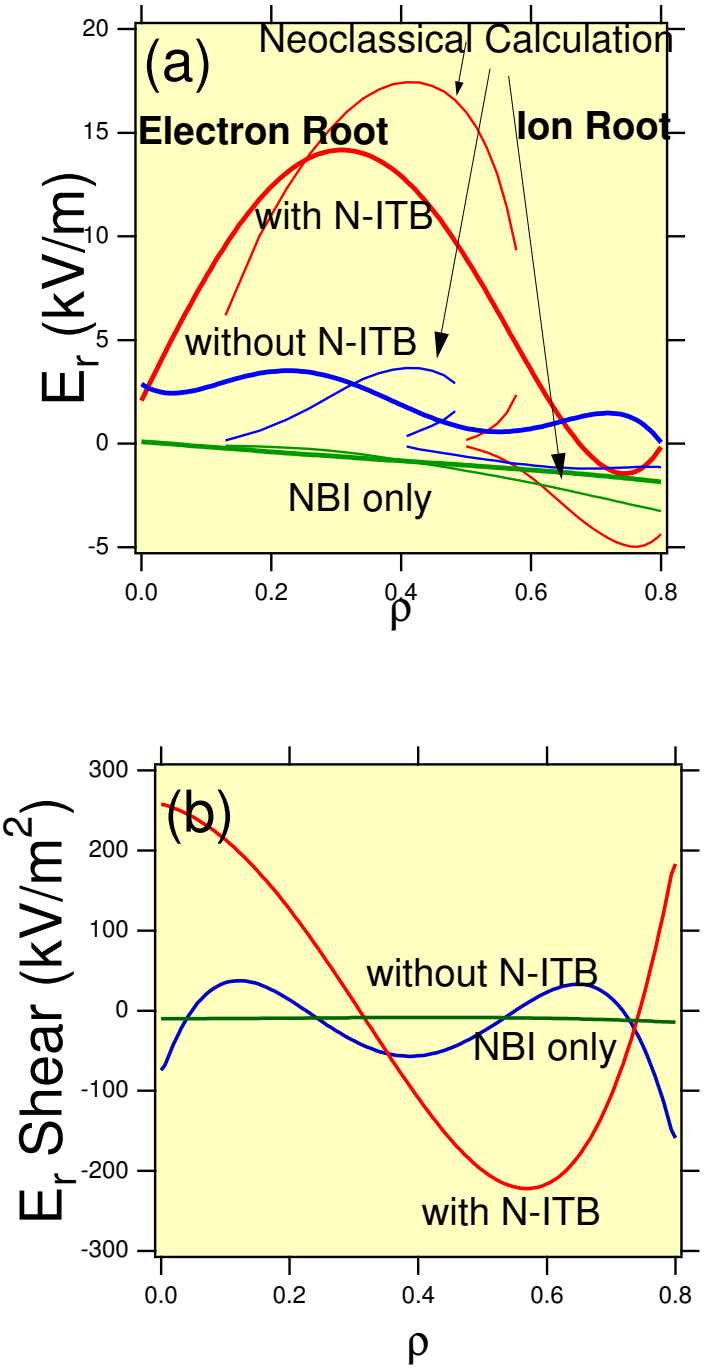

Figure 30: **Radial electric field (a) and field shear (b) derived form the plasma potential with HIBP measurement.**

case, the derived electric field remains in the ion root and is significantly small in the whole plasma. These theoretical estimate and the experimental measurements show good agreement.

However, there is a slight difference between the measurements and the estimate: the absolute value of the derived radial electric field is small both in core and edge regions, while there is a large radial electric field around $\rho \sim 0.4$ in the neoclassical calculation. One possible explanation to the discrepancy is due to the inaccuracy of the measurement in the center and edge region where the accuracy of the measurement severely affects the results of the calculations. Other explanation is inaccuracy of the neoclassical flux calculation: to obtain more accurate flux, the large computations are required by, for example, GNET [59] code that takes into account the fine structure of magnetic field and the contribution to particle fluxes from energetic particles. Especially, large amount of the energetic particles exists in low density (below $1 \times 10^{13} cm^{-3}$) plasma .

Consequently, these theoretical curves qualitatively support the experimental observations. It is clear that the radial electric field of N-ITB is induced by the transition from the ion to the electron root.

3.3.6 Dependence of N-ITB Formation on Magnetic Axis Position

The neoclassical particle flux is considerably affected by the magnetic field structure in the helical plasma. The inward shifted configuration is favorable for drift orbit optimization [60], and provides stable plasma discharge in spite of the unstable characteristics to the Mercier criterion. Accordingly, the shift of the magnetic axis affects the radial electric field [61], then the formation of the N-ITB.

The experiments are performed for EC heated NBI plasma, the parameters are $B_T = 0.88T$, $P_{inj}^{NBI} \sim 500kW$, P_{inj}^{ECH}, and $\sim 160kW$. The locations of the magnetic axis discussed here are 89.9, 94.9, and 97.4 cm. The previous results for 92.1 cm are also plotted as the open circles in figure 31. It is noted that more than 90% of the injected power is absorbed in the plasma center

($\rho < 0.1$), when the electron temperature is above 1 keV, and the deposited NBI power is almost determined by the plasma density.

The electron and ion temperatures are plotted as a function of line averaged density as shown in figure 31 (a) (b), because the characteristic of the N-ITB formation depends on the plasma density. These plots clearly show the difference of the temperature for the various magnetic axis locations on the same density.

In figure 31(a), the green squares and open blue circles denote the central electron temperature when the magnetic axis is located at 94.9 cm, 92.1 cm, respectively. The results of 92.1 cm correspond to the previous EC heated NBI experiments [50]. The achieved electron temperatures ($\sim 4keV$ at $n_e \sim 3\times10^{12}cm^{-3}$) of 94.9 cm are higher than those of 92.1 cm in the particular density range ($2.2 \times 10^{12}cm^{-3} < n_e < 4.2 \times 10^{12}cm^{-3}$). In contrast, the electron temperature of 97.4 cm is lower than that of 94.9 cm and the structure of the N-ITB formation is not clear. However, in the lower density ($n_e \sim 2 \times 10^{12}cm^{-3}$), the electron temperature increases up to $\sim 4keV$. These results suggest the reduction in the threshold density for the N-ITB formation at $R_{ax} = 97.4cm$: the threshold density move to $2 \times 10^{12}cm^{-3}$ from $4 \times 10^{12}cm^{-3}$.

The same characteristics are observed for the ion temperature as shown in figure 31 (b). The highest ion temperature is also achieved when the magnetic axis is located at 94.9 cm. The ion temperature at 97.4 cm goes up to $\sim$ 450 eV when $n_e isbelow \sim 2 \times 10^{12}cm^{-3}$. We can not find the transition to the N-ITB when the magnetic axis is located at 89.9 cm, because the plasma is kept at the higher density caused by the attachment of the plasma to the inner wall.

It is possible to explain the reason for the difference of the transport characteristics by the formation of the radial electric field. The radial electric field based on the neoclassical particle flow is estimated analytically as plotted in figure 32 (a), where the neoclassical particle fluxes are estimated from the analytical formula derived by Kovrizhnykh [57, 56]

The electron thermal diffusivity derived from the neoclassical diffusion is also shown in

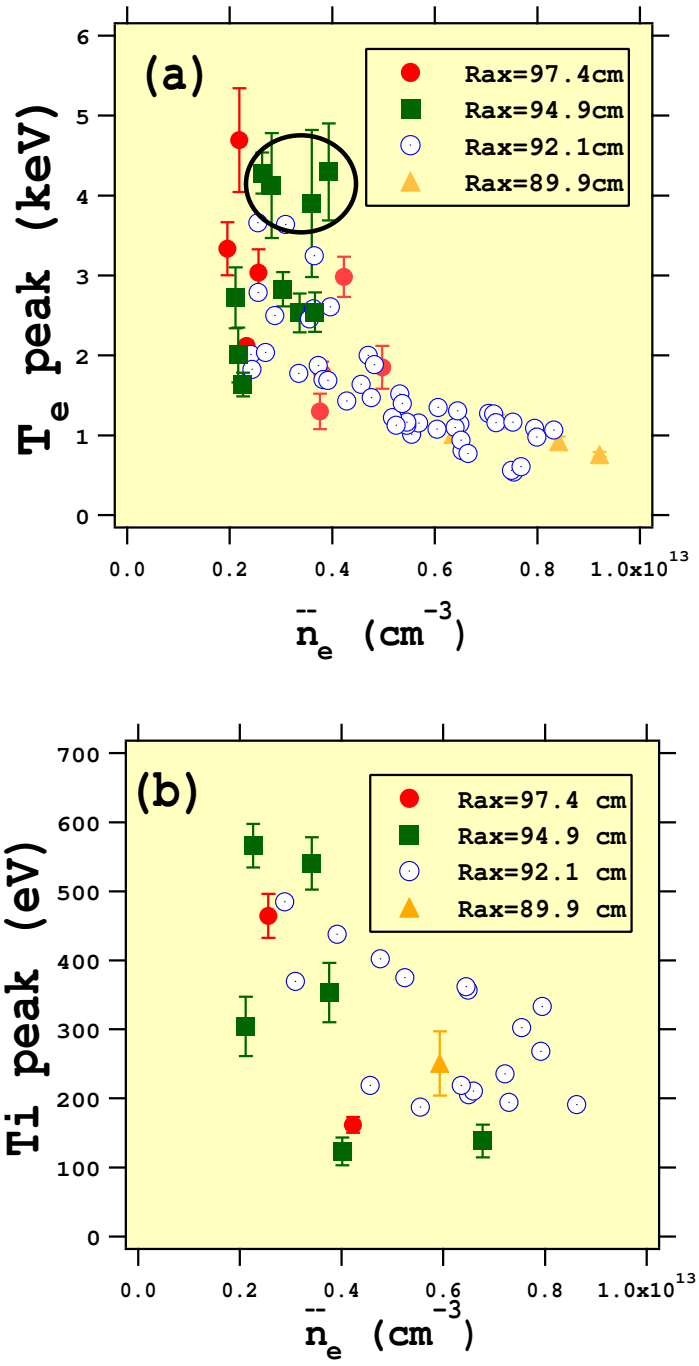

Figure 31: **Dependence of electron (a) and ion (b) temperatures on magnetic axis location as a function of averaged density. The maximum ion temperatures of the whole plasma are plotted because the ion temperature profile is flat inside N-ITB. Data for magnetic axes location of R_{ax} = 89.9, 92.1, 94.9, 97.4 cm are plotted. Open circles denote the data for R_{ax} =92.1 cm, and this position is the standard configuration for CHS experiments.**

figure 32 (b) for the cases of 94.9 cm and 97.4 cm. The previous results for the 92.1 cm are also plotted [50]. The previous results provide a good agreement between the calculated neoclassical value and the radial electric field measurement with HIBP [50]. The parameters used for calculations are as follows: $n_e \sim 2.5 \times 10^{12} cm^{-3}, T_e \sim 4keV, T_i \sim 500eV$ at $R_{ax} = 94.9cm$, and $n_e \sim 2 \times 10^{12} cm^{-3}, T_e \sim 3.5keV, T_i \sim 500eV$ at $R_{ax} = 94.9cm$.

As shown in figure 32(a), the calculations predict that the larger neoclassical radial electric field is created for both 94.9 cm and 97.1 cm. The neoclassical values at 94.9 cm are, moreover, higher than that at 97.4 cm. The formation of the large electric field is ascribed to the higher electron temperature. In the results for the R_{ax}=97.4 cm, the radial electric field is separated into three bifurcated states, while the only single solution exists in the R_{ax}=94.9 case. These values are also higher than the results of 92.1 cm. As show in figure 32(b), the neoclassical electron thermal diffusivity in R_{ax}=94.9 cm is lower than that in R_{ax}=97.4 cm due to the larger neoclassical radial electric field. In addition, the calculated radial electric field shear is also larger in R_{ax}=94.9 cm case compared to the 97.4 cm and 92.1 cm cases. Accordingly, the suppression of the anomalous transport is expected by the $E \times B$ shear [42, 50].

3.3.7 Particle and Impurity Transport

The question whether the N-ITB is able to affect particle transport in the helical plasma or not remains. In tokamak experiments, the sharp density gradient is produced by the ITB, then the particle transport is improved [2, 3, 4, 5, 6, 7]. On the other hand, in the ECH plasma and the EC heated NBI plasma, the profiles of the electron density are flat or hollow shape as shown in figure 9 (c) and figure 23 (c), then it is not observed that prominent symptom of forming the density gradient at the location of the N-ITB. To understand this phenomenon, it is important to consider off-diagonal terms for neoclassical particle flux: it is possible that an increase in the neoclassical flux of the electron temperature gradient compensates a decrease in the fluctuation driven particle flux. Accordingly, additional information to the density profile is

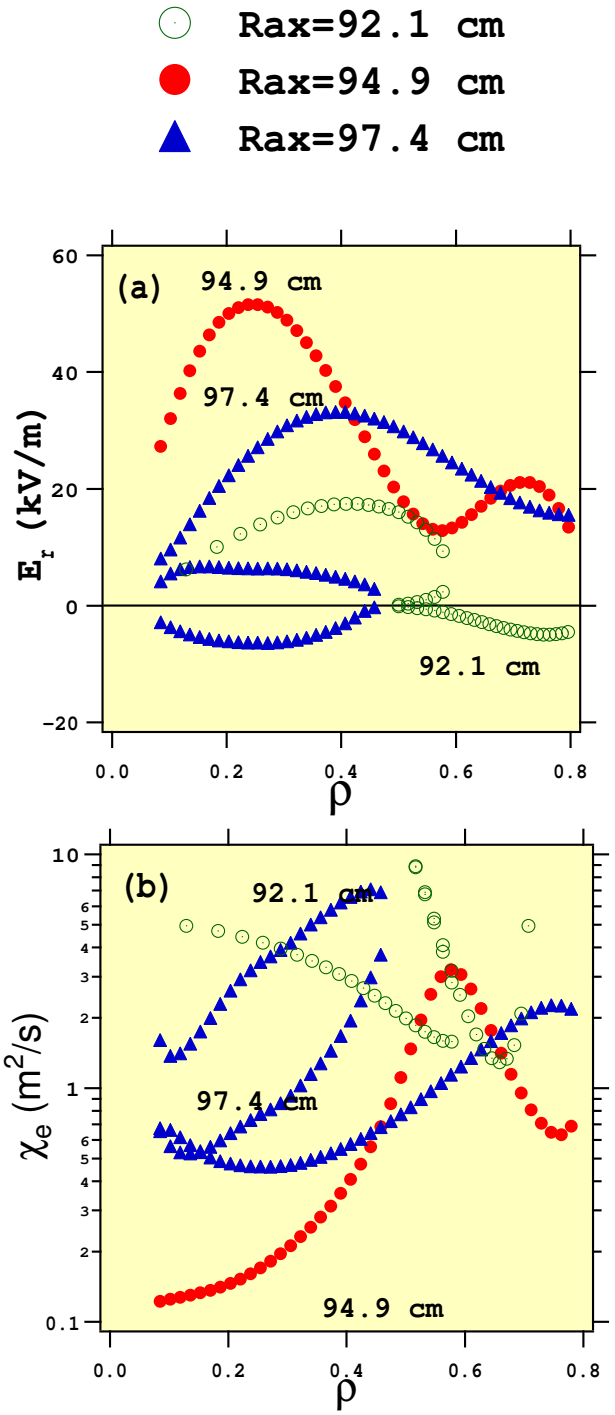

Figure 32: **Estimate of the radial electric field (a) and the electron thermal diffusivity (b) derived from the neoclassical diffusion of the helical plasma. The closed red circles and triangles denote the cases of the magnetic axis position of 94.9 cm and 97.4 cm, respectively. The results of 92.1 cm are also plotted as the open green circles.**

required to study the particle transport by the N-ITB. Following measurements for the impurity transport on the N-ITB provides another information for the effect on the particle transport. The titanium impurity transport was measured with the photon counting two-dimensional x-ray CCD camera [1024x512 pixels] for the EC heated NBI plasma with N-ITB [14]. The CCD camera has an 900mm-thick Be filter and a pinhole of 0.3 mm-diameter. The energy resolution is $3.22 \pm 0.04 eV/electron (16.5 \pm 0.2 eV/ADCcount)$. Because the frame rate is slow (0.2Hz), all emission from the discharge in CHS (100-150 ms) is accumulated. The ionization level of the impurity ions is determined by the balance between the diffusion and ionization. The energy level of TiK_α lines depends on the charge state. Because the energy resolution of the soft X-ray camera is not enough to distinguish individual K_α lines for different charge states, we tried to measure the change of the charge states distribution from the shift of averaged energy of the TiK_α lines. Figure 33(a) shows the energy spectra measured with X-ray CCD camera in EC heated NBI plasma experiments. For the plasma with N-ITB, the averaged peak energy of TiK_α line at $\rho = 0.03$ is 4.72-4.73 keV which is dominated by He-like ions. For the plasma without N-ITB, the peak energy is shifted to 4.68-4.69kV which is dominated by Be-like ions [14]. The energy peak depends on the ionization levels in a given condition of temperature and density. To evaluate the diffusion coefficients of impurity in the plasma, the numerical impurity code MIST and LINES are used.

The impurity flux is expressed as

$$\Gamma = -D(\frac{\partial n_Z}{\partial r}) - n_z V, \tag{36}$$

where D and V are coefficients for the diffusive and convective terms, respectively. In the numerical calculation, the model diffusivity profile as shown is assumed in figure 33 (c): the diffusivity in the core region steps down from the outer region for the case of N-ITB. In addition, because the electron density profile is almost flat during ECH as shown in figure 23(b),

it is assumed that the convective velocity can be neglected (V=0). The free parameters of the diffusivity model are determined by fitting the measured averaged energy peak. The results are shown in figure 33(b). The model shows good agreement with the averaged peak energy for the plasma with N-ITB.

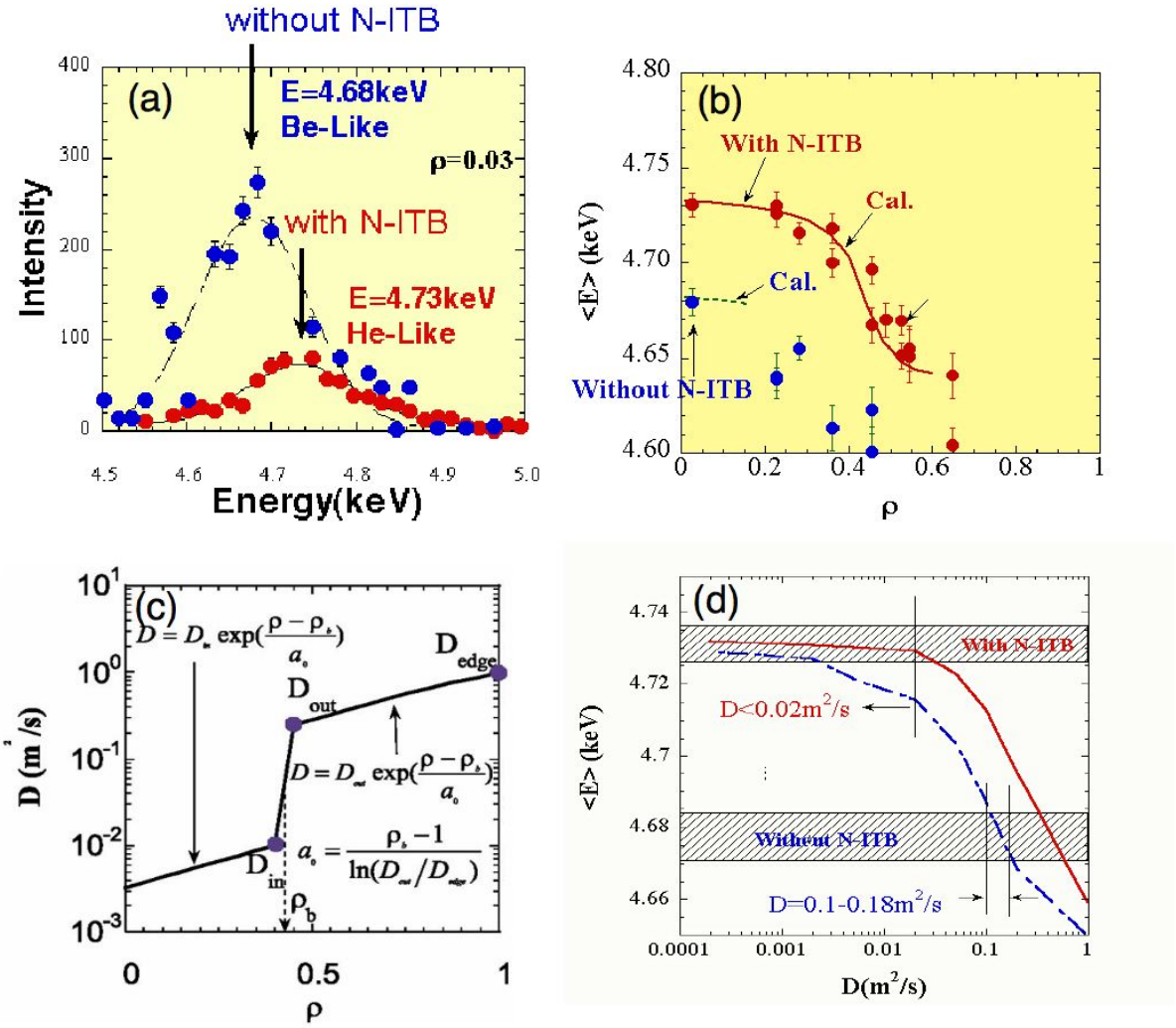

Figure 33: **(a) Energy spectrum for the plasma with and without N-ITB. (b) The radial profile of the energy peak of $TiK\alpha$ lines. A radial profile model of the diffusion coefficient. (d) The calculated averaged energy of $TiK\alpha$ line as a function of diffusion coefficients for the plasma with N-ITB (solid line) and without N-ITB (dashed line).**

The average energy of the titanium K_α lines is plotted as a function of the impurity diffusion coefficients D_{in} as shown in figure 33(d). The solid line denotes the dependence for the plasma with N-ITB, and the dashed line that for the plasma without N-ITB. The core diffusion

coefficient is reduced to $< 0.02 m^2/s$ in the plasma with N-ITB, while it is $0.1 - 0.18 m^2/s$ in the plasma without N-ITB. In the N-ITB discharge, because the transport time scale is comparable to the atomic process time (the ionization and the recombination), the averaged energy of Ti K_α line is sufficiently sensitive to the impurity diffusion. Consequently, the impurity particle confinement is considerably increased inside the N-ITB.

4. Discussions

4.1 Comparison of N-ITB Plasma between EC and EC + NBI Heating from the Viewpoint of NBI Deposition

In the N-ITB experiment with ECH only, the improvement of the ion thermal transport was not identified. This is because the transferred energy to ions from electrons is small for low collision frequency in the high electron temperature that is discussed in next sections.

Once particles of the neutral beam have been charged, the particles slow down by the Coulomb collisions, and the energy is transferred to both ions and electrons. When the particle velocity is high and comparable to the electron's velocity, the electron heating is dominant. When the particles slow down and their velocities have become comparable to the ion velocity, the heating occurs mainly for the ions. Accordingly, in EC heated NBI plasma, the more electron temperature increase in the core region, the larger contribution to the ion heating is given from NBI.

To confirm this, the NBI heating power for the N-ITB plasma is estimated using the Mote Carlo simulation code ,MCNBI code [62]. The results are shown in figure 34. In this calculation, the acceleration voltage is 36kV, the beam current is $\sim 40A$, the port through NBI power $\sim 700kW$, and the density $3.5 \times 10^{12} cm^{-3}$, which are typical parameters of the N-ITB experiments. The fraction of the deposited NBI power to ions is greater than $\sim$ 50%, when the electron temperature is higher than $\sim 1keV$ on CHS, as shown in Figure 34(c) . More than 80% of heating power is transfered to the ions, when the electron temperature is higher than $\sim 2keV$ that is achieved by the N-ITB. On the other hand, the transferred energy to ions in low temperature plasma without the N-ITB ($\sim 800eV$) is only $\sim$ 30%. This dramatic increase of the fraction of the ion heating is one explanation of the formation of the N-ITB in the ion transport.

There is another question whether the increase in the electron and ion temperature is due to the improvement of the confinement or due to the increase in the deposited power of NBI. To

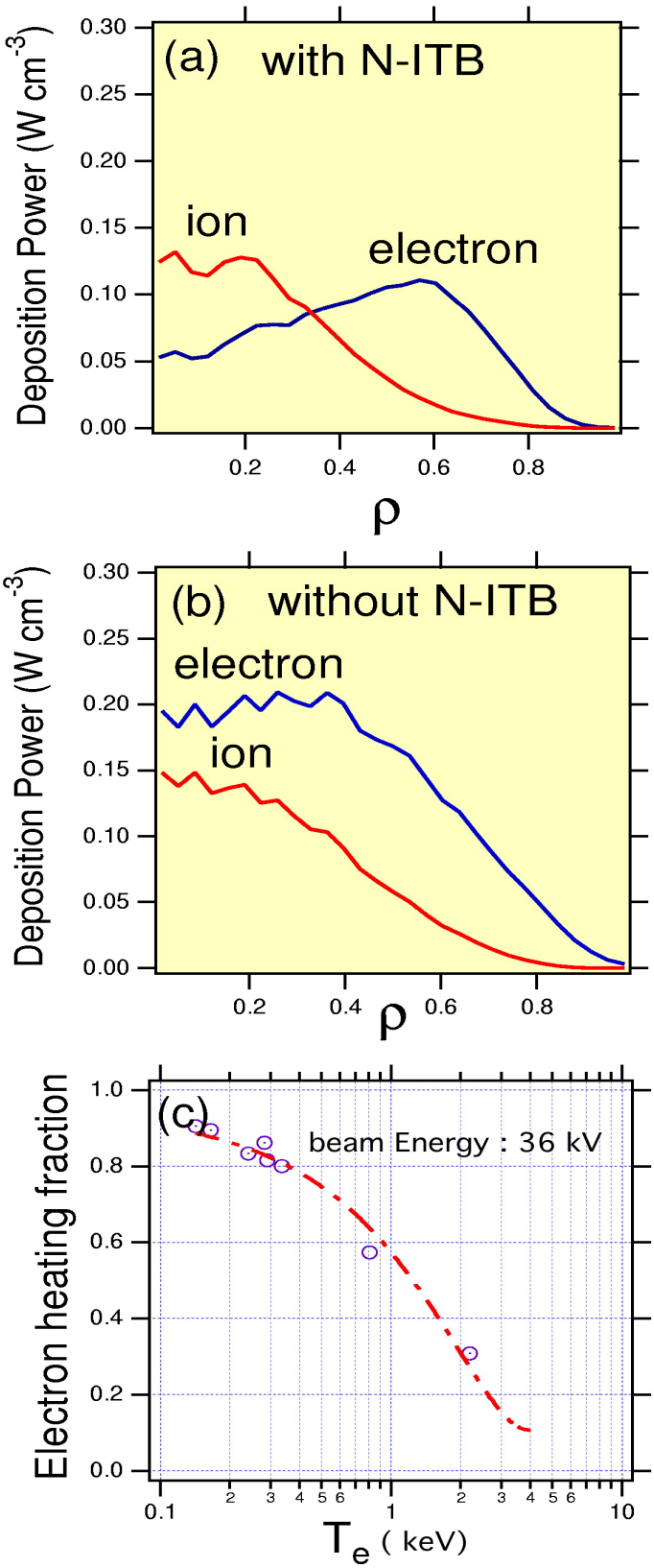

Figure 34: **NBI power deposition profile to electrons and ions for the plasmas with N-ITB (a) and without N-ITB (b). (c) Electron heating fraction of NBI deposition as a function of electron temperature.**

make sure of this, the calculation of the power deposition is carried out with MCNBI code for the N-ITB plasma (figure 34 (a)) and the plasma without N-ITB (figure 34 (b)). The total deposited power is 37 kW for figure 34 (a) and 60kW for figure 34 (b). The calculation uses the real geometry and orbit averaging is made. However, the finite orbit effect during slowing down processes and electric field are not included. First, we consider a difference of power deposition to electrons between the plasmas with N-ITB and without N-ITB. Absorbed ECH power rate is estimated larger than 90% for both cases, so that the heating power by the ECH is approximately $> 100kW$. The deposited NBI powers to electrons in the plasma with the N-ITB and without the N-ITB are approximately $20, 40kW$, respectively. These values are smaller than the absorbed ECH power, so that the difference of the electron heating power between the plasmas with and without the N-ITB is smaller. Moreover, the total deposited NBI power to electrons in the plasma with N-ITB is about 50% compared to the plasma without N-ITB. Consequently, the electron temperature increase in the N-ITB plasma can not be explained by the electron heating power increase.

Secondly, for the power deposition to ions, the results of the simulation show almost the same level of heating power in the core region as shown in figure 34(a) and (b). The fraction of the ion heating to the electron heating increases in the plasma core with the N-ITB, so that the deposited NBI power increases in spite of the low density that triggers the formation of the N-ITB. Although the difference of the density between the plasmas with and without the N-ITB is slight (approximately 30%) , the deposited NBI power for the plasma with the N-ITB is approximately half of that for the plasma without the N-ITB.

Accordingly, although the fraction of the heating power to ions increases by the electron temperature increase, the large increase of ion temperature (two to three times higher) is not explained by the difference of heating power, because of the reduction of the deposited power with the lower density of the N-ITB plasma.

4.2 Estimate of $E \times B$ Shearing Rate

The $E \times B$ shearing rate is essential in quantitative assessment of the $E \times B$ shear suppression of turbulence both for tokamak and helical devices [9, 54, 55]. This theory predicts that the $E \times B$ shearing rate has a strong influence on the suppression of the micro instabilities and is expected to reduce the anomalous transport.

Considerable experiments have been done to test the picture of $E \times B$ velocity shear effects on turbulence [9] for the following various experiments.

1 H-mode with edge confinement improvement seen in limiter and diverter tokamaks, stellarators, torsatrons, and mirror machines produced with a variety of heating and plasma biasing schemes.

2 The confinement improvement in the outer-half of the plasma seen in VH-mode and high internal inductance discharges.

3 The formation of core transport barriers in a number of tokamaks.

These experimental results qualitatively and qualitatively support the $E \times B$ shearing rate theory.

The $E \times B$ shearing rate [9] in the cylindrical geometry is described as follows.

$$\omega_{E\times B} = \frac{(RB_\theta)^2}{B}\left(\frac{\partial}{\partial\Psi}\right)\frac{E_r}{RB_\theta} \tag{37}$$

Here, R is the major radius,B_θ the poloidal magnetic field, B the magnitude of the magnetic field, E_r the radial electric field and Ψ the flux coordinate. This formula exhibits that the $E \times B$ shearing rate is determined not only by the radial electric field shear but also by the magnetic field shear.

Recent nonlinear gyro-Landau fluid simulations [9] have shown complete turbulence stabilization when $\omega_{E\times B}$ is comparable to γ_{MAX}, the maximum linear growth rate of all the unstable

modes in the plasma. The rule $\omega_{E\times B} = \gamma_{MAX}$ has been used in comparison between theory and experiments [9].

The $E \times B$ shearing rate is estimated for the N-ITB plasma on CHS. First, the result for ECH plasma described in the previous section is plotted in figure 35. The shearing rate for the plasma with N-ITB increases up to $\omega_{E\times B} = 2.5 \times 10^5 s^{-1}$ at the region of the barrier location ($\rho \sim 0.2 - 0.35$). On the other hand, the shearing rate is not varied throughout radius for the plasma without N-ITB.

In this calculation, the B_θ and Ψ is calculated by VMEC code [58] assuming $\beta = 0$, because the stored energy is very low due to the low density of the N-ITB plasma.

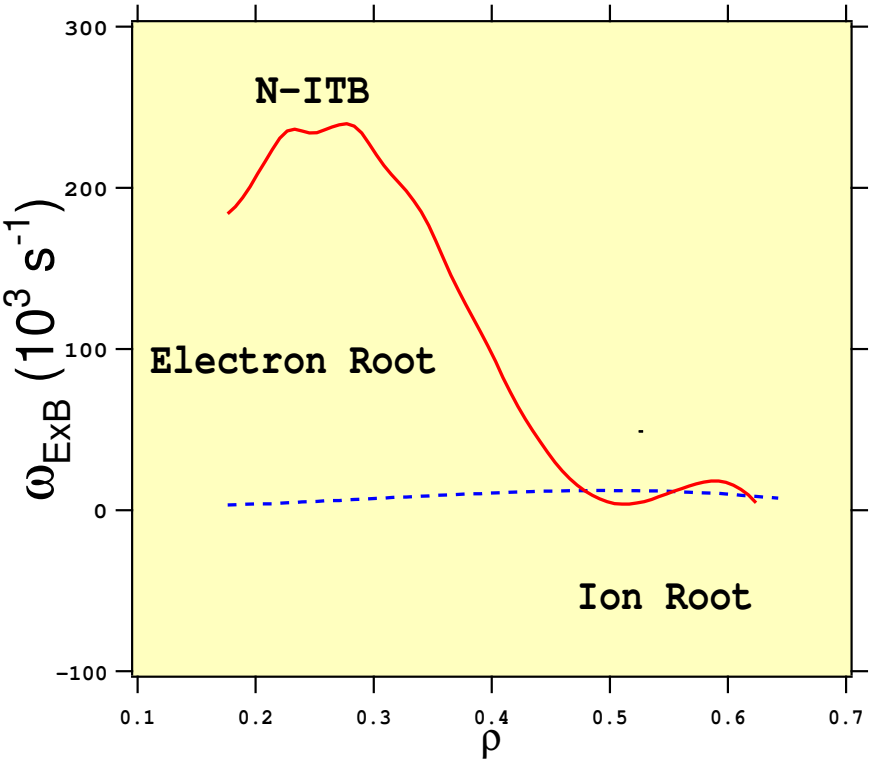

Figure 35: $E \times B$ **shearing rate for ECH plasma. The red and blue lines denote the plasmas with N-ITB and without N-ITB, respectively.**

In EC heated NBI plasma, the similar characteristic is observed, as shown in figure 36. The shearing rate for the plasma with N-ITB increases up to $\omega_{E\times B} = 4.0 \times 10^5 s^{-1}, with dE_r/dr \sim 300 kV/m^2$ that is approximately two times as large as the shearing rate for the ECH plasma. The

peak of the shearing rate exists around $\rho \sim 0.5$ that is outer than the peak position of the ECH plasma with the N-ITB ($\rho \sim 0.25$). Accordingly, the anomalous transport in the EC heated NBI plasma is expected to be suppressed strongly in the outer location than that in the ECH plasma. The $E \times B$ shearing rate ($\omega_{E\times B} \sim 1 \times 10^5 s^{-1}$) in the plasma without N-ITB is smaller. In NBI plasma without ECH, the sharing rate ($\omega_{E\times B} \sim -0.4 \times 10^3 s^{-1}$) is negligible compared to plasma with ECH.

The difference between the $E \times B$ shearing rate and the radial electric field shear is important. As is shown in figure 30, the local radial electric field is maximum around the plasma center with the barrier location ($\rho \sim 0.6$). On the other hand, the shearing rate has an only maximum around the barrier location, and the improvement of the transport is not clear in the plasma center except for the barrier location. Accordingly, the correlation between the N-ITB and the $E \times B$ shearing rate is significant.

The results of deuterium VH-mode plasma experiment in DIII-D tokamak [9] show that the observed shearing rate is approximately $\omega_{E\times B} = 6.0 \times 10^5 s^{-1}$ around the ITB. In this experiment, the shearing rate significantly exceeds the linear growth rate ($\sim 2 \times 10^5 s^{-1}$). Consequently, though the linear growth rate for CHS plasma is not estimated, both shearing rates for the ECH and EC heated NBI plasma are comparable to that at the internal transport barrier observed in Tokamak experiment.

4.3 Method of Transport Analysis

In order to quantitatively estimate confinement properties N-ITB plasma, the transport analysis is carried out to clarify the characteristic of the N-ITB. In the steady state, the heat conduction $Q_{cond}^{electron}$, Q_{cond}^{ion} are expressed as follows.

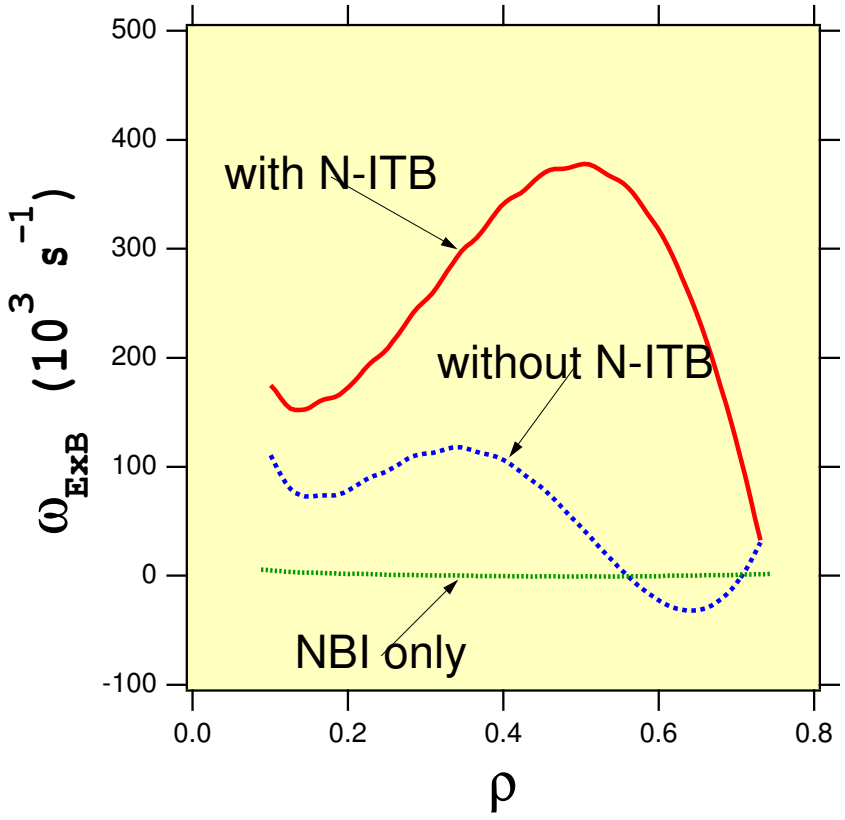

Figure 36: $E \times B$ **shearing rate for EC heated NBI plasma. The red and blue lines denote the plasmas with N-ITB and without N-ITB, respectively. The green line denotes the NBI plasma without ECH**

$$Q_{cond}^{electron} = \frac{3}{2}\nabla(T_e\Gamma_e) - 3\frac{m_e}{m_p}\frac{n_e}{\tau_e}[Z](T_e - T_i) + Q_{ech} + Q_{NBI}^{electron} \tag{38}$$

$$Q_{cond}^{ion} = \frac{3}{2}\nabla(T_i\Gamma_i) - 3\frac{m_e}{m_p}\frac{n_e}{\tau_e}[Z](T_i - T_e) + Q_{NBI}^{ion} \tag{39}$$

Here Γ_e and Γ_i are the radial particle fluxes of the electron and ion ,respectively. m_p, m_e indicate electron and ion mass, respectively, τ_e is electron collision time. The term $\frac{n_e}{\tau_e}[Z](T_e - T_i)$ represents the energy transportation between ions and electrons.

Q_{ech} is absorbed ECH power that is derived by the formula using I. Fidone and G. Granata [64]. Due to the high electron temperature plasma in spite of the low density, all injected power ($P_{inj} \sim 130kW$) reaches the resonance zone and more than 90 % power is absorbed when the electron temperature is above $\sim 1keV$. It is important to estimate NBI power deposition precisely in low density N-ITB plasma where orbit loss and charge exchange loss are dominant. For this purpose, the Mote Carlo method with the particle orbit simulation is carried out for the discussed plasma [62].

The electron and ion thermal diffusivities, denoted by χ_e and χ_i respectively, are defined as

$$\chi_e = \frac{Q_{cond}^{electron}}{n_e\nabla T_e} \tag{40}$$

$$\chi_i = \frac{Q_{cond}^{electron}}{n_e\nabla T_i} \tag{41}$$

.

The electron temperature and density are measured with YAG Thomson scattering measurement. The absolute value of the density includes 20-30 % error mainly comes from out of alignment of the optical path, so that the YAG Thomson density is corrected using the line averaged density measured with the HCN interferometer. The ion temperature is measured with the charge exchange spectroscopy. The data on coordinates are translated into a flux surface function, on of which coordinate is denoted by $\rho(= r/a)$. The data are fitted using appropriate functions such as a parabolic, gaussian, hollow, polynomial functions on account of reducing

the data scattering that comes from the local value measurement and its derivative.

The energy transport term between electrons and ions is derived using the Proctr-MOD code [63]. It is noted that the energy transport term is negligible compared to the other terms in the above equations for the discussed plasma due to the low density. However, this term is taken into account for evaluating precisely the transport characteristics.

The error included in the derived thermal diffusivity is mainly due to the calculated gradient for the electron and ion temperature profiles that are included in the denominators of Eq.41. The fine structure of these temperature profiles, which should be observed when its scale length is larger than the spatial resolution of the diagnostic devices, affects the evaluation of the temperature gradients. The evaluation of the gradient caused by the smaller scale length structure than the resolution is difficult. In this transport analysis, the error is estimated as a maximum error derived only from errors of measurement on each local point, and the error from the fine structure smaller than the scale length is not taken into account. Thus, the fine structure in the derived thermal diffusivity is unable to be discussed.

4.4 Characteristic of Electron Transport of N-ITB

In this section, the electron transport property of N-ITB plasma is discussed for the ECH plasma. The results of the transport analysis are shown in figure 37.

The calculation is carried out using the parameters (T_e, n_e, P_{inj}^{ECH}) of above described ECH plasma, as shown in figure 9. An ion temperature of a typical ECH plasma is used, as shown in refiontempECH, which has almost same electron temperature and density . This ion temperature is $\sim 130eV$ measured with a charge exchange spectroscopy with a diagnostic NBI which is considerably lower than the electron temperature ($\sim 2.2keV$), because the calculated energy transport between electrons and ions is below 10% of the deposition power to the electrons.

The electron thermal diffusivity is shown as the solid line in figure 37 for both plasmas with N-ITB and without N-ITB with the range of the error bar estimated. The electron thermal

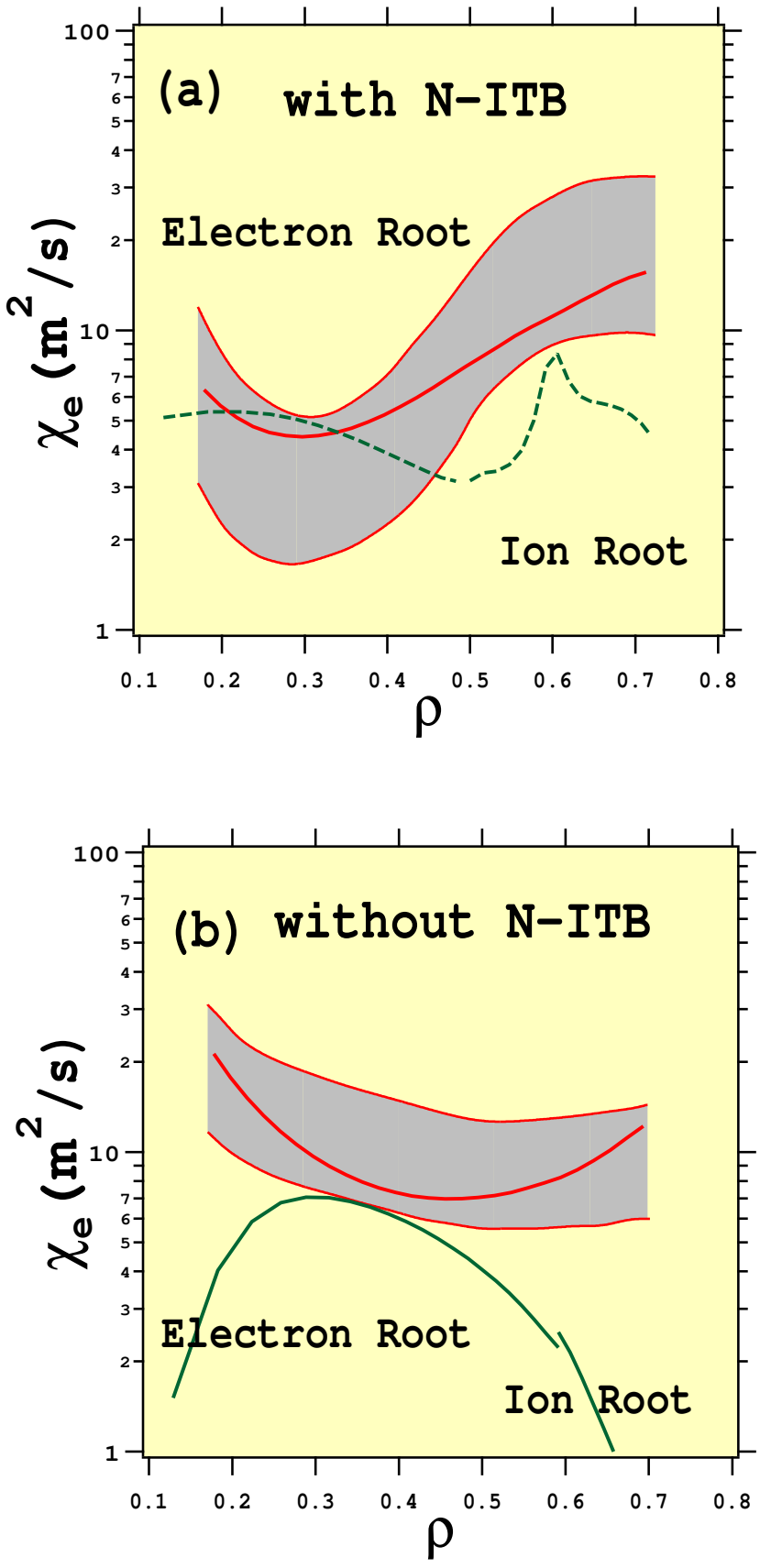

Figure 37: **Comparison of experimental thermal diffusivity and neoclassical calculation:(a) with N-ITB; (b) without N-ITB. The χ_e with N-ITB is lower than that without N-ITB.**

diffusivity is $5m^2/s$ around the barrier point for the plasma with N-ITB. It steeply reduces at location of the large electron temperature gradient.

The error is mainly derived from the uncertainty of the electron temperature gradient. The experimental thermal diffusivity that is shown as the solid line in figure 37 is calculated from the fitting curve to the profile that is shown in figure 9. The plotted error is estimated by the uncertainty of measured data from the fitting curve. Because of the small gradient, the error is larger in plasma center and edge regions.

We compare the electron thermal diffusivity of the ECH plasma with N-ITB ($P_{inj} = 200kW$) with that without N-ITB ($P_{inj} = 150kW$). In spite of the high electron temperature, the electron thermal diffusivity of the plasma with N-ITB is significantly lower than that of the plasma without N-ITB. On the other hand, in the region outside $\rho = 0.5$, there is no difference in the electron thermal diffusivity between the plasmas with N-ITB and without N-ITB.

The experimental electron thermal diffusivity is compared to the neoclassical electron thermal diffusivity including neoclassical ripple transport to investigate the effect of both radial electric field and the radial electric field shear on the electron energy transport. The transition to the N-ITB plasma occurs due to the increase in T_e under the threshold density. The calculated neoclassical thermal diffusivities for electrons are shown by the dotted line in figure37. The neoclassical coefficients are calculated from the neoclassical particle fluxes. At the same time the radial electric field is determined from the ambipolar condition, Eq.35.

The neoclassical electron thermal diffusivity also shows the transition to the electron root inside $\rho = 0.5$ for the ECH plasma with N-ITB. Although the data show that the neoclassical ripple transport is dominant since the plasma is of very low collisionality. This dose not indicates the small anomalous transport. The increase of the neoclassical transport around $\rho = 0.3$ is due to the increase of the electron temperature. The reduction of the experimental electron thermal diffusivity shows the effect of fluctuation suppression at the N-ITB around $\rho = 0.3$.

In the region of the outside of $\rho = 0.5$, the neoclassical flow remains in the ion root. The experimental electron thermal diffusivity is considerably higher than the neoclassical one. Therefore, the anomalous transport is dominant in the edge region.

For the ECH plasma with N-ITB, the experimental electron thermal diffusivity ($2 - 6m^2/s$) is almost equal to the neoclassical electron thermal diffusivity ($5m^2/s$) at $\rho = 0.3$, while for the plasma without N-ITB the experimental electron thermal diffusivity ($7 - 20m^2/s$) is larger than the calculated neoclassical electron thermal diffusivity ($7m^2/s$). These results show the reduction of anomalous transport with N-ITB.

As is shown in figure 37, the experimentally determined location of the transition from the electron root to the ion root is inside $\rho = 0.3$, while the result of the neoclassical calculation shows the transition at $\rho = 0.5$. To obtain more accurate fluxes, it is necessary to take into account the effect of the high energy electrons that are produced by ECH. However, this calculation is very time-consuming, and the further investigation is needed.

Consequently, the electron thermal diffusivity in the plasma with N-ITB is lower than that without N-ITB by the factor of 3. The reduction of the electron thermal diffusivity at the N-ITB is due to both the reduction of the anomalous transport and the improvement of the neoclassical transport.

4.5 Characteristics of Ion Transport for N-ITB of EC heated N-ITB Plasma

In this section, the property of the thermal transport for EC heated NBI plasma with the N-ITB is discussed. The calculation is carried out using the parameters (T_e, n_e, P_{inj}^{ECH}) of above described EC heated NBI palma, as shown in figure 23.

Figure 38 shows electron thermal diffusivity for two plasma discharges with N-ITB and without N-ITB.

First, for the electron thermal diffusivity, the N-ITB plasma gives reduced χ_e at $\rho \sim 0.4$ compared to plasma without N-ITB. It is main reason for the electron temperature increase in

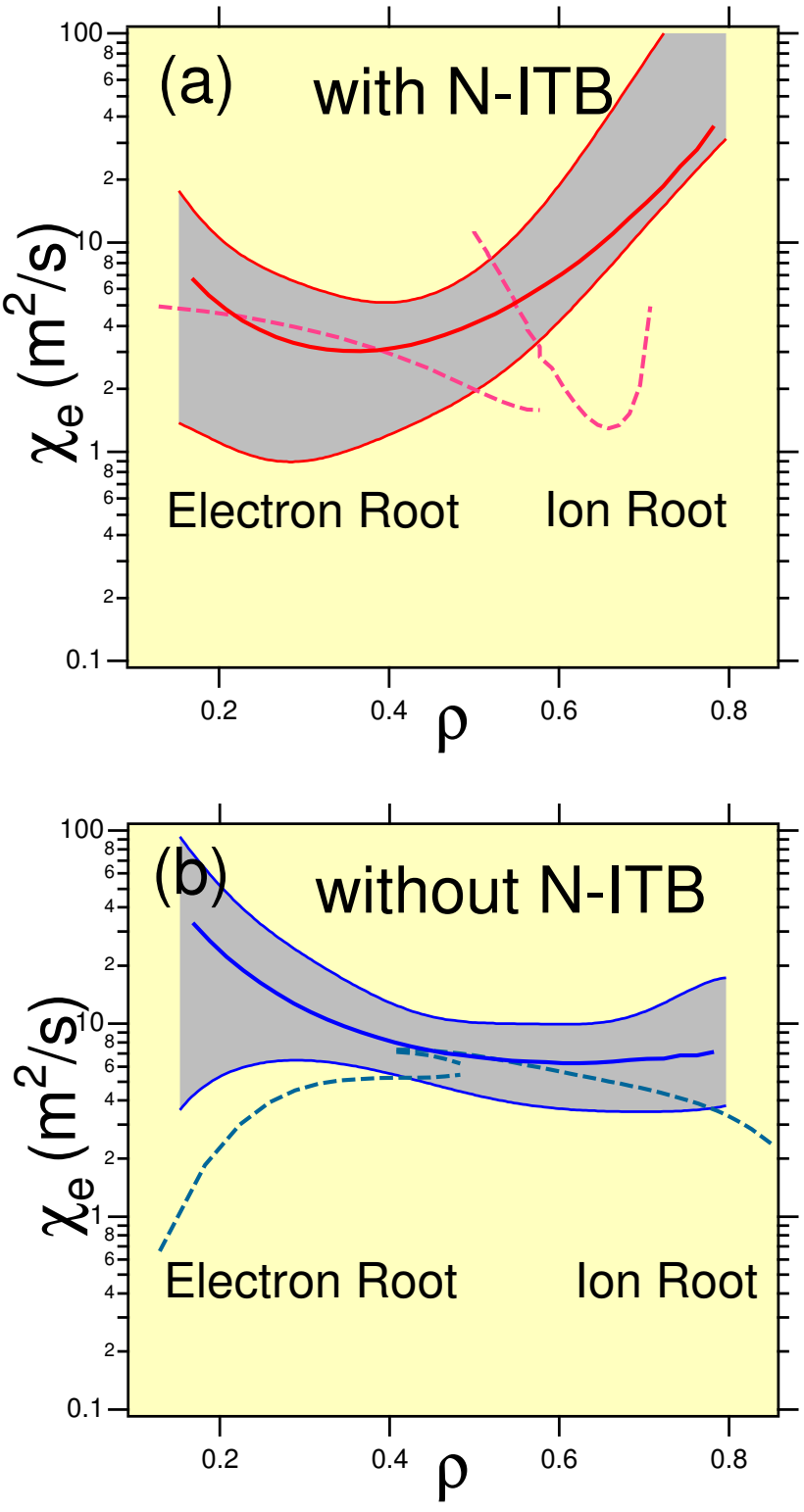

Figure 38: **Comparison between experimental electron thermal diffusivities with N-ITB (a) and without N-ITB (b) for EC heated N-ITB plasma. The dashed lines denote the neoclassical values.**

the core region.

The neoclassical thermal diffusivities are also plotted on the same graph by dotted lines. For the EC heated NBI plasma with N-ITB, the experimental electron thermal diffusivity ($\sim 4m^2/s$) is almost equal to the neoclassical electron thermal diffusivity at $\rho = 0.3 - 0.4$, while for the plasma without N-ITB the experimental electron thermal diffusivity ($7 - 20m^2/s$) is larger than the calculated neoclassical electron thermal diffusivity ($8m^2/s$). The neoclassical electron thermal diffusivity also shows the transition to the electron root inside $\rho = 0.6$ for the EC heated NBI plasma with N-ITB, while in the region outside $\rho = 0.6$, the neoclassical flow remains in the ion root.

These main characteristics of the electron transport in the EC heated NBI plasma are almost same as those in the ECH plasma above described. This is because the difference of the heating power to the electrons between both cases is small: the absorbed ECH power in the ECH plasma is almost same as that in the EC heated NBI plasma , and the deposited NBI power ($P_{abs} \sim 20kW$) to the electrons is considerably smaller than the absorbed ECH power ($P_{abs} \sim 100kW$), then the difference of the the total absorbed power between the two plasmas is slight.

However, the location of the minimum electron thermal diffusivity is different between the ECH plasma and the EC heated NBI plasma: the location of the minimum electron thermal diffusivity of the EC heated NBI plasma is moved to the outer position ($\rho \sim 0.4$) from $\rho \sim 0.2 - 0.3$, so that the improved region by the N-ITB is expanded, which corresponds to the expanded region where the electron temperature increases. In addition, this expansion also corresponds to the expanded region where the large positive radial electric field exists as shown in figure 30.

Figure 39 shows ion thermal diffusivities for two plasma discharges with N-ITB and without N-ITB. Secondly, for ion diffusivity ,the transport analysis shows the sharp reduction of the ion thermal diffusivity ($\chi_i < 1m^2/s$) at $\rho \sim 0.6$ for N-ITB plasma which is the direct

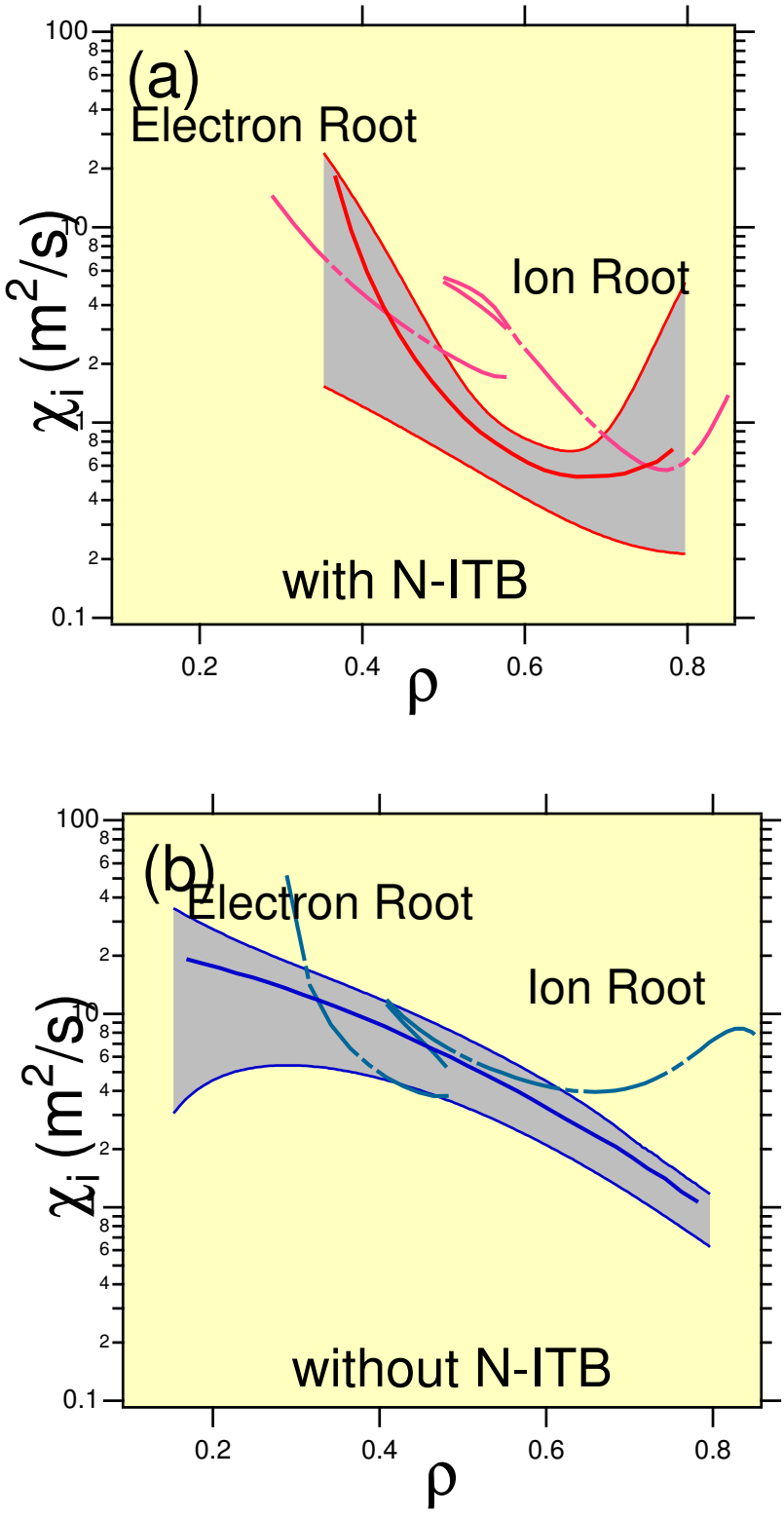

Figure 39: **Comparison between experimental ion thermal diffusivities with N-ITB (a) and without N-ITB (b) for EC heated N-ITB plasma. The dashed lines denote the neoclassical estimate.**

reflection of the steep ion temperature gradient at that position as shown in figure 39. The experimental ion thermal diffusivity for the N-ITB plasma considerably deceases from χ_i of $\sim 2-3m^2/s$ that corresponds to the plasma without N-ITB.

The neoclassical calculation is added on the same graph that is denoted by the dotted lines. The calculation exhibits that the transition from the ion root to the electron root occurs inside *rhosim*0.6 for the N-ITB plasma. For the plasma without the N-ITB, though the transition also occurs in the plasma core, the area of the electron root is narrower than that for the N-ITB plasma and there is no sharp reduction in the ion thermal diffusivity.

The value of the ion thermal diffusivity is less than the neoclassical level at the barrier location, while the diffusivity is larger than the neoclassical calculation for the plasma without the N-ITB, as shown in figure 39(a) (b). Similar results for the ion transport are obtained in the ITB experiments in the reversed shear configuration in the tokamak devices such as TFTR [2, 3, 4], DIIID [5], and JT-60U [6, 7]. In these experiments, the ion transport that is less than the neoclassical prediction is explained by the violation of the assumption for the neoclassical model: the scale length of the ion pressure gradient is comparable to the ion thermal banana width. In N-ITB experiments for helical plasma on CHS, very sharp ion pressure gradient is also observed, and the assumption of the Kovrizhnykh formula may be violated [57].

The another question is the difference in the locations of the minimum diffusivity between the ions and electrons. The minimum diffusivity location for the electrons exists at $\rho \sim 0.3$ which corresponds to the position of the sharp electron temperature gradient existing, while the location for the ions is $\rho \sim 0.6$ which corresponds to the position of the sharp ion temperature gradient existing. In this experiment, the location for the electrons coincides with the point of the maximum radial electric field, while the location for the ions coincides with the point of the maximum $E \times B$. Thus, at the maximum $E \times B$ location, the experimental electron thermal diffusivity is greater than the neoclassical one, while the experimental ion thermal diffusivity is

less than the neoclassical estimation. Accordingly, the suppression of the anomalous transport for ion by $E \times B$ shear is more effective than that for the electrons. However, this conclusion also depends on precise calculation of the neoclassical value. In addition, in other experiments, the plasma with the sharp electron temperature gradient is observed that is created on the outer position than $\rho \sim 0.3$.

Consequently, although further study is necessary to make complete understanding of the transport characteristics of the N-ITB including the modification of the Kovrizhnykh formula that take into account the fine structure of the plasma profile, these results show the simultaneous formation of the ion and electron thermal transport barriers in the new N-ITB plasma.

5. Conclusions

The investigation of the N-ITB plasma on CHS is carried out using the 24 spatial channel multipulse YAG Thomson scattering system. The experimental results and the transport analysis are summarized as follows.

5.1 N-ITB of ECH Plasma

1 The N-ITB is created by the 2nd harmonic EC heating at 53.2GHz for the magnetic field strength of B=0.88T, where P_{inj}^{ECH} is 200 kW. The N-ITB is formed at $\rho = 0.2 - 0.3$ in low density EC heated plasma ($n_e \sim 4\times10^{12} cm^{-3}$). The central electron temperature increases up to $2.2 \pm 0.1 keV$. The steep electron temperature gradient ($dT_e/dr \sim -0.6 keV/m$) is produced at the barrier location, and the shape of the electron temperature is transformed to the ”dome”. The electron temperature increases up to $\sim 4 keV$ by the further reduction of the density to $2 \times 10^{12} cm^{-3}$.

2 There is question whether the high value of the electron temperature ($T_e \sim 2 - 4 keV$) reflects the bulk component or the tail component that is a minority of the electrons. It is confirmed by the six channel measurement of the YAG Thomson scattering that the high value reflects the temperature of the bulk electrons, not the tail electrons.

3 The potential profile of the N-ITB plasma has the prominent dome structure in the core region as well as the electron temperature. The large radial electric field ($E_r \sim 5 kV/m$) is observed inside $\rho = 0.3$ due to the transition to the electron root from the ion root. The radial electric shear grows up at $\rho = 0.3$,of which value is $\sim 300 V/m^2$ at the barrier location.

4 Density fluctuation around N-ITB measured with HIBP shows the clear reduction of the fluctuations at the barrier location by 39%. That means the suppression of the anomalous

transport at the barrier location.

5 The density threshold of the N-ITB formation clearly exists at $4-5\times10^{12}cm^{-3}$ with $P_{inj} \sim 120kW$. These observations show a good agreement with the potential measurement.

6 The N-ITB can be created in the higher density plasma ($\sim 9\times10^{12}cm^{-3}$) at high magnetic field strength $B_T = 1.76T$ by both second harmonic heating (106GHz) and fundamental heating (53GHz). The central electron temperature increases up to 1.8-1.9 keV with the prominent temperature gradient produced at $\rho \sim 0.2 - 0.3$.

7 The $E\times B$ shearing rate is a measure suppression of the anomalous transport. The shearing rate for the EC heated NBI plasma increases up to $\omega_{E\times B} = 4.0 \times 10^5 s^{-1} with dE_r/dr \sim 300kV/m^2$ that is two times as large as that for the ECH plasma ($\omega_{E\times B} = 2.5 \times 10^5 s^{-1}$) . The peak of the shearing rate exists around $\rho \sim 0.5$ that is outer than the peak of the ECH plasma with the N-ITB ($\rho \sim 0.25$). The shearing rate values for the ECH plasma are comparable to that at the internal transport barrier observed in Tokamak experiment.

8 The electron transport analysis for the N-ITB plasma is carried out. In spite of the high electron temperature, the electron thermal diffusivity of the plasma with N-ITB in the core region is significantly lower than that of the plasma without N-ITB. The reduction of the electron thermal diffusivity at the N-ITB is due to both the reduction of the anomalous transport and the improvement of the neoclassical transport. The reduction of the experimental the electron thermal diffusivity in the core region shows the effect of fluctuation suppression at the N-ITB around $\rho = 0.3$.

5.2 N-ITB of EC heated N-ITB Plasma

1 New N-ITB regimes are found with the improved confinement for not only electrons but also ions in EC heated NBI plasmas. The N-ITB is created by the EC heating at 53.2GHz for $B_T of 0.88T$ and P_{inj}^{ECH} of 130-150kW in low density plasma ($n_e \sim 3 - 4 \times$

$10^{12}cm^{-3}$). The electron temperature increases up to $\sim 3keV$ with a sharp temperature gradient ($dT_e/dr \sim 20keV/m$). These characteristics are generally similar to the results of the N-ITB ECH experiment without NBI.

2 The improved confinement region is expanded for electrons from $\rho \sim 0.2 - 0.3$ to $\rho \sim 0.4 - 0.5$ compared to ECH N-ITB experiments.

3 With N-ITB formation, the ion temperature increases ($T_i(0) \sim 400 - 500eV$) by about two to three times,and the sharp ion temperature gradient (8-12 keV/m) is produced at $\rho \sim 0.6$.

4 The decrease of the ion temperature is much slower than that of the electron temperature after the electron transport barrier disappears.

5 The N-ITB is formed when the plasma is heated at the location close to the magnetic axis ($-2cm < R_{resonance} < 2cm$). When the plasma is heated in the outer region, the structure of the N-ITB is not clear, because the electron temperature profile is broad compared to that in the central heating.

6 The N-ITB formation, for not only electrons but also ions, in EC heated N-ITB plasma also strongly depends on the plasma density. When the averaged electron density is below the threshold density ($n_e \sim 4 \times 10^{12}cm^{-3}$), the central electron temperature considerably increases. The threshold density and other characteristics for electrons are very close to the ECH plasma N-ITB experiments. The central ion temperature rapidly increases up to $\sim 500eV$ from $\sim 200eV$ by the application of ECH when the density is lower than $3 - 4 \times 10^{12}cm^{-3}$. The ion temperature gradient at $\rho = 0.6$ increases from 2-3 keV/m up to 8-12 keV/m in the case of N-ITB.

7 The transport barrier is also accompanied with the large positive radial electric field ($E_r \sim$

$15kV/m$), which is larger than that ($E_r \sim 6kV/m$) in ECH plasma. The region of the increased radial electric field is expanded in accordance with the expansion of the region of the increased potential. The neoclassical calculations show good agreement with the measurements. It is clear that the radial electric field of N-ITB is induced by the transition from the ion to the electron root.

8 The dependence of the N-ITB formation on the magnetic axis position is observed. Both the electron and ion temperatures, where the magnetic axis is located at $R_{ax} = 94.9cm$, are higher than those where the magnetic axis is located at the normal position ,$R_{ax} = 92.1cm$ or$R_{ax} = 97.4cm$.

9 The impurity transport is decreased inside the barrier from the measurement using two-dimensional soft x-ray CCD camera. The averaged peak energy of the TiK_α line at $\rho =$ 0.03 (4.72-4.73 keV) is shifted to 4.68-4.69kV . The core diffusion coefficient is reduced to $< 0.02m^2/s$ in the plasma with N-ITB, while it is $0.1 - 0.18m^2/s$ in the plasma without N-ITB.

10 The NBI heating power deposition for the N-ITB plasma is estimated using the Mote Carlo simulation code. Although the fraction of the heating power to ions increases by the electron temperature rise, the large increase of ion temperature (two to three times higher) is not explained by the change of heating power, because of the reduction in the deposited power with the lower density of the N-ITB plasma.

11 The shearing rate for the plasma with N-ITB increases up to $\omega_{E\times B} = 4.0\times10^5 s^{-1} with dE_r/dr \sim 300kV/m^2$ that is approximately two times as large as that for the ECH plasma. The peak of the shearing rate exists around $\rho \sim 0.5$ that is outer than the peak position for the ECH plasma with the N-ITB ($\rho \sim 0.25$). The shearing rate values for the EC heated NBI plasma are comparable to those at the internal transport barrier observed in Tokamak ex-

periment. The local radial electric field is maximum at the plasma center and the barrier location, while the $E \times B$ shearing rate has a single maximum point around the barrier location. Accordingly, the correlation between the N-ITB and the $E \times B$ shearing rate is significant.

12 The transport analysis for the EC heated N-ITB plasma is performed for both electrons and ions. For the electron thermal diffusivity, the N-ITB plasma gives reduced the electron thermal diffusivity at $\rho \sim 0.4$ compared to plasma without N-ITB. For ion diffusivity ,the transport analysis shows the sharp reduction of the ion thermal diffusivity ($\chi_i < 1m^2/s$) at $\rho \sim 0.6$ for N-ITB plasma which is the direct reflection of the steep ion temperature gradient at that position. The value of the ion diffusivity is less than the neoclassical level ($\chi_i^{neoclassical} \sim 2 - 8m^2/s$) at the barrier location. However, further study is necessary to make complete understanding of the neoclassical feature.

6. Acknowledgements

The author would like to appreciate Professors Keisuke Matsuoka and Shoichi Okamura for valuable encouragements, suggestions, a great deal of advice and valuable comments to this work. The author would like to appreciate Professor Kazumichi Narihara for his useful suggestions and support to develop the YAG laser Thomson Scattering System. The author would like to appreciate Professor Akihide Fujisawa and Professor Katsumi Ida for their enlightening discussions, suggestions and a great deal of advice. The author would like to appreciate Professor Shigeru Sudo for continuous encouragements, suggestions, and assistance in preparing this manuscript. The author would like to appreciate Professors Masami Fujiwara and Osamu Motojima for continuous encouragements and support to study this work.

The author also would like to thank to Dr. S.Nishimura for measurement of charge exchange spectroscopy, Dr. Y.Yoshimura for electron cyclotron heating, Prof. S.Murakami for calculation of NBI deposition and Dr. M.Yokoyama for calculation of neoclassical radial electric field and transport, Dr. Y.Liang for x-ray CCD camera measurement, Prof. H.Iguchi for edge density measurement, Prof. K.Toi for magnetic fluctuation measurement. The author would also like to thank Dr. C. Suzuki and Dr. M.Isobe for CHS experiment. The author is much obliged to Mr. C.Takahashi for operation of data acquisition system. Finally, the author thanks to all member of CHS group.

References

[1] U.Stroth et.al Nucl. Fusion 36 (1996) 1063

[2] F.M.Levinton, et.al.,Phys.Rev.Lett. 75 (1995) 4417

[3] R.E.Bell, F.M.Levinton, S.H.Batha, et.al.,Phys.Rev.Lett. 81(7) 1429

[4] R.E.Bell, F.M.Levinton, S.H.Batha, et.al., Plasma Phys. Control. Fusion 40(1998) 609-613

[5] E.J.Strait, et.al., Phys.Rev.Lett 75 (1995) 4421

[6] T.Fujita, et.al., Phys.Rev.Lett 78 (1997) 2377

[7] T.Fujita, et.al., Nuclear Fusion, 38(2) (1998)

[8] T.Fujita, et.al., Proc. 17th Fusion Energy Conference Yokohama, Japan (1998) IAEA-CN-69/EX1/2

[9] K.H.Burrell Phys. Plasmas 4 (5) (1997) 1499

[10] Brakel R et.al., Plasma phys. Control Fusion 39 B273

[11] H.Maasberg, et.al., Physics of Plasmas 7(1) (2000) 295

[12] A.Fujisawa, Plasma phys. Control Fusion 44(2002) A1-A18

[13] O.Motojima et.al., 19 th IAEA Fusion Energy Conference Proceeding.

[14] Liang, Y., et.al., Phys. of Plasmas 9 (10) (2002) 4179

[15] H.Röhr, et.al., Nucl. Fusion 22 (1982) 1099

[16] H.Röhr, et.al., IPP Report IPP III/121 B (1987)

[17] B.Leblanc, R.Bell, D.Dimock, et.al., Rev.Sci.Instrum. 61 (11) (1990) 3566

[18] Reich Watterson, Kuo-in Chen, Rev.Sci.Instrum. 61(10) (1990) 2867

[19] J.A.Casey, R.Watterson, et.al., Rev.Sci.Instrum. 63(10) (1992) 4950

[20] H.Salzmann, J.Bundgaard, A.Gadd, et.al., Rev.Sci.Instrum. 59(8) (1988) 1451

[21] N.Bretz, D.Dimock ,et.al., Applied Optics 17(2) (1978) p.192

[22] D.Johnson, N.Bretz, D.Dimock, et.al., Rev.Sci.Instrum. 57(8) (1986) 1856

[23] R.R.Kindsfather, D.A.Rasmussen, et.al., Rev.Sci.Instrum. 57(8) (1986) 1816

[24] C.J.Barth, M.L.P.Dirkx, et.al., Rev.Sci.Instrum. 63(10) (1992) 4947

[25] C.J.Barth, M.N.A.Beurskens, et.al., ”High Resolution Multiposition Thomson Scattering at RTP” Proceeding of 7th International Symposium on Laser-Aided Plasma Diagnostics (1995)

[26] C.J.Barth, F.J.Pijper, et.al., Rev.Sci.Instrum. 70(1) (1999) 763

[27] T.Hatae, A.Nagashima, et.al., Fusion Engineering and Design 34-35 (1997) 621-624

[28] T.N.Carlstrom et.el. , Rev.Sci.Instrum. 63 (10) (1992) 4901

[29] P.K.Trost et.el. , Rev.Sci.Instrum. 61(10) (1990) 2864

[30] C.M.Greenfield, et.el. , Rev.Sci.Instrum. 61(10) (1990) 3286

[31] E.Agostini, et.al., ”The Thomson scattering System of Tore Supra. First Results” Inner report in Tore Supra Experimental Group, not published.

[32] G.Kuhner, H.Ringler ”Thomson Scattring on WVII-AS” Inner report in WVII-AS Experimental Group, not published. (1987)

[33] K.Narihara, et.al., Rev.Sci.Instrum. 66 (9) (1995)

[34] T.Minami, et.al., Reports on Topics Meeting of the Laser Society of Japan no.RTM-96-3 (1996) 13-18

[35] I.H.Hutchinson ”Principles of Plasma Diagnostic” Cambridge University Press

[36] V.A.Zhuravlev and G.D.Petrov Aov J.Plasma.Phys. 5(1) (1979)

[37] W.Stephen ”Mathematica” Second Edition ADDISON WESLEY 51502

[38] J.Howard et.al., J.Phys. D:appl. Phys., Vol.12 (1979) 1435

[39] H.Röhr, Physics Letters 81A(8) (1981) 451-453

[40] C.M.Penney, R.L.St. Peters, and M.Lapp J. Optical Sciety of America 64(5) (1974) 712-716

[41] K.Matsuoka et.al., Plasma Physics and Controlled Nuclear Fusion Research 1988 (Proc. 12th Int. Conf. Nice,1988) Vol.2,IAEA, Vienna (1989)

[42] A.Fujisawa, T.Minami,et.al., Phys.Rev.Lett. 82 (1999) 2669

[43] T.Minami, A,Fujisawa, et.al., J.Plasma Fusion Res. SERIES, Vol.4 (2001) 451-456

[44] T.Minami, A.Fujisawa, et.al., 26th EPS conference proceeding (1999)

[45] A.Fujisawa, H.Iguchi, T.Minami,et.al., Nuclear Fusion 41(5) (2001)

[46] A.Fujisawa, H.Iguchi, T.Minami, et.al., Plasma Phys. and Control. Fusion 41 A561-A568 (1999)

[47] A.Fujisawa, H.Iguchi, T.Minami, et.al., J.Plasma Fusion Res. SERIES, Vol.4 (2001) 454-460

[48] T.Minami, A.Fujisawa, et.al., Plasma Phys. Control. Fusion 44 (2002) A197-A201

[49] A.Fujisawa, H.Iguchi, T.Minami, et.al., Plasma Phys. and Control. Fusion 42 A103-A108 (2000)

[50] T.Minami, et.al., Nuclear Fusion submitted.

[51] K.Ida, et.al., Rev. Sci. Instrum. 60 (1989) 867

[52] K.Ida, et.al., Nucl. Fusion 39 (1999) 1649

[53] T.Minami, K.Ida, et.al., J.Plasma Fusion Res. vol.1 (1998)

[54] E.J.Synakowski, Plasma phys. Control. Fusion 40(1998) 581-596

[55] T.S.Hahm Phys. Plasmas 4(11) (1997) 4074

[56] M.Yokoyama, et.al.,, Nucl. Fusion 42 (2002) 133

[57] L.M.Kovrizhnykh, Nucl. Fusion 24 (1984) 435

[58] S.P.Hirshman, J.C.Whitson, Phys. Fluids 26(12) (1983) 3553-p3568

[59] S.Murakami et.al., Nucl. Fusion 40(2000) 693.

[60] S. Okamura, et.al. , Nucl. Fusion **39** (1999), p1337

[61] M.Yokoyama, et.al. J.Plasma Fusion Res. **79** (2003) p816

[62] S.Murakami, et.al.,J. Plasma Fusion Res. SERIES, 2 (1999) 255.

[63] H. C. Howe, Rep. ORNL/TM-11521, TN(1990)

[64] I. Fidone and G. Granata, Nucl. Fusion 11 (1971) 133